Cobalt, Chromium Implant Wear:

Investigating interactions between products and the local environment

and

Presenting an approach for mapping tissues

by

HAYLEY FLOYD

A thesis submitted to The University of Birmingham
for the degree of DOCTOR OF PHILOSOPHY

PSIBS Doctoral Training Centre
College of Engineering and Physical Sciences
The University of Birmingham
August 2017

Abstract

Modern cobalt-chromium (CoCr) alloy compositions, for hip implants, were developed to resist the issues of wear and corrosion; however they still succumb to degradation. While the literature is vast, there is still a lack of understanding of the variability in implant-metal derivatives generated, and the effect such products can have on biological components other than just cells.

In this thesis the effect of Co ions on type I collagen (main component of the extracellular matrix) was investigated. The conformation of the triple-helix was maintained, however the time taken for fibril formation to complete increased with Co concentration. In addition, with increasing Co, the collagen matrix became more heterogeneous and cellular attachment and proliferation was reduced. It is likely that Co ions are interacting with a C-O (hydroxyl) group.

An overlooked population of degradation products was also investigated. They were found to be highly dependent upon the local environment. Media composition resulted in changes to the morphology, while pH directed the initiation of precipitation. A pH <5 resulted in no observed pellet. In addition, the presence of Co ions in the media resulted in a change of Cr speciation.

Finally, an approach is presented for sub-micron (600nm) x-ray absorption near edge spectroscopy (XANES) mapping of *ex vivo* tissue. Sub-micron XANES maps contained at least 4 spectra, determined through principal component analysis and clustering. A 5x5 pixel region was averaged for comparison to the 3μm beam approach. Both spectra contained similar features representative of chromium phosphate suggesting that XANES with a micron-sized beam (standard approach) cannot represent the full chemical variability present within the tissue.

Author Declaration

All the work submitted in this thesis for assessment is solely my (H.F.) work. For chapter 4, experimental research was performed solely by H.F. for all parts except the AlamarBlue assay, raman spectroscopy and differential scanning calorimetry performed by Emma McCarthy (Grover group, Physical Sciences for Health, University of Birmingham). The collection of Diamond and Swiss Light Source beamline data (chapter 6) was performed jointly by the H.F. with fellow PhD student Alex Morrell (A.M.) from Aston University. Collection of ESF beamline data by H.F. solely of raw beamline data on MANTiS (PCA and clusteanalysis) was performed jointly by H.F. and A.M. All other analysis was performed by H.F. solely.

Hayley Floyd

Acknowledgements

I would like to thank the PSIBS doctoral centre and all my supervisors Professor Liam Grover, Professor Owen Addison, Mr Edward Davis, Professor Janet Lord, and Dr Hamid Dehghani for giving me the opportunity to carry out this work. In particular I would like to also express my deepest appreciation to Liam and Owen for their on-going guidance, support and inspiration throughout my PhD.

I would also like to thank all the fellow PhD's, post-docs, fellows, and lab staff that aided in training during my experiments, particularly Dr Richard Williams and Dr Gurpreet Chouhan for their guidance in cell culture and collagen preparation and the other members of the Grover group for all their help during the years. I would also like to extend my appreciation to Alex Morrell from Aston University who was a collaborator on acquiring data and analysis for chapter 6, thanks for the late night beam-time company.

I would also like to thank my family for their on-going encouragement not only through this PhD but throughout everything I have chosen to do, and to all my friends, who have listened and motivated me many times over the years.

Finally, to my Wife Sarah, who has experienced all of this PhD with me from helping me practise talks, to keeping me company during late-night experiments, to proof reading my thesis and keeping me sane. Thank you.

Table of Contents

Chapter 1: Introduction 1

Chapter 2: Literature Review Part 1 4

2.1. Cobalt-Chome Alloys 4
2.2. Hip Arthroplasty 4
2.2.1. Metal-on-Metal Implants 7
2.3. Modern Cobalt-Chrome Alloy composition 9
2.4. Tribocorrosion Mechanisms 10
2.5. Characteristics of Wear Debris 16
2.5.1. Wear Particles 17
2.5.2. Co and Cr Ions 22
2.5.3. Other Metal Species 27
2.6. Co and Cr in the Body 30
2.6.1. Cobalt 30
2.6.2. Chromium 30
2.7. Biological Response to CoCr Wear Products 31

Chapter 3: Literature Review Part 2 36

3.1. Collagen Structure 36
3.1.1. Effect of Co and Cr on Collagen 38
3.2. Analysis techniques for collagen 40
3.2.1. Circular Dichroism 40
3.2.2. Turbidity Curves 42
3.2.3. Small Deformation Oscillatory Rheology 43
3.3. Imaging of CoCr in *ex vivo* tissue 44
3.3.1. Synchrotron X-ray Spectroscopy 45
3.3.1.1. X-ray Fluorescence Phenomenon 47
3.3.1.2. X-ray Fluorescence Mapping 48
3.3.1.3. X-ray Absorption Near-Edge Spectroscopy 48

3.3.2. Studies of CoCr in Tissue 50

Chapter 4: How Do Cobalt Ions Affect Collagen Formation? 53

4.1. Introduction 53
4.2. Methodology 57
4.2.1. Collagen Preparation 57
4.2.2. Circular Dichroism 57
4.2.3. Reflection Confocal Microscopy 58
4.2.4. Atomic Force Microscopy 59
4.2.5. Turbidity Curves 60
4.2.6. Rheometry 60
4.2.7. Cell Culture 60
4.2.8. Cell Splitting & Counting 61
4.2.9. Incubation of Cells and Collagen 62
4.2.10. ICP-OES 63
4.2.11. MTT Assay 64
4.2.12. Collagen Gel Contraction Assay 65
4.2.13. X-ray Fluorescence 66
4.2.14. Cell Staining 67
4.2.14.1. Live-Dead Staining 67
4.2.14.2. Actin and DAPI Staining 68
4.2.15. AlamarBlue Assay 69
4.2.16. Raman Spectroscopy 70
4.2.17. Differential Scanning Calorimetry 70
4.3. Results 72
4.3.1. Determining the Effect of Co(II) on Collagen Triple Helix. 72
4.3.2. Determining the Effect of Co(II) on the Formation of Collagen Fibrils 73
4.3.3. Determining the Dispersion of Cobalt Throughout the Bulk Matrix 76
4.3.4. Determining the Effect of Co(II) Ions on the Collagen Matrix. 77
4.3.5. Determining the cellular response to Co-collagen gels 81
4.3.6. Determining potential binding sites between cobalt ions and collagen. 85
4.4. Discssion 87

4.5. Conclusion 92

Chapter 5: Precipitation of Metal Ions in Media 94

5.1. Introduction 94
5.2. Methodology 97
  5.2.1. Precipitation of Cr(III) in Various Media 97
  5.2.2. Preparation of Biological Media 97
  5.2.3. Monitoring pH After Addition of Cr(III) 98
  5.2.4. Flame Absorption Atomic Spectroscopy of Cr(III) in Supernatant 99
  5.2.5. Scanning Electron Microscopy 100
  5.2.6. European Synchrotron Radiation Facility 101
  5.2.7. Synchroton-XRF & Synchroton-Xanes 101
5.3. Results 104
  5.3.1. Determining the Effect of pH on the Initiation of Cr(III) Precipitation 104
  5.3.2. Observing the effect of media composition on Cr(III) precipitation 106
5.4. Discussion 113
5.5. Conclusion 116

Chapter 6: Multiscale Mapping of Metal Particles in Tissue - Presenting an Approach 119

6.1. Introduction 119
6.2. Methodology 123
  6.2.1. Preparation of Tissue 123
  6.2.2. Diamond Light Source 124
  6.2.3. Swiss Light Source 125
  6.2.4. European Synchrotron Radiation Facility 126
  6.2.5. Histological Staining 127
  6.2.6. XRF Analysis 128
    6.2.6.1. Producing XRF Maps 128
    6.2.6.2. Correlation of Co and Cr with Mo 128
  6.2.7. XANES Analysis 129
    6.2.7.1. Metallic Contribution 129
    6.2.7.2. Principal Component Analysis and Clustering 129

6.2.7.3. Linear Combination Fitting 130
6.2.7.4. ESRF Data Binning 131
6.3. Results & Discussion 132
6.3.1. Histological Staining 132
6.3.2. Spectroscopic Mapping Approach 134
6.3.2.1. Micron-scale Mapping 134
6.3.2.2. Sub-micron Mapping 138
6.3.2.3. Validation of Sub-Micron Mapping Approach 144
6.3.3. Analysis Methods for Mapping Approach 146
6.3.3.1. Conformation of Metal Particle 146
6.3.3.2. Principal Component Analysis & Clustering 148
6.4. Conclusions 150

Chapter 7: Discussion 153

7.1. Overall Discussion 153
7.2. Future Works 161
References 164

List of Figures

Figure 2.1: Diagram representing the two types of hip replacement performed; (a) the total hip replacement (THR), and (b) hip resurfacing **6**

Figure 2.2: Schematic of corrosion mechanisms **12**

Figure 2.3: Relations between the main characteristics of wear particles and the information regarding the wear mechanisms and biological activity that can be typically obtained **21**

Figure 2.4: A summary of case studies and review regarding poorly functioning hip implants and the levels of cobalt and chromium ions measured in surrounding tissues and fluids. **23**

Figure 2.5: Abnormal fluid and metal staining of the tissues surrounding the implant. In addition the patient was found to have extensive osteolysis in the acetabular and femoral regions **24**

Figure 2.6: Schematic showing the complex nature of the signalling pathways induced by CoCr implant debris resulting in inflammation and contributing to osteolysis **32**

Figure 3.1: Figure 3.1: The formation process of collagen fibres begins inside cells where the triple helix is formed prior to secretion into the extracellular environment where they self-assemble and cross link to form fibres **37**

Figure 3.2: Figure 3.2: Characteristic circular dichroism profile of fully formed collagen. The positive and negative peaks are located around 220 and 200nm respectfully **41**

Figure 3.3: Characteristic profile for collagen fibrillogenesis showing the 3 phases: Initial lag followed by the steep growth phase, where collagen self-assembles to form fibres, and finally the lateral plateau phase **42**

Figure 3.4: Experimental schematic for small deformation oscillatory rheology. The cone-shaped plate is brought into contact with the surface of the sample and small amplitude oscillations are applied **44**

Figure 3.5: Schematic of a standard synchrotron set-up **46**

Figure 3.6: Fundamental process behind XRF and XANES spectroscopy........................**47**

Figure 3.7: Typical x-ray absorption spectra depicting the x-ray absorption near edge spectroscopy (XANES) region and the extended x-ray absorption fine structure (EXAFS) regions of the spectrum. A detailed view of the XANES region highlights the pre-peak, K-edge/peak and the post-peak regions.....**49**

Figure 4.1: Calibration curve for inductively coupled plasma optical emission spectrometry (ICP-OES) between the relative intensity of counts at 228.616nm (characteristic peak of Co) and Co concentration......................**64**

Figure 4.2: Circular dichroism of CoCol gels with a control of collagen only. Changes in the intensities of the positive and negative peaks potentially indicate the interference of Co(II) with the collagen triple-helix formation. Table insert shows the positive peak ellipticity for the CoCol gels................................**72**

Figure 4.3: Mean turbidity profiles for Co dosed collagen at concentrations of 0, 65, 135 & 200 ppm. [a] Early turbidity profile to show growth phase with [b] complete profile. Error bars show the standard deviation for the repeats within each concentration, n=3...**74**

Figure 4.4: [a] Ratio of the growth phase at each Co concentration with respect to the control (0ppm) shows Co increases the time for collagen fibrillogenesis to complete, n=3. [b] Release of Co ions from the collagen matrix after 1 and 6 days for initial concentrations of 0, 65, 135 & 200ppm, n=9. No significanct difference was found between the Co released at day 1 vs. day 6 (p>0.05)..**75**

Figure 4.5: Benchtop X-ray fluorescent (XRF) measurements of Co distribution within a CoCol gel containing 200ppm Co(II). [a] Bright field image of CoCol gel. [b] Relative Co intensity map throughout CoCol gel. [c] Zoomed view of Co map showing positions of region 1 & 2 which represent high and low intensities of Co respectively. [d] Averaged spectra of overall gel, Co region highlighted. [e] Spectra of region 1 & 2 used to show an average 3-fold difference in Co fluorescence...**76**

Figure 4.6: AFM images of collagen with [a-b] 0ppm Co(II), [c-d] 135ppm Co(II), [e-f] 200ppm Co(II). Scale bar is 1μm. [g] Table showing the mean D-banding width calculated from the AFM images, error is calculated as the standard deviation with n=68, using multiple fibril across 3 regions of the sample. [h] A box-whisker plot showing the range of D-bandings measured across the CoCol gel samples. 135 & 200ppm were found to be significantly different to the control (p<0.001)..**78**

Figure 4.7: Reflection confocal microscopy images of the macro-scale network of collagen. A z-stack has been projected onto 2D for visualisation. [a] 0ppm and [b] 200ppm Co. The presence of Co results in heterogeneity in the collagen matrix. **79**

Figure 4.8: [a-e] Images of CoCol gels being lifted from dishes with increasing concentrations of Co(II). [f] Storage modulus, G' and [g] loss modulus, G" from a frequency sweep with a fixed strain. A decrease in the storage modulus of the gel indicates a reduction in stiffness.. .... **80**

Figure 4.9: MC3T3 cells seeded [a] on top of CoCol gels and [b] within Co-doped media, after staining with calcein AM (green) and propidium iodide (red) for live/dead contrast. All images were acquired using a confocal microscope and imaged at day 2, scale bar = 200μm. [d] AlamarBlue assay performed on cells on CoCol gels and within Co-doped media. [e] MTT assay performed on cells within Co-doped media only to assess proliferation. All data suggests a decrease in cell viability and proliferation **82**

Figure 4.10: HDFs seeded [a] on the surface of CoCol gels, scale bar = 100μm and[b] within CoCol gels, scale bar = 200μm. Lower seeding densities for within CoCol gels meant a lower magnification was required to observe a larger field of view. All images show staining with ActinRed 555 (red) and DAPI (blue) for cytoskeleton/nucleus contrast and were acquired at day 3. [c] Shows the collagen gel contraction assay for HDFs within collagen after 3 days, n=3. No contraction was observed with the presence of Co(II).... .... **84**

Figure 4.11: [a] Raman spectra of both 0ppm and 200ppm collagen gels, [b] a scores plot of the first two principal components shows the clusters corresponding to 0 and 200ppm, [c] A loadings plot of the first principal component indicating changes at 1000 cm-1 and 869 cm-1, see the arrows. [d] Differential scanning calorimetry measurements indicating a reduction in energy required to remove bulk water between 0ppm and 200ppm CoCol gels.. .... **86**

Figure 5.1: Calibration curve for flame atomic absorption spectroscopy (FAAS), produced using standards of known Cr(III) solutions. Measurements were performed in triplicate and the mean acquired, with error bars depicting the standard deviation. The linear line of best fit was produced by fixing the intercept at zero and using weighted linear regression.. .... **100**

Figure 5.2: [a] FAAS results showing the concentration of Cr in the supernatant of DMEM incubated with 50ppm Cr(III) for 1 hour at various initial pH conditions. [b] The table shows the pH measured immediately before and after adding Cr(III), a decrease in pH is noted. For reference the initial pH condition is rounded. pH was measured over time for RPMI-1640 adjusted to starting conditions of [c] pH 4 and [d] pH 7.5. After addition of 50ppm Cr(III) pH decreased, before increasing for a starting condition of pH 7.5. Starting condition of pH 4 showed no increase in pH over time **105**

Figure 5.3: Size analysis performed on Fiji (based on ImageJ) to determine particle diameters observed in SEM images. For each sample, precipitation was formed in various environments: cell culture media (RPMI-1640 or DMEM) with or without human serum (HS), phosphate buffered saline (PBS) or simulated body fluid (SBF). The mean diameter and standard deviation from the mean are reported, n=100.. .... **106**

Figure 5.4: SEM images showing the Cr (III) complexes formed in different media (maintained at pH 7 for consistency) after 1hr. Media used were cell culture media (RPMI-1640 or DMEM) with or without human serum (HS), phosphate buffered saline (PBS) or simulated body fluid (SBF). Scale bar is 500nm for all images **107**

Figure 5.5: [a] XRF elemental map imaged at the Cr edge, 5.99keV of the control sample (human synovial fluid (HSF) with no Cr(III) doping). The arrow indicates the location of the single point Cr-XANES measurement shown in [b]. This Cr-XANES spectrum has a low signal-to-noise. **109**

Figure 5.6: Elemental Cr-XRF maps at 5.99keV (Cr-edge) of precipitate formed in human synovial fluid doped with [a] 100ppm Cr(III) only and [b] 38ppmCo(II):100ppmCr(III). Below the XRF maps, the point XANES spectra are shown. Spectra correspond to the points in the XRF images indicated by the labelled arrows. The black arrows on the XANES spectra highlight the post-edge region, where the Cr-edge and first interference peak in [b] is more resolved. **110**

Figure 5.7: Cr(III) XANES references for [a] CrPO4 standard obtained at Diamond Light Source and [b] reference spectra for inorganic and organic Cr(III) **111**

Figure 5.8: Elemental Cr-XRF maps of precipitate formed in human synovial fluid doped with 300ppmCo(II):118ppmCr(III). XRF maps acquired at [a] the Cr-edge, 5.99keV and [b] Co edge, 7.5keV. [c] Cr-XANES measurements are obtained from regions indicated by white arrows in the XRF maps. The black arrow indicates the post-edge region which becomes more resolved with increasing Co presence (from the Co-XRF) **112**

Figure 6.1: Main tissue block - primary source for tissue slices for beamline interrogation. Sample originated close to the acetabular cup, arrows indicate the edge closest to the implant. Due to sample storage the tissue folded back on itself **132**

Figure 6.2: [a] Brightfield image of H&E stained tissue slices adjacent to beamline interrogated samples. Arrows indicate metal particles aggregating along tissue boundaries. [b] Reflection mode image highlights the metal debris within the tissue. [c] Overlay of reflection (blue) and brightfield modes. Scale bar = 100μm **133**

Figure 6.3: XRF image of ex vivo synovial sheath using a 3μm beam at Diamond Light Source. Cobalt, chromium and chlorine (used as a tissue marker to observe geometry) are represented by the red, blue and green channels respectively **134**

Figure 6.4: [a] Static single point XANES measurement, using a 3μm beam on a region with high Cr signal. [b]CrPO4 and CoCr standards on same beam set-up **135**

Figure 6.5: [a] XANES map (~300x45μm in size with a 3μm beam) showing the clusters generated through PCA analysis using software package MANTiS , the spectra in these clusters were summed to produce the spectra in [b]. The arrow shows the location of the pre-peak for Cr(III) species which can give an indication of metallic Cr content **137**

Figure 6.6: XRF images, performed at ESRF, using [a] 4μm beam followed by [b] 600nm beam on smaller ROI's. Co, Cr and Cl are represented by red, blue and green respectively, the latter acquired at a lower energy in [b] to improve signal-to-noise **139**

Figure 6.7: [a] XRF map used to select ROI for XANES mapping (both 600nm). [b] A XANES intensity map - each pixel is a Cr XANES spectrum. [c] Four averaged radial selections (see arrow) of the XANES spectra across the 'particle' - pre-edge range is magnified in in the inset. [d] Graph representing the contribution of Cr metallic fraction vs. other Cr species as determined by linear combination fitting using ATHENA. Metallic Cr contribution is seen to decrease moving radially outwards from the centre of a high intensity region of CoCr **140**

Figure 6.8: Cr-XANES intensity map with XANES spectra at each pixel overlaid. This illustrates the dissimilarity of the spectra moving radially outwards from the high intensity (red) centre. This suggests chemical variability on a submicron scale **141**

Figure 6.9: Clusters were produced of the XANES map in figure 6.8 using k-means clustering, after principle component analysis determined 4 components were sufficient to represent the majority of the data. Cluster 1 could be represented via linear combination fitting of the 3 standards in red, while clusters 3 and 4 have similar spectral features to Cr malate and acetate hydroxide. [right] Cr standards, acquired using similar beam set-ups are shown. **143**

Figure 6.10: A 5x5pixel region, centred on the high Cr intensity point selected for spectral binning to mimic a 3μm beam. The spectra presented are [b] single point spectrum from Diamond, [c] reference spectra, and [d] averaged spectrum from 5x5 region... .... **144**

Figure 6.11: [Top] Two XRF intensity maps centred on a region of high Co. For each regions maps of Mo, Co and Cr were taken at the Swiss Light Source using a 20.02keV beam (Mo) and a 8.5keV beam (Co and Cr). [Bottom] Scatter plots showing the correlation between Mo & Co and Mo & Cr **147**

Figure 6.12: [a] Spectra from principal component and cluster analysis from figure 6.9 and [b] selected spectra from the inset Cr-XANES map from figure 6.8. These spectra originated from data acquired with the 600nm beam at ESRF. [c] Standards with similar spectral features to the corresponding spectrum acquired using a similar experimental set-up **149**

List of Abbreviations

AFM	Atomic Force Microscopy
ASTM	American Society for Testing and Materials
ATSDR	The Agency for Toxic Substances & Disease Registry
BHR	Birmingham Hip Resurfacing
Calcein-AM	Calcein Acetoxymethyleste
CD	Circular Dichroism
CGC assay	Collagen Gel Contraction assay
Co	Cobalt
CoCol	Co-dosed Collagen
CoCr	Cobalt-Chrome
CoCrMo	Cobalt-Chromium-Molybdenum
Cr	Chromium
CrPO	Chromium Phosphaste
DAPI	4',6-diamidino-2-phenylindole
dH20	Deionised Water
DLS	Dynamic Light Scattering
DLS	Diamond Light Source
DMEM	Dulbecco’s Modified Eagle Medium
DMSO	Dimethyl Sulfoxide
DSC	Differential Scanning Calorimetry
ECM	Extracellular Matrix
EDX	Energy-Dispersive X-ray Spectroscopy

EOI	Element of Interest
ESRF	European Synchrotron Radiation Facility
EXAFS	Extended X-ray Absorption Fine Structure
FAAS	Flame Absorption Atomic Spectroscopy
FBS	Foetal Bovine Serum
FDA	(US) Food and Drug Administration
FEG-SEM	Field Emission Gun-Scanning Electron Microscope
FTIR	Fourier Transform Infra-Red
H&E	Heamatoxylin and eosin
HA	Hip Arthroplasty
HBRC	Human Biomaterials Resource Centre
HDF	Human Dermal Fibroblast
HS	Human Serum
HSF	Human Synovial Fluid
IARC	International Agency for Research on Cancer
ICP-OES	Inductively Coupled Plasma Optical Emission Spectrometry
LCF	Linear Combination Fitting
L-Glut	L-glutamine
LM	Light Microscopy
MANTiS	Multivariate Analysis Tool for Spectromicroscopy
MC3T3	Pre-osteoblast MC3T3-E1 subclone 4
MCP-1	Monocyte Chemotactic Protein-1
Mo	Molybdenum
MoM	Metal-on-Metal

MoP	Metal-on-Polyethylene
MTT	3-(4,5-Dimethylthiazol-2-yl)-2,5-diphenyltetrazolium bromide
NaOH	Sodium Hydroxide
NJR	(UK) National Joint Registry
OCT	Optimum Temperature Cutting
PBS	Phosphate-Buffered Saline
PC	Principal Components
PCA	Principal Component Analysis
Pen/Strep	Penicillin-Streptomycin
PFA	Paraformaldehyde
PI	Propidium Iodide
RCM	Reflection Confocal Microscopy
ROH	Royal Orthopaedic Hospital
ROI	Region of Interest
RPMI-1640	Roswell Park Memorial Institute 1640
SBF	Simulated Body Fluid
SCENIHR	Scientific Committee on Emerging and Newly Identified Health Risks
SEM	Scanning Electron Microscopy
SLS	Swiss Light Source
STXM	Scanning Transmission X-ray Microscope
TEM	Transmission Electron Microscopy
THA	Total Hip Arthroplasty
THR	Total Hip Replacement
Ti	Titanium

TNF-α	Tumour Necrosis Factor alpha
UHMWPE	Ultra-High-Molecular-Weight Polyethylene
UV-Vis	Ultraviolet-Visible
W	Tungsten
X05LA	MicroXAS Beamline
XANES	X-ray Absorption Near Edge Spectroscopy
XAS	X-ray Absorption Spectroscopy
XPS	X-ray Spectroscopy
XRF	X-ray Fluorescence
αMEM	Minimum Essential Medium Eagle Alpha Modified

Sarah
Thank you...

Chapter 1

Introduction

In the last century, the increase in life expectancy has resulted in a growing elderly population, increasing the prevalence of musculoskeletal conditions such as osteoarthritis. In addition, as healthcare has improved, there has been an increase in expectation for a good quality of life. As such, patients who present with pain, either from injury or disease, expect strategies of treatment to be able to safely and effectively restore full function. The most revolutionary development, within the last century, for the management of degenerative musculoskeletal conditions is the hip arthroplasty (1). Prostheses are the most effective method of restoring function and treating both pain and disability, and it has revolutionised the way in which osteoarthritis is treated.

However, while heralded as a success, hip implants are prone to degradation products such as ions and wear producing particulate debris, which is released into the surrounding biological environment (2-6). Early low-friction concepts, using ultra-high molecular weight polyethylene, were found to produce large volumes of wear particles which correlated with high revision rates (7, 8); typically caused due to osteolysis and aseptic loosening of the implant (9, 10). Following this, improved manufacturing and implant design resulted in the production of metal cobalt-chrome alloy prosthesis which boasted a higher resistance to wear and corrosion. However, it was later found that the 'metal-on-metal' designs suffered from large numbers of small nano-sized particle debris and the release of metal ions.

The literature investigating the effect of released cobalt and chromium on cellular behaviour in the body is vast (11-18); and describes increases in the local and systemic levels of wear debris, the development of metallosis and adverse tissue reactions, and the rates of implant revision. However, there is still a lack of understanding of both the variability in implant-metal derivatives generated and the host response to such products. It was this that initially motivated this thesis which has since developed into three research questions:

1. **How do cobalt ions affect collagen assembly?** – Typically studies focus on the effects of metal debris on 2D cell cultures and show little consideration for the extracellular matrix; which plays a crucial role in directing cell function and provides the scaffold for hard tissues such as bone. This thesis focuses on the effects of cobalt, which typically remains in solution after corrosion processes.
2. **Investigating precipitation of chromium ions** – Biological consequences of cobalt and chromium will be dependent on how they are presented - either in metallic form, ionic form or precipitated. Only one study has previously investigated the concept of precipitation; other studies only consider free ions. Consequently, what does this mean for the understanding of available implant degradation products? This investigation aimed to be a proof of concept, that environment can impact the speciation of precipitated

degradation products, which became a further motivator for the application of speciation mapping at international beamlines on ex vivo tissues.

3. **Multiscale mapping of metals in tissues** – Investigations into the distribution of cobalt and chromium speciation within tissues predominantly use single point observations, which average over several microns. Given the observation of nano-scale chromium precipitation, it was hypothesised that this method may omit potential small scale changes in speciation.

Given the distinct nature of the aforementioned research questions, each question is addressed within its own self-contained chapter. The literature review for this thesis is presented in two parts, the former will explore the topic of hip arthroplasty that formed the motivation behind this research, and the latter will focus on additional literature related to the research performed. The final chapters provide an overall discussion addressing the impact of this thesis and the future work that may follow.

Chapter 2

Literature Review Part 1
The Issue of Hip Implants

2.1. Cobalt-Chrome Alloys

The first cobalt-chrome (CoCr) alloy was discovered in the early 20th century by Elwood Haynes during his search for corrosion resistant metals and patented under the name Stellite™ (19). Further development to increase strength properties resulted in the addition of other transition metals (20) (such as molybdenum (Mo) and tungsten (W)) to produce the first Co-based super-alloys (21) for which all subsequent CoCr alloys are now derived. Initially used for a broad range of applications, the harder composition alloys soon found their use in the medical industry. They were used for tools (22), dental prosthetics (23), and heart valves (24), though they are more commonly recognised for their use in orthopaedic implants (25, 26). The focus of this thesis will be on the orthopaedic applications of CoCr alloys, specifically hip implants.

2.2. Hip Arthroplasty

Joint arthroplasty is a surgical procedure whereby the articulating surface of a musculoskeletal joint is either resurfaced or replaced. The degeneration of a patient's femoral head, due to either excess wear or disease, can lead to progressive loss of mobility and significant pain. Typically, to relieve pain and restore function, the only viable treatment strategy is to replace the joint. This method has revolutionised the treatment of patients with osteoarthritis or joint trauma (1). Hip arthroplasty (HA) is therefore often heralded as the most important surgical development within the last century (27). While there are many limitations and adverse biological implications that correspond with hip implants, without them many more patients would have been unable to regain function and mobility.

Since the late 19th century there have been many advances in the materials and surgical techniques used in total hip arthroplasty (THA), and the literature reviewing the history of this development is vast (27-30). Early techniques consisted of placing organic tissue between the articulating surfaces (1); however, development favoured the use of non-organic materials. This was most likely due to ability to manufacture such implants. For example, Glück's replacement of femoral heads with ivory in 1891 (31); followed by Smith-Petersen's development of mould arthroplasty using a glass hemisphere over the femoral head in 1925, or later-on the Vitallium™ cup (a derivation of Stellite™) in 1938 (25); the first regular use of Metal-on-Metal (MoM) implants using a CoCr cup by McKee from 1953 (32); and Charnley's first generation low friction arthroplasty in 1962 (33), which used a high density polyethylene cup with a stainless steel femoral head also known as a Metal-on-Polyethylene (MoP) implant. The earlier non-organic materials (ivory and glass), while functional, would have been harder to reproduce than the later materials (metal and polyethylene), as they would not have been able to cast the implants from a mould.

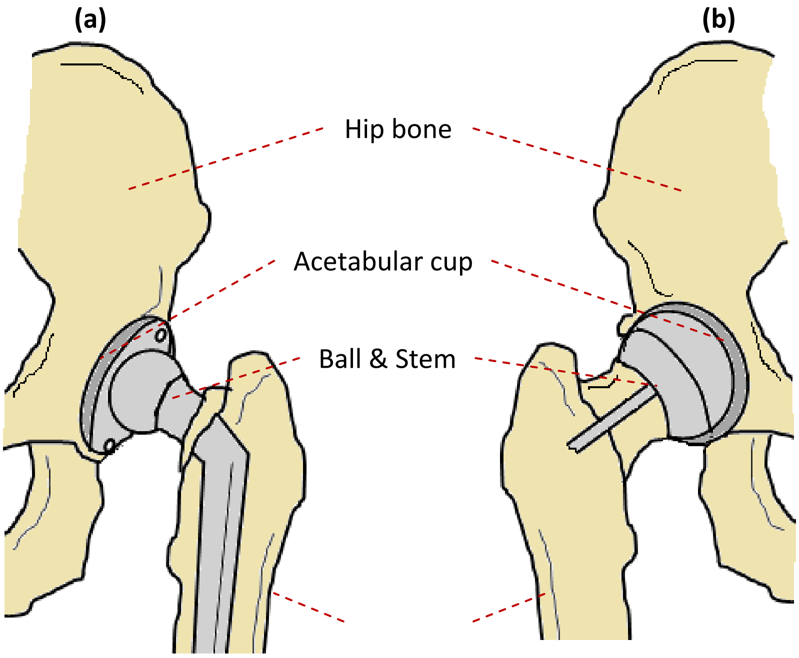

Figure 2.1: Diagram representing the two types of hip replacement performed; (a) the total hip replacement (THR), and (b) hip resurfacing.

Today there are two types of hip replacement systems; the traditional total hip replacement (THR) and the more modern hip resurfacing. A comparison of the two techniques can be seen in figure 2.1. The THR, based on Charnley's work, consists of a femoral stem (or taper) that is inserted into the femur with a femoral head (ball) attached at one end. This 'ball' fits into the acetabular cup which is placed into the acetabulum (hip socket). However this design required the removal of a substantial amount of bone from the femur to accommodate the stem. Reasonably this was seen as unfavourable (given the nature of the initial medical condition relating to bone loss and degradation), this led to the development of hip resurfacing as a bone conserving alternative to THR.

The most popular resurfacing technique is the Birmingham Hip Resurfacing (BHR), whereby the femoral head is shaped to accept a hollow cap, which acts as the ‘ball’, this is held in place by a thin pin-like stem. The ball covering then fits into an acetabular cup which is fitted into the hip socket.

In the decade following 2003, surgeons in the US performed more than 200,000 hip replacements annually, with this number increasing every year (34). From 2008 to 2013 in England and Wales, 423,715 hip replacement surgeries were performed, as reported by the UK National Joint Registry (NJR) (35).

2.2.1. Metal-on-Metal Implants

Metal-on-metal (MoM) hip implants are defined as a hip implant where the ball and acetabular cup are both made of metal materials. Generally, the ball and acetabular cup are made from a CoCr alloy. However, the stem (if present) may be either fixed to the femoral head as a single piece, and therefore the same material, or attached via a taper joint. The latter allows the potential for variation in the material used; however this leads to concerns regarding galvanic corrosion due to the close contact between two dissimilar metals (see section 2.4).

The use of MoM prostheses declined in the 1970s as concerns grew regarding their potential to produce metal debris and the associated hypersensitivity observed in local tissues during revision surgeries (36). Following this, Charnley (considered the father of total hip arthroplasty) popularised the use of a metal-on-polyethylene (MoP) implant (polyethylene acetabular cup). This implant showed early success, however concerns over large volumes of ultra-high-molecular-weight polyethylene (UHMWPE) particles were soon linked with inflammatory responses, which led to periprosthetic bone loss and aseptic loosening (13). Given the production of wear particles by MoP was reported to be much higher in number than those produced by MoM, MoM experienced a renewed interest (37). In addition, more modern MoM implants have an improved resistance to frictional and corrosion related wear (38), which suits the growing number of younger patients requiring 'higher performance' hips to maintain active lifestyles and the ageing population who wish to maintain a high quality of life.

As surgical technique became standardised and the mean patient age decreased (27), it became more apparent that a main factor in implant failure was due to the produced wear. This led to many studies comparing the best combinations variables (composition, size, cement) to produce the lowest amount of wear and best survival rates (27).

Despite the widespread use of MoM implants, they were still susceptible to early failure (39). Reports showed a significant rise in both the local and systemic levels of particulate wear debris and metal ions respectively (40). These wear products are thought to enter the pseudo-synovial fluid and trigger an immune response by the body which can result in tissue necrosis (41), pseudo-tumours (42) and osteolysis resulting in aseptic loosening (43). The latter ultimately leads to the need to surgically revise the implant, accounting for over 50% of revision surgery (35).

Concern over MoM debris (now know to be greater in volume that MoP) and revision rates, coupled with failure rates and product recall, resulted in substantial increases in legal action from recipients of MoM implants and distrust from the public (44). In 2014 the European Commission asked the Scientific

Committee on Emerging and Newly Identified Health Risks (SCENIHR) to produce a final opinion on the MoM situation. SCENIHR concluded that MoM hip implants were acceptable based on a case-by-case basis, as laid out in their report (45). The US Food and Drug Administration (FDA) were in agreement with this, as in 2016 they issued an order (46) stating that MoM devices are to remain labelled as a "higher risk" device and requires manufacturers to submit applications for approval to market existing or new MoM devices. While this decision was made in order to protect patients from adverse clinical reactions to MoM implants, it does not make a final verdict on the limits of acceptable wear generation from MoM, nor does it address the issue of wear and failure rates from other materials (35).

2.3. Modern Cobalt-Chrome Alloy Composition

There have been a few CoCr alloy compositions available since their introduction; however, for modern joint implants, the predominant CoCr alloy is a cobalt-chromium-molybdenum (CoCrMo) based alloy. This consists of two phases, the primary CoCrMo matrix and a secondary carbide phase.

In the primary Co-alloy phase the addition of Cr promotes the spontaneous formation of a passive oxide layer on the implant's surface, which consists of a mix of Cr and Co oxides. This increases the corrosion resistance by forming a barrier between the metal and the biological environment (47, 48). The Mo component increases local corrosion resistance by producing air-formed surface films (Mo oxide) (49). The secondary carbide phase is classified depending on the level of carbon added. The addition of carbon provides hardness, which contributes to wear resistance, by forming micron scale carbides at the surface

(50). For biomedical applications, there are commonly two types of CoCrMo alloys, high-carbon (>0.2%) or low-carbon (<0.05%) (51). Typically the higher carbon content shows greater tribocorrosion resistance; therefore it is the more common material for bearings in the body (52).

The metal constituents of orthopaedic implants are typically a balance of cobalt, 28 wt% Cr and 6 wt% Mo (written as Co-28Cr-6Mo). For American Society for Testing and Materials (ASTM) standards F75, F799 and F1527, there is also trace carbon (0.35 wt%), nitrogen (<0.25 wt%), nickel (<1 wt%), iron (<0.75 wt%), silicon (<1 wt%) and manganese (<1 wt%). Cast alloys (most commonly ASTM F75) can also contain tungsten (<0.2 wt%), phosphorus (<0.02 wt%), sulphur (<0.01 wt%), aluminium (<0.3 wt%) and boron (<0.01 wt%) (51).

2.4. Tribocorrosion Mechanisms

Despite the natural corrosion and wear resistant properties of CoCr alloys, they (like all metals) still succumb to degradation, thus producing a variety of particulate and ionic products. Wear mechanisms are considered any mechanism that increases the standard wear rate of an implant. Typically the main wear mechanisms for CoCrMo hip implants fall under the category of tribocorrosion. "Tribo" comes from the Greek "to rub", and "corrosion" defines the chemical and electrochemical reactions between a metal surface and its local fluid environment. As such tribocorrosion is used to describe the combination of wear (tribology) and corrosion effects and is therefore particularly relevant with regards to the material degradation of articulating metal surfaces, such as orthopaedic joint implants. Realistically, these mechanical and chemical processes cannot be separated and as such this thesis uses the term ‘surface degradation’ to encompass the material loss and production of particulate and ionic debris from both mechanical and chemical processes.

For hip implants, the most significant types of tribocorrosion mechanisms are pitting, crevice corrosion, galvanic corrosion, and fretting (53). Typically all of these mechanisms result in some form of material loss, producing products capable of interacting with the surrounding environment resulting in adverse biological reactions. However it is unlikely that an implant will fail as a direct result of corrosion, but rather due to other processes (articulating wear and fretting) that then leads to tribocorrosion resulting in further generation of ionic products. Figure 2.2 shows schematics for several of the corrosion processes described below.

Pitting corrosion occurs at localised regions of the implant, notably where there are surface defects present that compromise the integrity of the passive oxide layer or where there is a localised deviation in chemical composition. Typically, once pitting is initiated the pit becomes an anode (rules of electrolysis) and the metal surface a cathode. The internal surface of the pit undergoes dissolution and results in a net positive charge from the metal ions. Consequently, there is a net migration of negative chloride ions from the surrounding environment to preserve the charge balance and a decrease in local pH due to hydrolysis. Ultimately, these dynamics result in the pit growing and the acceleration of further metal dissolution due to the concentrations of chloride ions (53, 54).

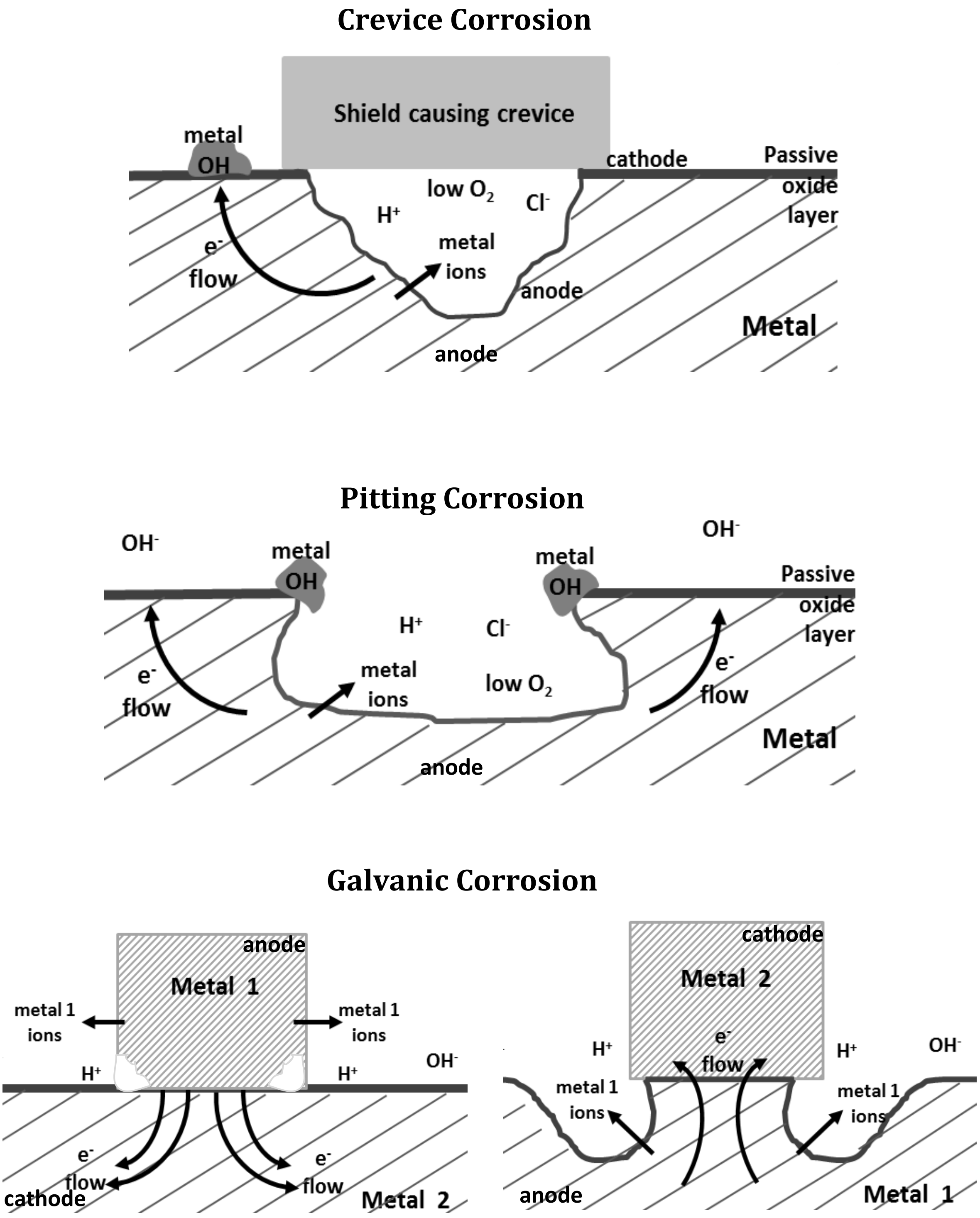

Figure 2.2: Schematic of corrosion mechanisms.

Crevice corrosion frequently occurs at sites where the working fluid is allowed to become stagnant in a confined space, such as under screws or gaps between adjoining parts, like the taper junction (only one part is required to be metal). Typically, oxygen content within the crevice decreases because the stagnant nature of the local fluid prevents diffusion into the space. Within the crevice the local chemistry of the fluid changes and, similar to pitting, there occurs dissolution which results in a net migration of chloride ions. The crevice then becomes more acidic and further accelerates dissolution (53).

Galvanic corrosion is common at the taper joint when the femoral head and stem are made of dissimilar metals, e.g. between CoCrMo and titanium (often used for the taper). A potential difference is created between these two metals in solution and allows the flow of electrons. This results in one side becoming a cathode and the other an anode, with the anodic side undergoing increased corrosion. This is an electrochemical corrosion process (54).

Fretting corrosion typically takes place at sites where micro-motions occur between two surfaces, under a sustained load, which are not designed to slide together, for example between the stem and the surrounding bone. Typically these micro-motions, which tend to result from minor hip movements, cause the loss of the passive oxide layer which results in a period of enhanced corrosion and dissolution (as described in pitting) before the re-passivation of the surface (55).

An influencing factor of tribocorrosion is the nature of the surrounding physiological environment. Typically the pH of the body is around 7.4 with a temperature of ~37°C. The main components of bodily fluids are water, oxygen, chloride and sodium ions, electrolytes, and other complex compounds. From the perspective of metallic implants, this makes the physiological environment electrochemically aggressive. For example, infections and crevices can reduce local concentrations of oxygen, and trauma and inflammation (typically after surgery) can reduce the local pH to ~5.3 (38).

No metals used in orthopaedics are completely inert; however the alloy composition is usually chosen to ensure the production of a surface ‘passive’ film capable of preventing the interactions between the metallic components from the local biological environment. From the described mechanisms it is important to note that they all involve the loss of the stable, passive oxide layer, with it being the method of depassivation that distinguishes them. Tribocorrosion will realistically be a combination of several of these mechanisms; as such there are studies which focus on creating experiments to model this tribological system.

Typically there are two types of tribological wear systems studied, two-body and three-body wear. The former, a two-body wear system, involves the friction of two surfaces against each other (usually the ball and cup), usually lubricated by a biologically relevant media (such as simulated body fluid). A three-body wear system involves the two aforementioned surfaces, with the addition of either a wear particle from the articulating surface or other particulate debris (implant cement etc.).

Mischler and Munoz (5) reviewed two-bodied systems used to simulate tribocorrosion processes in MoM hip implants, published between 2000 to 2010. Set ups included a flat pin-on-plate (4 papers), ball-on-plate (4 papers) and whole implant simulations (13 papers). From their analysis they concluded the following; wear coefficient of two-body systems (either tribometer or simulator) increased with average Hertzian contact pressure and with the CoCrMo electrode potential. The latter conclusion supports the concept that the tribocorrosion behaviour is affected by local electrochemical conditions (56)., however, their analysis included the results obtained from tribometers only. In addition the former conclusion, stating the wear coefficient is proportional to contact pressure, is derived from a scatter plot of the two variables which does not show a clear positive correlation. As such, this paper, while beneficial in its accumulation of the data, can only conclude a dependence between wear and the electrochemical environment (which was already known) and a potential relationship between contact pressure and wear coefficients (which while unsurprising is only supported when some results are neglected).

Few studies have gone as far as to simulate third-body wear; however, Halim et al. (57) showed that the articulating surface is sensitive to the presence of metallic third bodies. The presence of metal particles (CoCr or titanium (Ti)) turned the simulator lubricant black and resulted in wear rates an order of magnitude higher than with cement flakes. While this study used hip simulator stations to approximate *in vivo* conditions and wear particles with clinically relevant compositions, they failed to ensure the size range of their metal particles was clinically relevant, the particle size used was 5-400µm. Typically reported particles sizes are much smaller than this as *in vivo* studies have reported the majority of the debris as <50nm (58), while *in vitro* studies have reported 30-100nm (59). Given the particles used act as the third body in this tribocorrosion model, this disparity in particle size reduces the *in vivo* approximation of this model, yet is not addressed in the limitations.

To summarise, there are many variables that will factor into how a hip implant will wear over time, for example; THR or resurfacing, femoral head size, material composition, cement/cementless, surgeons skill in aligning the ball and cup, lubrication, and usage (number of cycles). While individually the variables and mechanisms of wear are understood, it is the interplay between them that results in a complex circumstance which ultimately affects the rate of wear and properties of the debris produced. Due to this complexity there has yet to be an *in vivo* approximation that fully accounts for all variables. As such, the limitations of a given method should be clearly stated in a publication to aid in the development testing methods, and for clarification on which variables are being tested.

2.5. Characteristics of Wear Debris

As previously stated, despite the attempt to design a wear resistant alloy, wear still occurs. The processes by which wear debris will interact with the body, detailed in section 2.7, can depend not only on the amount of wear produced but also on properties such as whether it is particulate or ionic, size and morphology, and composition/ionisation.

Due to the volume of literature produced regarding CoCr implant wear, the following section reviews the evidence that focuses on observing and characterising properties of wear debris.

2.5.1. Wear Particles

Studies investigating wear particles typically do so by characterising debris retrieved from patients during implant revision surgery (3, 4, 60, 61) or from *in vitro* simulators (3, 58, 62-64). Protocols for characterisation typically involve isolation of the particles followed by imaging and characterisation (2).

Isolation and digestion: Particles are isolated from the surrounding environment, i.e. tissues, biological fluids, artificial lubricants, using digestion protocols. The most common digestion protocols are alkaline (potassium hydroxide or sodium hydroxide) (65, 66) and enzymatic (papain or proteinase-K) (4, 59, 67, 68). Digestion protocols are typically performed alongside a series of washes, using reagents such as sodium hydroxide (69), Tris-HCL (4, 58, 68), and sodium dodecyl sulphate (58, 68), and designed to remove proteins and other biological constituents. The effects of alkaline and enzymatic protocols on the size and composition of metal wear particles were reported by Catelas et al. (67, 68). Alkaline protocols resulted in a 1.7-2.1 fold decrease in average particle size for all morphologies (round, oval and needle-shaped), whereas the enzymatic protocols did not result in a significant change compared to the control (without digestion). In addition alkaline protocols resulted in more heterogeneous particles with a reduced Cr component in comparison to the enzymatic protocols. These results were not as pronounced if the particles were generated in 95% serum showing that the method of particle generation is also a contributing factor. While this comprehensive study highlighted the deleterious effect of commonly used reagents within the literature, it did not comment on the number of steps typically involved within these protocols. Enzymatic digestion was concluded to be best suited for particle isolation; however the protocol involved 14 separate washes/steps with centrifugation. It is likely that such a high number of steps may affect the final concentration of particles. This was not assessed and as such use of this technique should be reserved for characterisation of morphology and composition only, and care taken when determining generated concentrations from after isolation and digestion.

Imaging: This involves visually observing the particles post-isolation to allow for later characterisation. Studies have employed a range of techniques with the most common being light microscopy (LM) (61), scanning electron microscopy (SEM) (58, 63), transmission electron microscopy (TEM) (3, 4, 68, 70), and automated particle sizers (71). LM is limited in its resolution, to ~200nm, by the wavelength of light, hence the use of electron microscopy. SEM and TEM use electrons in vacuum and are capable of nanometre and sub-nanometre resolution, respectively (72). Other techniques, such as dynamic light scattering (DLS) are available, which measure the intensity of scattered laser light by the particles in suspension. This technique is able to resolve distributions down to 2nm (73) and is more suited to analysing polydisperse samples, however it is limited by low resolution for closely spaced size populations.

Characterisation: The most common characteristic reported is particle size, usually given as the largest dimension of the particle or equivalent circle diameter. The latter is the size reported by techniques such as dynamic light scattering (DLS), as size is not measured directly, but rather calculated assuming a spherical morphology. This technique is well suited to examining polydisperse distributions of samples down to 2nm by analysing the scattering of laser light due to particles undergoing Brownian motion (73). Secondary characteristics reported tend to be shape (usually a qualitative assessment) and chemical composition (61) (usually x-ray spectroscopy) to determine elements present. While it has been shown that metal particle populations are not solely circular and do exist with round, oval or needle-shaped morphologies (6, 64, 67).

In the literature a range of particle sizes and morphologies have been reported for MoM systems. Langkamer et al, (61) analysed post-mortem tissue close to the implant with light microscopy and found 1-2μm round and 2μm long needle-like particles in cells. Shahgaldi et al. (6) used histological, TEM and energy-dispersive x-ray spectroscopy (EDX) (analytical technique used to determine elemental composition) to evaluate the particles in local tissues and found spherical particles ranging from <1-4μm from CoCr implants. Doorn et al. (4) used enzymatic digestion on periprosthetic tissue from 13 patients to isolate particles for imaging using TEM. Particles observed ranged from ~5-800nm, the majority were <50nm, and exhibited round to oval morphologies, with EDX reporting chromium oxide and crystalline CoCr particles.

Later studies have reported smaller sizes than those stated above, for example Pourzal et al. (64) used TEM and EDX to show a CoCr cylinder vs. bar system produced 100-500nm round and shard-like particles under 3-body abrasive wear. Their hip simulator produced two populations of oval particles, 15-30nm (Cr oxide) and 30-80nm (partially oxidised with some Co).

As techniques and medical interest have advanced, the characteristics reported have progressed from simply "micron sized particles", to descriptions of multiple populations of varying size and morphology distributions with complex compositions that varies from the bulk (CoCrMo) implant composition. Given the relationship between particle characteristics and bioreactivity (depicted in figure 2.3), this evolution in the observed characteristics of implant derived debris has a direct impact on the potential understanding of the biological response and subsequent patient outcomes. This provides justification for the continued analysis of implant derived characteristics, particularly chemical composition. For size and morphology there exists many studies linked to developments of model tribological systems (3, 52, 57, 59, 62, 66), however the evaluation of chemical composition is not as rigorously investigated (59, 68, 74). As such, part of this thesis aims to present an approach for *in situ* determination of the chemical composition of implant derived debris that goes beyond stating "exhibits some Co or Cr" (64). While such a conclusion provides an indication to the dominant chemical composition of the debris, the methods used work by averages (75-77) and much of the chemical variation is lost (further discussed in section 3.2.2).

To summarise, unsurprisingly tribological properties of the implant will impact upon the characteristics and number of generated wear particles. Typically severe wear conditions result in a larger number of particles, usually bigger and irregular, and as such some characteristics may be indicative not only the severity but also of the wear mechanisms taking place (2). Figure 2.3 gives an overview of the interrelations between measured characteristics of metal wear particles and the mechanisms and biological responses investigated. Analysing

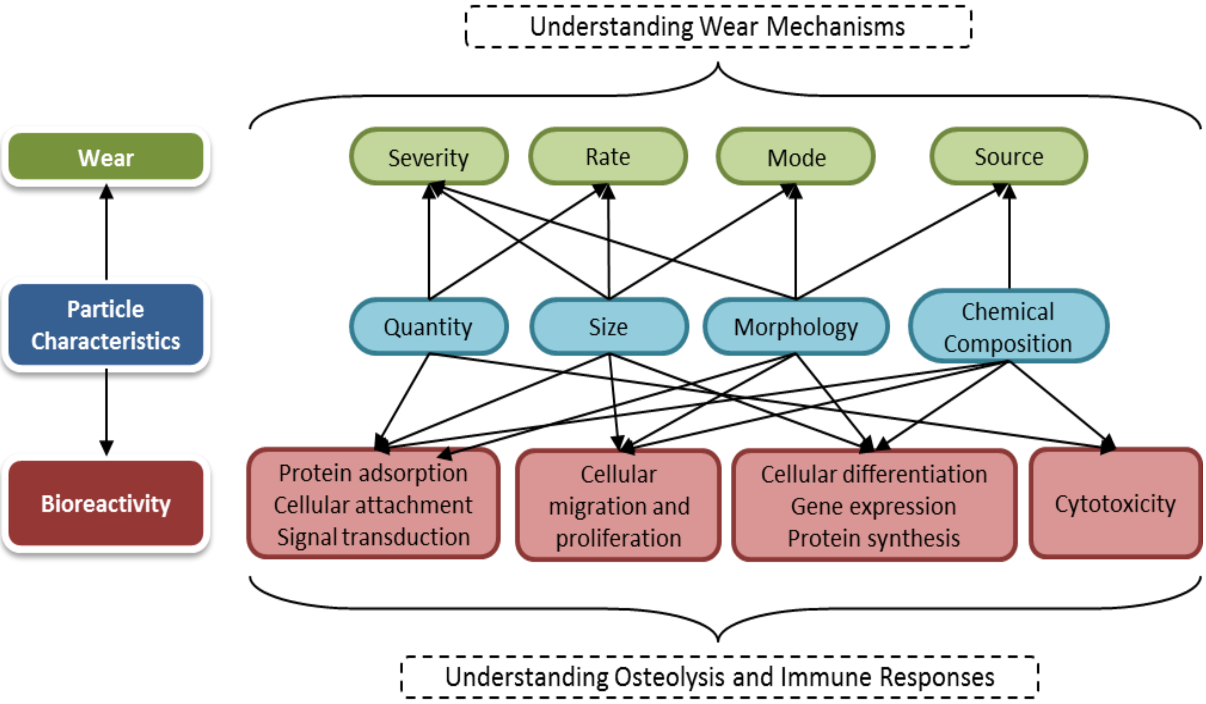

Figure 2.3: This figure depicts the relations between the main characteristics of wear particles and the information regarding the wear mechanisms and biological activity that can be typically obtained. Created by Billi et al., this infographic was produced as part of a literature review of the most commonly-used protocols for characterising metal wear particles. The interrelations between measured characteristics and the mechanisms and biological responses investigated are shown with black arrows.

(Used under the Creative Commons Licence from Billi et al.)

generated particles informs further studies in a number of ways, for example; providing a set of parameters for modelling debris particles in *in vitro* studies; and allowing for comparisons to be made between simulator generated particles and *ex vivo* particles to determine wear mechanisms. These interrelated areas of research must be considered side-by-side if the research is to develop and aid the understanding of host response and the choice of future designs and materials for the next generation of arthroplasty devices.

2.5.2. Co and Cr ions

Co and Cr ions are generated at various sites both near and far from the implant itself, through either corrosion of the implant or dissolution of wear particles, respectively. Previous studies have been concerned with determining correlations between the levels of Co and Cr ions detected in periphery fluids and adverse reactions. This was to determine whether ion level monitoring could be used as an indicator of the degree of implant deterioration and used to inform clinical decisions (i.e. revision) (78).

The concentrations of Co and Cr in blood, blood serum and urine have been investigated (40, 61, 79-85) for both well and poorly functioning implants, as well as a range of implant types and sizes. The table in figure 2.4 summarises the detected concentrations reported for Co and Cr.

A detailed review of 104 studies (80) reported the median Co serum concentrations as ~0.65-1.7μg/L for MoM small-head diameter (<36mm) THA, 0.7-5.38 μg/L for large-head diameter (≥36mm) THR, and 1.12-4.28μg/L for hip resurfacing at 6-24 months. Another review (83) calculated the mean ion levels across 43 studies and found the average Co concentration was 0.3-7.5μg/L in serum and 0.7-3.4μg/L in blood, while the Cr ranged between 0.8-5.1μg/L for serum and 0.5-2.5μg/L for blood. However, these larger-scale reviews report an averaged Co or Cr concentration, and while this gives an indication of the metal ion levels for the majority of revisions, it doesn't highlight the metal ion levels for the most serious cases.

Case Study/Review	**Cobalt Ion Concentrations**	**Chromium Ion Concentrations**
Hartmann et al. [2013] Review of 104 studies with revisions at 6-24 months (80)	Serum [mean]: 0.65-1.7 μg/L [SD-THR]** 0.7-5.38 μg/L [LD-THR]*** 1.12-4.28 μg/L [resurfaced]	Not reported
Jantzen et al. [2013] Review of 43 studies of revisions (83)	Serum [mean]: 0.3-7.5 μg/L Blood [mean]: 0.7-3.4 μg/L	Serum [mean]: 0.5-5.1 μg/L Blood [mean]: 0.5-2.5 μg/L
Sampson et al. [2012] Female [29yrs] Silent osteolysis from BHR, revision at 5yrs (87)	Synovial Fluid: 745 μg/L [pre-revision]	Synovial Fluid: 11850 μg/L [pre-revision]
Sampson et al. [2012] Male [65yrs] Silent osteolysis from BHR, revision at 5yrs (87)	Blood: 71.4 μg/L [pre-revision]	Blood: 36.3 μg/L [pre-revision]
Sampson et al. [2012] Female [54yrs] Loss of function and silent muscle necrosis from 2yr old resurfacing (87)	Blood: 386.5 μg/L Synovial Fluid: 12.2 μg/L	Blood: 140 μg/L Synovial Fluid: 263.3 μg/L
Langton et al. [2013] Male [55yrs] Minimal discomfort, widespread osteolysis (see figure 2.5) (84)	Blood: 217 μg/L [pre-revision]	Not reported
Dobbs et al. [1980] Female [81yrs] Deceased with MoM and MoP implants (90)	Synovial Fluid: 12.94 ppm* Synovial Membrane: 62.6 ppm* Granuloma: 193.1 ppm* Femur Tissue: 6.9 ppm*	Synovial Fluid: 63.32 ppm* Synovial Membrane: 327 ppm* Granuloma: 322.8 ppm* Femur Tissue: 5.52 ppm*

*[1000 μg/L = 1ppm]
**Small-head diameter – Total hip replacement (<36 mm) (86)
***Large-head diameter – Total hip replacement (≥36 mm) (86)

Figure 2.4: A summary of case studies and review regarding poorly functioning hip implants and the levels of cobalt and chromium ions measured in surrounding tissues and fluids.

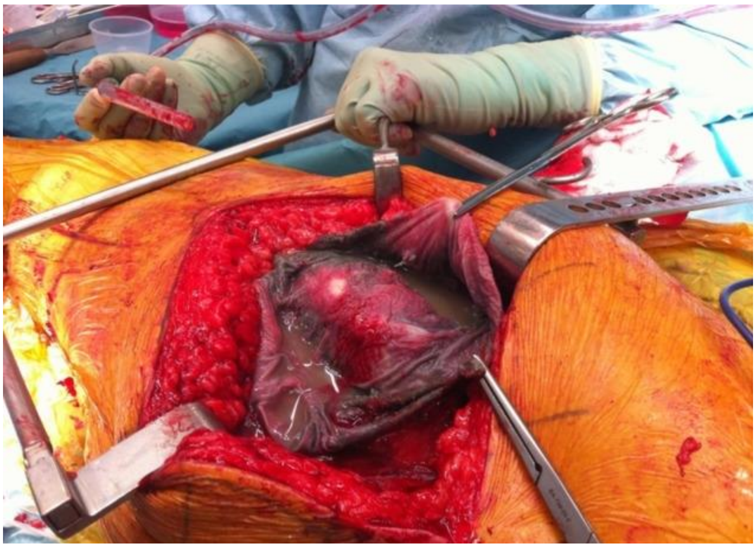

Figure 2.5: This figure shows abnormal fluid and metal staining of the tissues surrounding the implant. In addition the patient was found to have extensive osteolysis in the acetabular and femoral regions.

Permissions obtained to use figure from BMJ open. Image from Langton et al. (84)

Other papers have presented case studies of poorly functioning hips with much higher levels of metal ions measured. For example, a 29yr old female with silent osteolysis from a BHR at 5yrs measured 11,850μg/L of Cr and 745μg/L of Co in synovial fluid (87). A 65yr old male, again with silent osteolysis from a BHR at 5yrs, measured 36.3μg/L for Cr and 71.4μg/L for Co in blood (87). A 54yr old female with a 2yr old resurfaced hip suffered rapid deterioration of function and silent muscle necrosis. Blood levels measured 140μg/L for Cr and 386.5μg/L for Co, synovial fluid measured 263.3mg/L for Cr and 12.2mg/L for Co (87). A 55yr old male with minimal discomfort, turned out have widespread osteolysis (see figure 2.5) and measured a blood level of 217μg/L of Co (84).

Typically the causes of the metal ion generation measured in these case studies are complex and the focus of these publications was to determine the metal ion levels in patients with poorly functioning hips, rather than the cause of corrosion. Factors such as implant type (total replacement vs resurfacing), degree of use, amount of particle dissolution and implant positioning will play a role in the mechanisms of tribocorrosion taking place. However it was stated for the 54yr old female that the main contributing factor was excessive edge loading due to misalignment during initial implantation, resulting 100x greater generation of debris than simulation studies (87).

The aforementioned literature provides an example of the metal ion concentrations measured for various patients and/or implant groups; however, the data must be read with care (as stated in the reviews) as the methods and units of measurement vary. The lack of consensus regarding units of measurement slows direct comparison across the literature. While some units are interchangeable (i.e. μg/L = parts per billion (ppb), or mg/L = parts per million (ppm)) others (i.e. nanomoles per litre (nmol/L)) require division by the atomic weight of the target ion. In addition, the time from implantation to assessment varies with little justification. Given the rate of metal release can vary depending on implantation time this will affect the measured concentrations and again impact upon the ability for direct comparison. It is accepted that an implant will experience its highest rate of wear in for the first 0.5-1million cycles (known as run in phase), with a subsequently lower wear rate following this (known as steady state phase) (39). As a final point, many methods of analysis measure the concentration of metal ions in the supernatant component of centrifuged fluids. Therefore any metal ions present in the pellet component, due to being either actively taken up by cells, precipitated or transported to other systems - i.e. the lymphatic system (88, 89) and surrounding tissues/organs (79) - are unaccounted for. It is therefore reasonable to suggest that the quantification of only freely circulating metal ions within blood and urine (remaining in the supernatant after centrifugation) may underestimate the total amount of metal ions released into the body (90). Despite this however, the technique of metal ion level monitoring is still a good clinical indicator of whether abnormal wear is likely to be occurring.

Few studies (79, 91) have looked at either the ion levels within the surrounding tissues, typically due to the need for excessive tissue sampling, or have analysed the total metal contained within such samples, rather than just free circulating ions. Dobbs et al. (79) measured Co, Cr and Mo levels in a range of organs and tissue sites from a deceased 81yr old female with MoM and MoP hip implants. The metal ion concentrations were reported as: joint fluid = 12.94ppm Co and 63.32ppm Cr; synovial membrane[1] = 62.6ppm Co and 327ppm Cr; granuloma[2] = 193.1ppm Co and 322.8pm Cr; and tissue from the femur = 6.9ppm Co and 5.52ppm Cr. All measurements were performed by irradiating the samples for 100hrs and analysed using gamma spectrometry after 5 days to determine the concentrations of specific metals, including Co and Cr, present. This technique measured the total metal load within the samples, in particular the joint (synovial) fluid. Comparing the Co and Cr levels within this study to others, measuring only free circulating ions, an increase can be seen primarily in the concentration of Cr present (see figure 2.4). This further supports the concept that the primary method of determining metal load on the body, while providing a

---

[1] Tissue from the capsule or "sheath" surrounding the joint

[2] Collection of immune cells, such as macrophages, that forms as the immune system attempts to segregate foreign substances from surrounding cells

clinical indication of implant degradation, underestimates the local levels of metal products when only observing free circulating ions.

Furthermore, Co and Cr concentrations found in the tissues local to the implant have been found to be higher than those at a distance from the implant, i.e. synovial membrane vs. tissue from the femur. In addition, the high concentrations found in a granuloma, highlight the potential for localised releases of high concentrations of Co and Cr into the surrounding tissue. This again provides evidence that metal levels in periphery fluids (blood and urine) cannot fully represent the local levels of metal products. Thus published values need to be clearer in stating that the values reported from methods involving centrifugal techniques are of free circulating ions, not simply metal ion levels released from an implant.

2.5.3. Other Metal Species

There are studies (75, 77, 92) observing the speciation of Co and Cr within surrounding tissues, using x-ray spectroscopy techniques on *ex vivo* tissue. Typically these samples are cut into thin (several microns) sections, and elemental analysis is performed to determine the distribution and speciation of metals present. Generally, it is reported that hydroxide and phosphate species are detected alongside the metallic debris (see chapter 3 for further discussion). However there are two shortcomings to these investigations; (1) the cross-section over which speciation measurements are performed is typically several microns diameter and at single points, which disregards any potential small scale variations in species, and (2) it is generally implied that the detected species originate as corrosion by-products (particularly the hydroxide species), and little thought is given to the concept of precipitation.

The first shortcoming, regarding overlooking small scale variations in metal species, forms the motivation for the research addressed in chapter 6, and the literature for which is presented in more detail in the following chapter. Regarding the second shortcoming, the observation of species other than oxides/hydroxides (i.e. phosphates) suggests precipitation processes are occurring. Given the diverse biochemical environment and the prevalence of corrosion processes that promote dissolution, it is unsurprising that there are multiple pathways for the generation of degradation products.

One thesis (85), which formed two papers (93, 94), investigated the precipitation of metal ions by adding Co(II) and Cr(III) respectively into cell culture media, with and without the presence of foetal bovine serum (FBS) or human serum (HS). Techniques such as scanning and transmission electron microscopy (SEM and TEM) were used to observe size and morphology, Fourier transform infra-red (FTIR) spectroscopy was used to evaluate composition, and gel electrophoresis with mass spectrometry was performed to determine which proteins were bound to the complexes that precipitated. It was determined that Co(II) ions would not precipitate, however Cr(III) ions did so readily within 1hr. The size of the particles ranged from 60-100nm, with variation occurring depending on the composition of the media used. FTIR showed amino acids and phosphate groups present in the Cr(III) complexes, interpreted as organic and inorganic phases respectively.

This work then progressed to using a proteomic approach to investigate the interaction with serum proteins and simple cellular uptake experiments. It was shown that albumin was the only protein from FBS that interacted with the Cr(III) complexes, however a range of proteins did so from HS. Also, the complexes formed in HS were more readily up taken by macrophage cells than the corresponding FBS-complexes due to bound HS-proteins facilitating phagocytosis. This is significant as the majority of studies focus on the biological reaction to free metal ions and metallic particles only. There are, however, a few exceptions of those using chromium orthophosphate (17, 18) to assess the effect on gene expression of osteoblasts, however no consideration was given to the presence of bound proteins as the chromium orthophosphate was purchased, and thus contained no organic phase.

As mentioned in the previous sections, techniques for investigating wear debris centres around centrifugation followed by Co and Cr measurements within the supernatant or isolation and size analysis of the pellet. It ignores the prospect of precipitation. While the work by Tkaczyk et al. (85) proved that Cr(III) precipitated complexes are an important consideration for the issue of CoCrMo implant wear, the idea of Cr(III) precipitation has not been pursued nearly a decade on. This motivated the second research question which is addressed in chapter 5 - what does precipitation mean for the understanding of available wear products?

2.6. Co and Cr in the Body

2.6.1. Cobalt

Co is an essential trace element for both humans and animals as the integral constituent of the vitamin B12, playing a role in forming amino acids and producing red blood cells. The recommended dietary allowance for vitamin B12 is 2µg/day however it is generally considered nontoxic at higher levels (95). The form of Co can be either organic or inorganic, and it is the organic form that is essential, while the inorganic forms (in ionic form) are generally toxic (96). The main ways for Co to enter the body is through diet (present within foods), respiratory system (generally through employment in the metal industry), skin (environmental pollution and workers in metal industry) and biomaterials (such as implants).

The Agency for Toxic Substances & Disease Registry (ATSDR) reports the hazardous health effects of exposure to Co - when absorbed through the respiratory system Co can cause effects such as pneumonia and asthma. Uptake of high concentrations may also result in heart, liver and kidney problems, as well as hypersensitivity (97). Perhaps most seriously, Co compounds are listed by the International Agency for Research on Cancer (IARC) as 'agents which are possibly carcinogenic to humans' (98).

2.6.2. Chromium

Like Co, Cr is an essential trace element, however in higher concentrations or certain forms it is particularly harmful. In small amounts, Cr helps the metabolism and the regulation/transportation of blood sugar and a deficiency can result in symptoms similar to type-2 diabetes. The adequate daily intake has been recommended to be between 25-35µg/day for men and 21-25µg/day for women (99). At higher concentrations, it is primarily Cr(VI) that is considered toxic, as Cr(III) is poorly absorbed.

The ATSDR reports a list of respiratory issues from Cr dust including; asthma and ulceration, skin exposure demonstrate rashes and inflammatory responses, and ingestion can cause damage to the throat, kidneys and circulatory system. Finally, the IARC has listed Cr(VI) as 'carcinogenic to humans' (100).

2.7. Biological Response to CoCr Wear Products

There have been many long term studies and reviews in the past two decades showing that joint arthroplasty is not permanent and that all total joint replacements eventually result in implant loosening, typically due to osteolysis (9, 101-104). Tribocorrosion processes continuously produce debris (ions and particles) over the lifetime of the implant. It is acknowledged that this debris is involved in aseptic loosening (104), usually through particulate phagocytosis and activation of macrophages and osteoclasts (103). However there is no over-arching and universally accepted mechanism, just many studies all investigating parts of the process from various aspects (103, 104). Figure 2.6 provides a schematic of signalling pathways involved in the inflammatory response to CoCr debris (105).

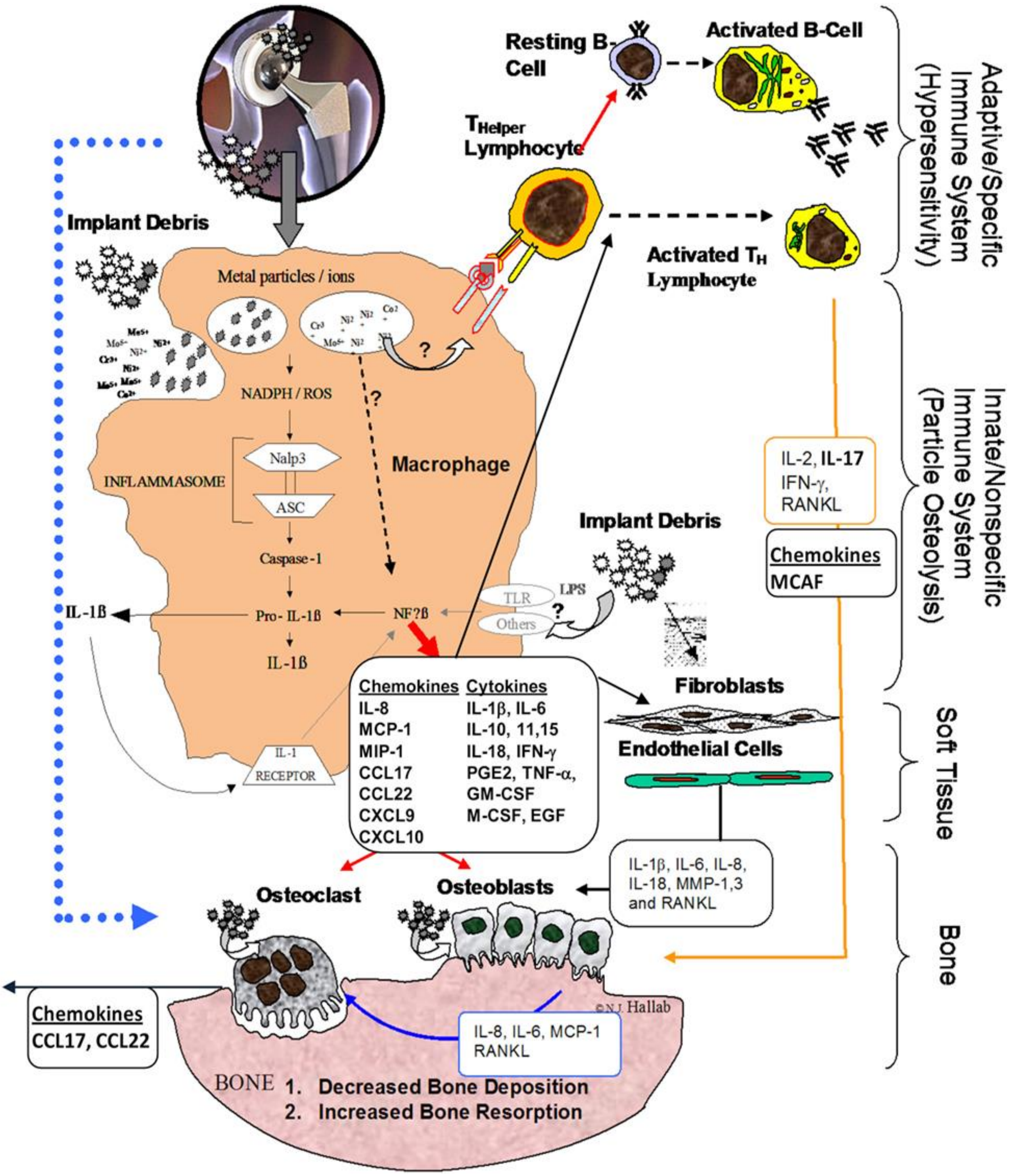

Figure 2.6: This figure depicts a schematic showing the complex nature of the signalling pathways induced by cobalt-chromium implant debris resulting in inflammation and contributing to osteolysis.

This figure is used under the Creative Commons Licence from: Hallab N et al. (105) Where original courtesy was attributed to Bioengineering Solutions Inc.

A major cell type involved in the osteolytic process is the macrophage (10). *In vitro* studies have shown that after ingesting debris (foreign material), macrophages expand and their diameters increase from 10-20μm up to 40-50μm (106). The interaction between macrophage and particle results in the release of an array of pro-inflammatory cell signalling molecules and cytokines, such as tumour necrosis factor alpha (TNF-α) (involved in systemic inflammation) and monocyte chemotactic protein-1 (MCP-1) (involved in recruiting osteoclasts and monocytes) (103, 104). In addition to cytokine production macrophages can form granulomas through a complex interaction between the cells, wear debris, and an array of biological mediators (107). A granuloma is essentially an aggregation of cells that separates ("walls off") large foreign bodies (wear particles) from the surrounding environment if they are too large for phagocytosis. Ultimately the granuloma will progress towards fibrosis (thickening of tissue) (107). As seen in the previous section they have been found to contain extremely high concentrations of Co and Cr (79).

There are several studies examining the role of pro-inflammatory marker MCP-1 and osteoclasts in osteolysis, primarily because MCP-1 is involved with the recruitment of osteoclasts which are in turn responsible for active bone resorption. Some studies looked at culturing monocytes (osteoclast pre-cursors) in the presence of CoCr debris and observed cellular toxicity resulting in a decrease in osteoclast formation and consequently a reduction in bone resorption (15). Other studies expanded this to look at the expression of RANK and RANKL[3].

---

[3] RANK is a cell-surface receptor on osteoclast pre-cursors. RANKL is a ligand that is expressed to bind to RANK, promoting osteoclast differentiation.

It was shown that while other types of wear debris increase osteoclastogenesis (development of osteoclasts), this did not occur for CoCr debris (108). It was therefore suggested that, rather than the RANK-RANKL pathway, recruitment of osteoclasts might be caused by the inflammatory cytokines (i.e. MCP-1) (109). A schematic of potential immune pathways resulting from CoCr debris is depicted in figure 2.6.

Other studies have shown that CoCr debris causes dysregulation of the homeostasis between osteoblasts (bone-forming cells) and osteoclasts could contribute to the osteolytic process. There are reports of CoCr inhibiting osteocalcin (protein important for bone metabolism) impeding the mineralisation of bone (110, 111), reduced alkaline phosphatase activity (essential for promotion of mineralisation) measured after incubation of osteoblasts with CoCr ions (112), and a decrease in the synthesis of collagen type I (main component of the organic matrix of bone, see section 3.1) after exposure to Co and Cr particles (10μg/L) and ions (100μg/L) (113, 114).

The literature regarding the cellular response to wear debris is extensive. Current research suggests that the progression of periprosthetic osteolysis is dictated by a number of factors including composition, metal concentrations, particle morphology (10), and complicated by variation in cellular response due to different donors (8). Despite being extensive, the research so far largely focuses on the effects of exposure to wear particles and ions on 2D cell cultures or in blood. While this is critical in determining pathways for immune response, it does not consider the possibility of any effects to the extracellular matrix caused by metal degradation products. The extracellular matrix is not only in contact with much of the implant, but also plays a crucial role in providing the physical and chemical cues to direct cell function and fate. As such this motivated the first research question regarding the effect of metal ions on the extracellular matrix.

Chapter 3

Literature Review Part 2

3.1. Collagen Structure

Type I collagen is present in many tissues within the human body as it forms the basis of the extracellular matrix and is the most abundant component of the organic matrix of bone (115).

Collagen type I is defined by a right-handed triple helical structure that comprises a motif of three polypeptides (procollagen) (see figure 3.1). These polypeptides consist of two α(1)-chains and one α(2)-chain bound together via hydrogen bonding in a characteristic left-handed triple helical conformation. This is allowed due to the repetitive glycine (Gly)-X-Y triplet where X and Y are usually proline and hydroxyproline (116). This is then secreted from the cell by exocytosis. Once in the extracellular matrix, these procollagen structures undergo the loss of their propeptide ends, leading to self-assembly into fibrils where the collagen molecules super twist and are quasi-hexagonally stacked, via covalent and hydrogen bonding. The axial staggering formed from the super twist results in a characteristic feature of repeating light and dark regions referred to as the collagen 'D-banding/periodicity'. The literature reports D-banding to be equal to 67nm, or ~0.22x length of collagen molecule (as they are ~4.5 D long) (117). Collagen fibres are then formed through the aggregation of collagen fibrils, via covalent bonding. The fibrils range from 50-200nm thick, while the fibres are

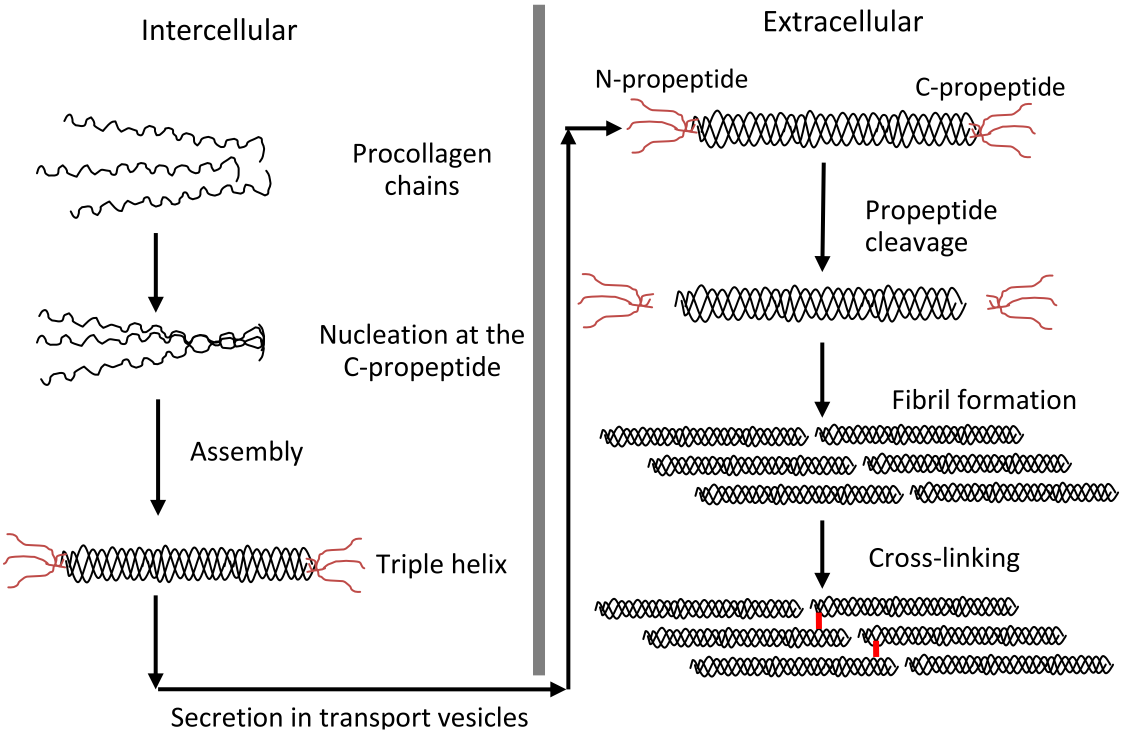

Figure 3.1: The formation process of collagen fibres begins inside cells where the triple helix is formed prior to secretion into the extracellular environment where they self-assemble and cross link to form fibres

typically 1-20μm thick (115). The final collagen matrix will then undergo mineralisation to form bone (118).

The collagen chains contain negatively charged amino acid residues, which can interact with water molecules, forming a dense hydration layer by strongly binding with the hydroxyl and carbonyl groups of glycine and hydroxyproline in collagen (119, 120). Initial hydration occurs when water molecules bind first to the hydrophilic amino acid residues, and then to the non-polar regions of the collagen (120). It is assumed that hydrogen bonding of the water bridges between neighbouring collagen chains contributes to matrix self-assembly. Intra-chain bridges are usually 2-3 molecules long, dependent on the local environment and can form through three potential routes; either between a carboxyl and hydroxyl group [C-O---Water---O=C]; between two carboxyl groups [C=O---Water---O=C]; or between two hydroxyl groups [C-O---Water---O-C] (119). It is likely that any interaction with collagen may occur either directly with the collagen fibrils or with the water molecules.

Given that the highly ordered hierarchical structure of bone is critical to maintaining bone mechanical properties and the extracellular matrix itself influences cellular behaviour; any modification to this may impact upon the body's response to an implant.

3.1.1. Effect of Co and Cr on Collagen

Literature evaluating the impact Co and Cr products have on collagen is not as extensive as those focusing on the effects ions and particles have on 2D cell cultures. This, while critical in determining potential pathways for immune response, does not consider the effects on the extracellular matrix. This is relevant to research regarding implants as it is the extracellular microenvironment that is in contact with the implant and plays a crucial role in providing the physiochemical cues to direct cell function.

Available literature investigating the effect of Co or Cr on collagen is limited to the effect of Co and Cr products the cellular expression of collagen (113, 121), with a single paper evaluating the effect CoCr particles had on an organ culture model (11).

Allen et al. (121) exposed osteoblast-like cell lines to Co, Cr and CoCr particles and showed that Co inhibited type I collagen synthesis, while Cr and CoCr showed no inhibition. However, at higher concentrations, Cr and CoCr inhibited the expression of osteocalcin, a protein which comprises ~25% of the non-collagenous proteins in bone. Anissian et al. (113) exposed human osteoblast-like cells to Co ions. The Co ion-enriched culture media reduced the expression of type I collagen. It was found however that Co concentrations <0.17mmol/mL had no significant effect on human osteoblast function. Papageorgiou et al. (11) used an organ culture model of porcine dura mater (thick membrane surrounding spinal cord) and treated it with doses of CoCr nanoparticles. After 7 days the basal layer of collagen in the model appeared loosened.

For studies evaluating the effect Co or Cr had on the actual formation and structure of collagen, the leather tanning industry was the only source of insight. Since collagen is a major component in skin, the tanning industry has had a history of using various techniques to crosslink collagen to form leather. Cr(III) is one such metal ion that is often used (122, 123). It was shown that Cr(III) does not destroy the triple helix or change the D-banding. However, a small conformational distortion (decrease in the ratio of positive-to-negative peak) suggested that Cr(III) displaces the bound water resulting in further stabilisation. This dehydration of the collagen was supported by atomic force microscopy, which depicted fibril aggregation. In addition, an increase in Cr(III) corresponded with a decrease in the intermolecular lateral packing (perpendicular to the length of fibres). It was demonstrated that nanometre-sized clusters formed between the fibrils resulting in inter-fibrillar crosslinking.

A few studies (124, 125) have assessed the effects of metal ions on collagen mineralisation (bone formation). They found Co and Cr substituted the calcium ions to become fully incorporated into the hydroxyapatite. The hydroxyapatite crystals also showed increases in both size and symmetry, and which size has been associated with increased brittleness and reduced resistance to load (124).

These studies show the potential for metal ions to interact with and influence parts of the collagen pathway, whether that be the cellular expression (113, 121), structure post cross-linking (11) or during mineralisation (124). However, while the effect of Cr ions on the structure of collagen is discussed in the leather industry (122, 123), the effect of Co ions has not been investigated. Consequently, this provided the motivation for the subject of the first research question – do cobalt ions affect collagen formation? The focus was primarily on Co due to the propensity for Cr(III) ions to readily precipitate (85).

3.2. Analysis techniques for collagen

3.2.1. Circular Dichroism

Circular dichroism (CD) is the difference between the absorption in the left and right handed circularly polarised light that occurs when molecules contain light absorbing groups (126). CD spectroscopy is a technique used to analyse the secondary structure (or conformation) of macromolecules by examining the primary absorbing group within an observed region. For collagen, it is the amine group of the peptide bond in the UV region that is interrogated (127). The limitation is that only changes close to the protein backbone can be observed

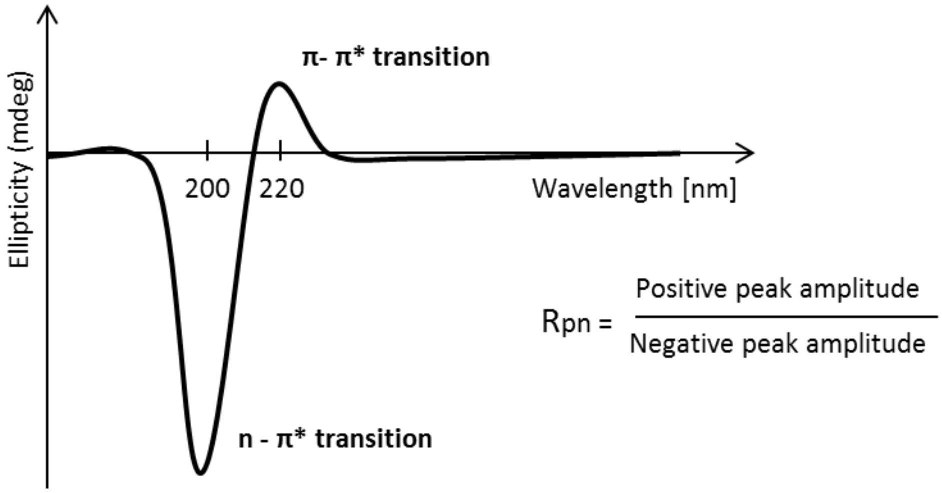

Figure 3.2: Characteristic circular dichroism profile of fully formed collagen. The positive and negative peaks are located around 220 and 200nm respectfully.

rather than smaller changes caused by modifications to any side chains. However, the collagen backbone has a distinctive confirmation which is characterised by a positive peak (around ~220nm) and a large negative peak (around ~200nm), attributed to n - π* and π- π* transitions (126) respectively (figure 3.2). While the presence of these positive and negative peaks relates to the triple helix and the random coil conformations respectively (128); it is the ratio of their amplitudes which is often used to measure the triple helix content. The literature states that for collagen, ratios close to 0.12 supports a fully helical structure (129)

Changes to the characteristic peaks are typically due to structural changes in the proteins. For example, one study (127) combined collagenase (enzyme which breaks collagen peptide bonds) with type I collagen in order to analyse the CD spectra as the collagen denatured. Increasing the incubation time resulted in a reduction of the negative peak intensity. Another study (129), involving modifying triple-helix peptides and studying the resulting effect of adding trimethylamine N-oxide, found that the amplitude of the CD positive peak

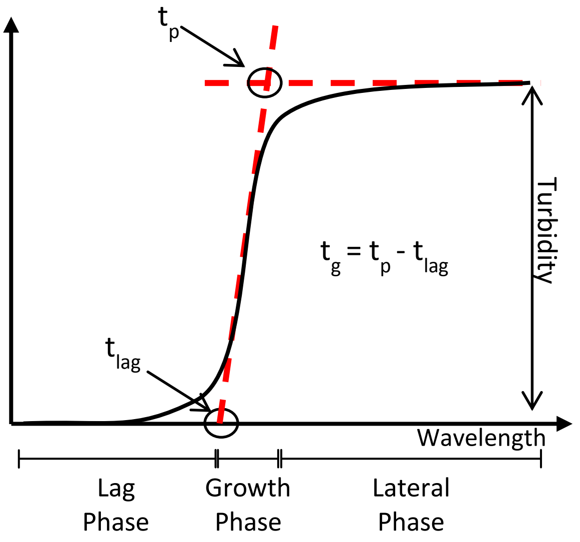

Figure 3.3: Characteristic profile for collagen fibrillogenesis showing the 3 phases: Initial lag followed by the steep growth phase, where collagen self-assembles to form fibres, and finally the lateral plateau phase.

increased, likely due to tighter packing of the triple-helix of their collagenous peptides. These studies show how changes in the CD spectra can suggest changes in the protein structure of collagen which can aid the evaluation of fibrillogenesis.

3.2.2. Turbidity Curves

Collagen fibrillogenesis, the next step after the formation of the triple-helix, is the assembly of these helices into collagen fibrils, then fibres. Fibrillogenesis can be monitored by observing the absorbance of a given wavelength through the collagen sample on an ultraviolet-visible (UV-Vis) spectrometer. As the collagen begins self-assembly the fibrils will occlude the light path resulting in increased absorbance over time. This is recorded on a turbidity-time graph, of which the profile for type I collagen is well documented (130).

Current evidence supports the theory of a nucleation and growth process (131) as the absorbance curve has a sigmoidal profile. For collagen type I there are generally three phases to consider, which are indicated in figure 3.3.

Lag Phase – The aggregation of monomeric collagen occurs to form 'nuclei', no aggregation into fibrils occurs meaning no significant change in absorbance. This is observed as the time taken (t_{lag}) for an increase in the absorbance to begin, as recorded on the turbidity profile (figure 3.3).

Growth Phase – The aggregation of 'nuclei' forming fibrils lead to a rapid and linear increase in absorbance. This is characterised as the time taken for the steep increase in absorbance to occur (t_g), and calculated using the following equation:

$$t_g = t_p - t_{lag}$$

t_g – growth phase, t_p – lateral phase, t_{lag} – lag phase

Lateral Phase – gelation occurs due to fibril association causing no further change in absorbance. This phase is said to occur once the turbidity profile has reached a horizontal plateau, the height of which for a given concentration has been associated with final fibril diameter (132, 133). Given that a larger fibril diameter is likely to result in more occlusion of the light path it is unsurprising that this would result in an increased absorbance, and thus plateau height.

3.2.3. Small deformation oscillatory rheology

Collagen is characterised as a viscoelastic material (134, 135), and as such rheological methods can be used to characterise mechanical properties. These methods can involve observing a materials response to changes in stress or strain. Common methods in the literature (136, 137), with respect to hydrogels, involve exposing a sample to small-deformation oscillations to determine the storage modulus (G').

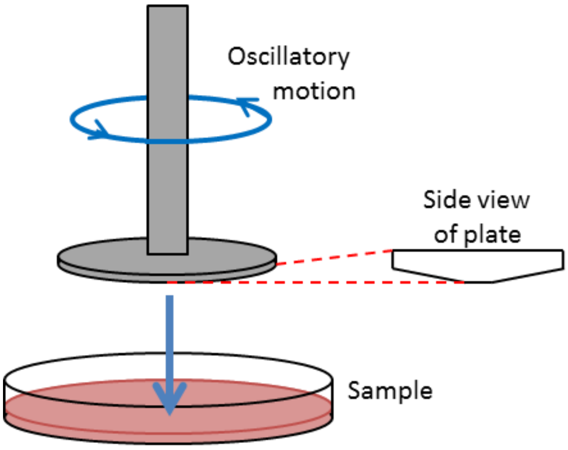

Figure 3.4: Experimental schematic for small deformation oscillatory rheology. The cone-shaped plate is brought into contact with the surface of the sample and small amplitude oscillations are applied.

Small-deformation oscillations, also known as oscillatory shear, involve subjecting a sample to oscillatory stress and measuring the elastic response. The sample is placed between a flat plate and a cone, which is then rotated at a given amplitude while in contact with the sample's surface (figure 3.4). The resistance to this oscillatory deformation is measured and the storage modulus determined, which describes the elastic properties and as such is an indicator of stiffness, as it describes the material's resistance to deformation (138).

3.3. Imaging of CoCr in *ex vivo* tissue

As mentioned in section 2.5, the analysis of wear debris from patients requires the isolation of the debris (particulate or ionic) from the surrounding biological component (tissue or fluid). This is typically done through digestion followed by centrifugation. While effective for wear debris characterisation, this method prevents information regarding the distribution of Co and Cr with respect to tissue and cellular structures. To preserve the spatial information, thin sections of tissue have been imaged via histology (41, 82, 139), SEM (6, 82, 139) and TEM (4, 6, 139) showing small black/opaque particles. It is usually unclear from these images what the composition of the particles are; therefore techniques such as EDX (4, 6, 82, 139) and FTIR (82, 139) can be used to investigate chemical speciation. The drawback of these techniques is they cannot give chemical and stoichiometric information simultaneously (140), and the determination of the species present is typically inferred through the detected element ratios (EDX) or the chemical bonds detected (FTIR). To unambiguously determine speciation x-ray spectroscopy (XPS) can be used. This technique can map the elemental distribution across a region, and produce spectra at given points allowing for the chemical structure and valence state of a given element to be distinguished (140). All this can be done without the intrinsic problems related to destructive sample preparation, such as dehydration for vacuum or coating/staining required for techniques such as TEM, as the fluorescence emitted is characteristic to a specific element, meaning the observed sample's state is similar to that *in vivo*.

3.3.1. Synchrotron X-Ray Spectroscopy

Synchrotron x-ray spectroscopy uses synchrotron radiation as a source for the x-rays. It is a preferred method for use on samples which require a high level of sensitivity due to the high photon flux and linearly polarised nature (141) of the beam (of x-rays); rather than a corresponding bench-top machine using x-ray tubes. However, synchrotron sources are only found at dedicated facilities, for example, the Diamond Light Source (Oxford, UK) or the European Synchrotron Radiation Facility (Grenoble, France).

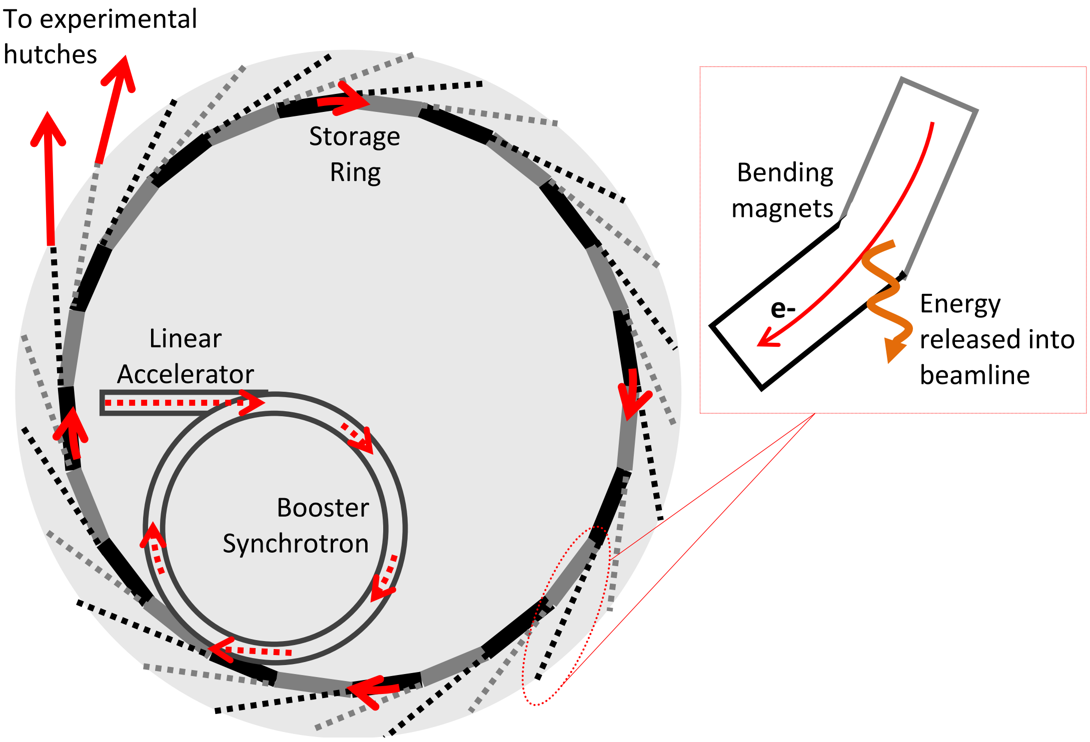

Figure 3.5: Schematic of a standard synchrotron set-up. Electrons accelerated and booster synchrotron where they gain speed before entering the larger storage ring. In the storage ring, electrons are bent by magnets, releasing x-rays used to interrogate samples.

Synchrotrons are also known as cyclic particle accelerators. Typically a synchrotron is made up of an electron gun (where electrons are generated), and series of accelerators (figure 3.5). The accelerators consist of a linear accelerator which injects the electrons into the booster synchrotron (to gain speed), and finally the storage ring (large 'circle' made up of small straight sections). Bending magnets (located at the junction of each straight section) are used to bend the electrons around the storage beam. Each time the electron passes through a magnet it releases energy as photons, which is guided into the experimental workstations, and typically referred to as a beamline. This is where the schematics of beamlines vary, depending on the experiments designed to take place there. However, typically all beamlines will contain an optics hutch (where

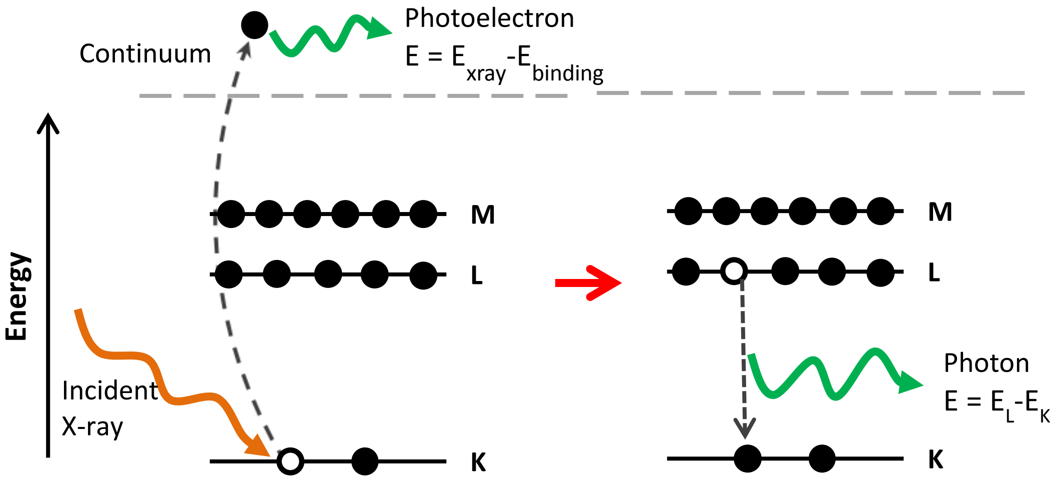

Figure 3.6: Fundamental process behind x-ray spectroscopy. K, L and M represent the first few electron orbitals/shells. Incident x-rays excite an electron in a lower shell leaving a hole later filled by a higher state electron. This process emitts a characteristic photon with energy equal to the energy gap.

the beam is focused) before being passed to the experimental hutch (where measurements take place).

3.3.1.1 X-Ray Fluorescence Phenomenon

As seen in figure 3.6, an x-ray incident upon an atom can displace a core electron, given the energy of the x-ray is greater than its binding energy. When displacement occurs, the incident x-ray is absorbed and any remainder energy (in excess of the binding energy) is passed to the ejected photoelectron. This process causes the atom to become unstable, therefore an electron from a higher orbital falls into the hole to take its place. When this occurs, a photon is released with energy equal to the difference between the two orbitals, and as the electronic orbital energies for all elements are known, this energy is characteristic of the element. There is a second effect (auger effect), whereby an electron may be released (from an outer orbital) in place of a photon. However as this is typically a low energy (<2keV) mechanism it will not be discussed here, as Co and Cr detection would require higher energy x-rays (142).

3.3.1.2 X-Ray Fluorescence Mapping

Detecting the photons emitted from the atom, after excitation by x-rays (described above), allows the elements present within the cross-section of the 'beam' to be determined. Scanning across the surface of a sample with an x-ray beam produces a map of the elements present. This is essentially x-ray fluorescence mapping (XRF) (143). Since samples contain more than one element, a typical method of XRF mapping is to set the incident x-ray energy to just above the heaviest element of interest (EOI), which ensures any variation in ionisation or speciation of the EOI still detected. In addition, all lighter elements to the EOI should also be excited and detected, though typically the contrast will not be as great. Multiple channels are then output (one for each element measured) that can be overlaid to produce a final image showing the elemental spatial distribution in a sample. The intensity of the map at each point (pixel) is proportional to the elemental concentration at that point. If standards are prepared for known concentrations then these can be correlated with the intensity and a calibration curve be made.

3.3.1.3 X-Ray Absorption Near-Edge Spectroscopy

X-ray absorption spectroscopy (XAS) is based on the same underlying principal as XRF. Typically XAS measurements can be performed in transmission or fluorescence geometries (144). Irrespectively, the absorption coefficient is interrogated by measuring a single point through a range of selected energies

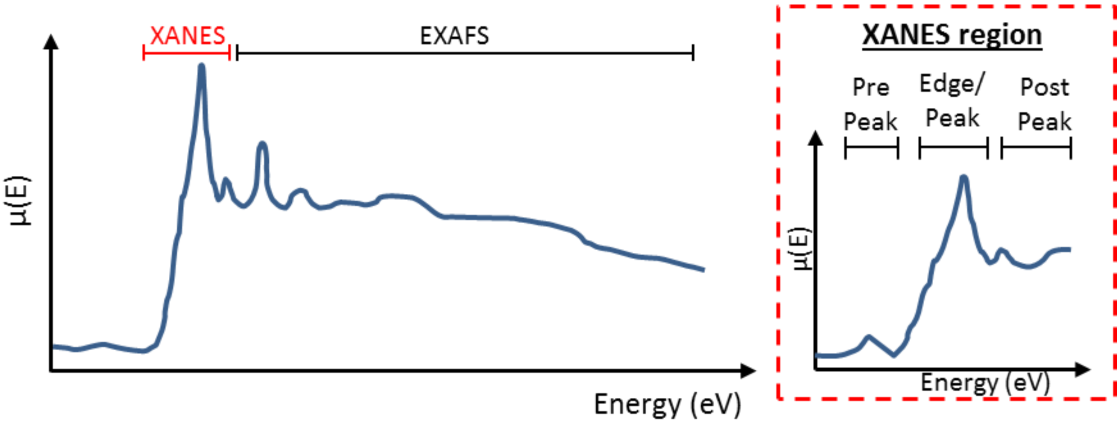

Figure 3.7: Typical x-ray absorption spectra depicting the x-ray absorption near edge spectroscopy (XANES) region and the extended x-ray absorption fine structure (EXAFS) regions of the spectrum. A detailed view of the XANES region highlights the pre-peak, K-edge/peak and the post-peak regions.

using monochromatic x-rays above and below the binding energy. By plotting the intensity against energy, the resulting spectrum reveals information on the chemical speciation (regarding its co-ordination state) of a single (user defined) element at that point.

Figure 3.7 depicts a typical XAS spectrum. Generally, this is split into two regions, the x-ray absorption near edge spectroscopy (XANES) region and the extended x-ray absorption fine structure (EXAFS) region.

XANES provides information regarding the symmetry and electronic structure of the observed element (145). There are typically three regions within the XANES spectra that are analysed (figure 3.7); the pre-peak, peak or edge, and the post-peak regions (141-143). The pre-peak exists at energies below the excitation energy for a given element and contains features resulting from electron transitions to higher unfilled orbitals. The peak, or edge, occurs at the absorption threshold for a given element, representing the transition or a core electron to the lowest unoccupied orbital. This event has a high probability of occurring, hence the steep absorption gradient. The post-peak region typically results from ejected photoelectrons (figure 3.6) experiencing multiple scattering events in higher orbitals. As such this region is harder to fit in analysis.

Features in the EXAFS region, like in the XANES post-peak region, are as a result of ejected photoelectrons. However, these photoelectrons have a higher kinetic energy and as such single scattering events with the nearest neighbours dominate (142, 143). Analysis of these peaks/features, provides information regarding the numbers and types of ligands/neighbouring atoms, as well as the distances between these ligands/neighbours and the absorbing atom (145).

3.3.2. Studies of CoCr in tissue

Synchrotron XRF and XAS techniques are well suited to the analysis of low concentrations of metallic debris within tissues, giving insight into the local chemistry. To date studies focusing on identification of the metallic species of wear debris, using such techniques, aren't as numerous as the more destructive characterisation methods, i.e. SEM/TEM with EDX (4, 6, 64).

Typically many studies have focused on the analysis of Cr, driven by the need to understand the Cr valency present. As mentioned previously (section 2.7.2), Cr(III) is thought to play a role in the metabolism of glucose, while Cr(VI) is classed as a group 1 carcinogen. The distinction between Cr(III) and Cr(VI) in a XANES spectrum is obvious - the pre-peak for Cr(VI) has a much higher amplitude than Cr(III) (146) - however by all accounts Cr(VI) has yet to be detected in patient samples or *in vitro* studies (76, 81, 92, 140, 147, 148).

The literature documents a variety of Cr(III) species interpreted from XANES spectra in periprosthetic tissues from failing hip implants. From XANES measurements, Ektessabi et al. (75) observed an edge/peak shift which implied partial oxidation of Cr. However, the quality of the data suffered due a low beam resolution - 10μm. Beam resolution in x-ray spectroscopy refers to the width of the beam (which also dictates pixel size). A wider beam is less able to resolve two closely neighbouring points as the beam is likely to span them both in one measurement. In addition, the study utilised only a single point XANES measurement and stated that it wasn't similar to metal Cr or Cr oxide (Cr_2O_3); from this a conclusion was made as to the speciation of Cr within the tissue. A single point XANES measurement provides no spatial information on Cr species and as such is not adequate to conclude as to the general speciation within a tissue.

Hart et al. (76, 77) improved upon this study by reducing the beam width, 4μm, and performing a variety of static XANES measurements at the Co and Cr energies. The most abundant Cr species observed was interpreted as a hydrated chromium phosphate complex, while Co analysis reported a combination of metallic Co with some Co(II), most likely in the form of an organic complex. However, given implant derived debris is typically characterised as containing a high proportion of nanometre sized particles (7, 58, 59, 64, 65, 67), it is reasonable to suggest that a 4μm beam may span multiple particles/aggregates. This means only the most dominant species present within the beam width will be reported, and any subtle changes in speciation may be lost. This limitation also applies to the use of single point XANES measurements. Multiple single points over an area of tissue will indicate the global average of species across the tissue, but any small-scale local changes are not measured.

Goode et al. (92) further improved upon the beam resolution by using a nano-sized beam (25nm) on a scanning transmission X-ray microscope (STXM) to perform XAS on particles internalised by macrophages within tissues. This overcomes the limitations stated previously regarding the observation of small-scale local changes. It was noted that there appeared two phases to the debris, (i) Cr(III) as a hydroxide or oxyhydroxide with some oxidised Co(II) and (ii) oxidised Cr(III) and metallic CoCr. A main outcome of the paper was the near absence of any Co from the majority of the internalised particles suggested rapid corrosion resulting in a significant localised release of Co(II) (92). However, despite using a submicron beam on a scanning microscope, the paper does not highlight the importance of a mapping approach over the more frequently used single point measurements. What is lacking is the validation that this approach is the only logical choice to evaluating spatial variation of the local chemistry of implant derived debris within tissues. It was this that motivated the third research question addressed in chapter 6 – does the scale of the approach impact the spatial variation of the local chemistry observed within tissues?

Chapter 4

How Do Cobalt Ions Affect Collagen Formation?

Contributions: *All work in this chapter was designed and written-up by the author Hayley Floyd (H.F.). Experimental research was performed solely by H.F. for all parts except the AlamarBlue assay, Raman spectroscopy and differential scanning calorimetry performed by Emma McCarthy (Grover group, Physical Sciences for Health, University of Birmingham).*

4.1. Introduction

Cobalt-chromium-molybdenum (CoCrMo) alloys are commonly used within the medical industry for metal implants due to their improved resistance to frictional and corrosion related wear (38). For example metal-on-metal (MoM) hip implants have been found to have lower rates of wear than comparative metal-on-polyethylene (MoP) implants, and generate smaller (submicron) particles (4, 42). MoM implants have been found to be 1.5 times more likely to require revision within 2yrs than MoP implants (149). The need for revision is typically discovered due to patients experiencing pain, even with well positioned implants. This suggests that an adverse biological reaction to implant derived debris to be a more likely cause than simply a biomechanical failure (150).

MoM implant derived debris is used in this thesis to describe the combination of particulate and ionic debris. Particulate debris is typically generated through mechanically abrasive mechanisms at the articulating surface (5, 57), or through the precipitation of metal ions (93). The release of metal ions is typically due to corrosion processes, as described in section 2.4. A passive oxide layer is present on the surface of the bulk implant which limits corrosion processes (53); however the repetitive mechanical movement of load bearing hip implants can disrupt this leading to corrosion of the surface and the release of free metal ions (40, 55).

Considering literature shows that cobalt is more soluble than chromium (151); precipitation of Co(II) in culture media could not be observed (85, 93); and the near absence of Co in particles internalised by macrophages suggested a significant localised release of Co(II) (92); it is reasonable to conclude that Co is more likely than Cr to remain in ionic form, interacting with the extracellular matrix (ECM).

As stated previously (section 2.7), current literature evaluating the effect implant derived debris has on the initiation of inflammatory responses typically interrogate two-dimensional cell cultures (10, 103-105, 107, 113, 121). Previous studies have shown how Co can cause cellular death by crossing the cytoplasmic membrane and interacting with nuclear proteins and DNA (152); cause apoptosis and necrosis in macrophages (153); and increase pro-inflammatory cytokines (103, 104). While these studies are crucial to understanding the pathogenesis of osteolysis, they do not consider the extracellular environment. It is well known that cellular interactions are driven by small chemical and/or physical changes in the three-dimensional ECM (154-156). As such, this may influence the cellular (157) and mechanical (118) functions associated with soft tissue and bone.

The ECM provides the physical and chemical cues that direct cell function and fate, and primarily consists of collagen type I (115). The collagen matrix formation is a hierarchical process requiring multiple stages prior to fibre formation (115). Considering Co and Cr ions produced through the tribocorrosion of MoM implants are relatively small - Co atom = 125pm, Co(II) = 70pm, Cr atom = 129pm, Cr(III) = 62pm (158, 159) – they have the potential to interact with collagen at early stages in the development of the fibres. Any interaction may result in modifications to the hierarchal conformation and thus impact the structural and mechanical properties of the matrix. This has been observed in literature originating from the leather industry, with respect to Cr(III) ions. It was demonstrated that Cr(III) dehydrates collagen by displacing bound water and forming nanometre-sized clusters between the fibrils resulting in inter-fibrillar crosslinking (122, 123). However, as Co(II) has never been used to tan leather, its effect on collagen has never been investigated. This chapter investigates how the presence of Co(II) ions can affect structural and mechanical properties of collagen matrix formation and how this subsequently effects the cellular-matrix interactions.

From the literature, the concentrations of Co ions measured from bodily fluids and tissues vary substantially. Examples of concentrations measured are as follows: average of 7.5µg/L in serum and 3.4µg/L in blood (83), 745µg/L in synovial fluid (87), up to 193mg/L in tissue (granuloma) (79). However, ion levels detected in peripheral fluids have the potential to misrepresent the complexity of the heterogeneity in implant ion concentrations within the immediate implant environment. As such the upper concentrations of Co(II) used during the subsequent investigations was derived from the Co levels found in tissue (79).

Throughout this thesis, notation for Co(II) concentration is reported in ppm [1ppm = 1mg/L].

This chapter contains a series of experiments performed to observe the effect Co(II) ions had on the structural and mechanical properties of the collagen matrix at different length scales, i.e. the conformation of peptides, D-spacing, fibre distribution and mechanical properties. Any changes to the structure of the ECM will impact upon cellular functions such as attachment and proliferation, thereby affecting tissue function. The aims of this chapter are to (i) determine the effect Co ions have on the structure of collagen gels and the subsequent cell response to such gels; (ii) suggest potential binding sites for any Co-collagen interactions; and (iii) highlight the importance of studying not only the cellular response to materials, but the effect on the ECM and how this can impact our understanding of the long-term biocompatibility of materials.

4.2. Methodology

4.2.1. Collagen Preparation (CoCol gels)

Cultrex® Rat Collagen Type I, bought from Trevigen® (AMS Biotechnology Europe Marketplace, UK) at 5mg/mL, was diluted to a working concentration of 3mg/mL in sterile phosphate-buffered saline (PBS) stock (NaCl 0.137M, KCl 0.003M, Na_2HPO_4 0.008M, KH_2PO_4 0.0015M). This stock was created by dissolving two Oxoid™ PBS tablets (Thermo Fisher Scientific, UK) in 200 mL of distilled water.

Co(II) stock was made to a concentration of 1000ppm by adding cobalt (II) chloride hydrate (Sigma-Aldrich, UK) to double distilled water. Unsupplemented dulbecco's modified eagle medium (DMEM) (Sigma-Aldrich, UK) was then pre-dosed with Co(II) at a range of concentrations (0ppm, 30ppm, 65ppm, 135ppm, 200ppm) and buffered back to pH 7.6 with 1M sodium hydroxide (NaOH) to maintain pH consistency.

Collagen (3mg/mL working stock) was further diluted with Co dosed-DMEM, to a final concentration of 1mg/mL and NaOH was added until a light pink colour change occurred at pH 8. The collagen solutions were then incubated for 3 hours at $37^{o}C$ to ensure full gelation. All solutions were kept on ice around $4^{o}C$ prior to use. These Co-dosed collagen gels are henceforth referred to as CoCol gels.

4.2.2. Circular Dichroism (CD)

The molecular conformation of collagen after the addition of Co(II) was measured using a circular dichrometer (CD) (Jasco J-715 spectropolarimeter). CoCol gels were prepared and added to Type 20/C Spectrosil® Far UV Quartz cuvettes (Starnacells Inc.), all of which were matched with a path length of 0.5mm. Once in cuvettes, the collagen was incubated at 37°C for 3hrs to ensure full gelation. After gelation, samples were placed in circular dichrometer under nitrogen. Spectra were recorded between 185-400nm at 200nm/min over 5 repeats, and the average was taken.

Due to the long incubation times, to ensure full formation of the collagen, 4 cuvettes were prepared simultaneously, 1 control and 3 containing Co. The control was present for each round of samples to provide a measure of continuity.

4.2.3. Reflection Confocal Microscopy (RCM)

Confocal reflection microscopy is useful to observe the large-scale fibrillar network of collagen gels without the need for sample processing, reducing the risk of sample deformation due to fluorescent-labelling or drying artefacts. A z-stack of a given volume can be observed to provide 3D information. However, the resolution in z is low and requires deconvolution, which is not possible in reflection mode at length scales above nm-range. As such, summation of the 3D-stack is the best way to present reflection images of the collagen network.

CoCol gels were prepared in a 35mm imaging dish with a N#1.5 coverslip base (MatTek Corp., Massachusetts USA), and left for 3hrs at 37°C for the fibrils to fully form. Immediately after, fibrils were imaged on an inverted Olympus FX1000 microscope using x60 water immersion lens with a 488nm laser in reflection mode. 100 images were taken in the z (vertical) direction to produce a 3D-stack of a fixed volume. Using Fiji (Java-based processing package based on ImageJ) each image in the 3D-stack was first normalised based on intensity, then projected onto a 2D plane in the z-direction using ‘Z Projection’ in the standard version.

4.2.4. Atomic Force Microscopy (AFM)

CoCol gels were prepared and a thin layer of each sample was swabbed onto a clean glass slide. This was left in a sealed container to prevent loss of water and allow collagen fibrils to fully form at 37^{o}C for 3hrs. The layer of collagen was then air dried and further washed with sterile water to remove salt crystals from the surface. Atomic force microscope (AFM) images were acquired using a NanoWizard® 4 NanoScience Atomic Force Microscope (JPK Instruments, Germany) in intermittent contact mode using PPP-NCL cantilever tips (Nanosensors, Windsor Scientific).

AFM images were analysed using the JPK Data Processing software to enhance the contrast of the images. The D-banding results in repetitive peaks in the height profile along the length of the fibrils. The width of fibril D-banding was measured as the full-width at half-maximum from these height profiles. Band spacing values were taken from a minimum of 5 positions along a given fibril, on a minimum of 10 fibrils and the average taken. An independent-samples t-test was performed on SPSS statistics software (version 24.0, IBM Corp.) to determine whether a change in D-banding was significant between the samples of CoCol gel. Significance is observed for $p<0.05$ ($p<0.001$ being very significant), while $p>0.05$ is not significant.

4.2.5. Turbidity Curves

Kinetic analysis of the collagen fibril formation was studied by measuring the turbidity curves using a UV-VIS spectrophotometer (Cecil Instruments, UK). CoCol gels were prepared and immediately added to a disposable cuvette (1cm) and placed in the spectrophotometer. Temperature was temperature maintained at 37^{o}C, with absorbance at 620nm. The kinetics study began immediately (t= 0min) and a turbidity-time profile was produced after measuring absorption every 30 seconds for 2 hours. Each concentration of Co(II) in collagen was interrogated three times and an average taken.

4.2.6. Rheometry

CoCol gels were prepared in 35mm dishes (ThermoFisher Scientific) with a gel height of 1mm, and kept in an incubator at 37^{o}C until 5mins prior to measurement. Rheological measurements were performed with an AR-G2 rheometer (TA Instruments, USA). A sandblasted 20mm stainless steel plate (to minimise wall slip) was used in parallel plate geometry with a gap of 1mm. The limit of the linear viscoelastic region was determined through strain sweeps, performed at a frequency of 1Hz. The lowest value was found to be at 0.01 strain. G' and G'' graphs were therefore obtained through frequency sweeps, performed at a strain of 0.01, over a frequency range of 0.01-10Hz.

4.2.7. Cell Culture

All cell culture procedures were conducted using standard aseptic technique within a laminar hood (BSB 3-S, Gelaire ICN Biomedicals, UK) sterilised with

Virkon and 70% ethanol. Equipment was disinfected with 70% ethanol and cell culture media warmed to 37^{o}C in a water bath prior to use

Pre-osteoblast MC3T3-E1 subclone 4 (MC3T3) cells from mice were obtained from LGC (Middlesex, UK), their behaviour is similar to primary calvarial osteoblasts. Human Dermal Fibroblast (HDF) cells were obtained from LGC (Middlesex, UK).

Cell numbers were expanded over several weeks and stored in liquid nitrogen (N_2) at 10^6 cells/mL. When required a vial was rapidly defrosted in a water bath at 37^{o}C and added to fresh media supplemented with: 10% foetal bovine serum (FBS); 2.5% HEPES; 1% penicillin-streptomycin (Pen/Strep); and 2.5% L-glutamine (L-Glut). Minimum Essential Medium Eagle Alpha Modified (αMEM) (Sigma-Aldrich, UK) was used for MC3T3 cells and Dulbecco's Modified Eagle's Medium (DMEM) (Sigma-Aldrich, UK) was used for HDF cells.

Cell-media solutions were centrifuged at 1000rpm for 3min and the supernatant aspirated, discarded and replaced with fresh supplemented media. MC3T3/HDFs were subsequently re-suspended, seeded in 75ml flasks (ThermoFisher Scientific) and incubated (37^{o}C, 5% CO_2, 95% air) (Sanyo Electric Co. LTD, Japan).

4.2.8. Cell Splitting & Counting

Once cells were at ~70% confluency the media was removed and the cells washed with warm sterile phosphate buffered saline (PBS). Either TrypLE™ Express (for MC3T3s) or TrypLE™ Select (for HDFs) (ThermoFisher Scientific) was then added and flasks returned to the incubator (37^{o}C, 5% CO_2, 95% air)

(Sanyo Electric Co. LTD, Japan) until at least 90% of cells de-attached. Supplemented culture media was added to neutralise the TrypLE™ /TrypLE™ Express. The cell solution was then centrifuged at 1000rpm for 3min and re-suspended (as above) in fresh supplemented culture media (s-αMEM or s-DMEM). If the cells were to be used, cell counting was performed at this point using an automated cell counter (Countess™, ThermoFisher Scientific), otherwise cells were divided into multiple flasks and incubated (37°C, 5% CO_2, 95% air) (Sanyo Electric Co. LTD, Japan) for further proliferation.

4.2.9. Incubation of Cells and Collagen

Sterility of CoCol gels was maintained by ensuring all reagents were kept sterile, either through 0.22μm filtration or autoclaving were appropriate, and using standard aseptic technique within a laminar hood at all times. Equipment was sterilised using 70% ethanol and one bottle of collagen (shipped sterile) was reserved for cellular experiments.

Cells were incubated either on or within collagen. For cells on top of collagen, the standard procedure of cell splitting and counting was used, before being seeded on the surface of fully gelled collagen in cell culture media and returned to the incubator (37°C, 5% CO_2, 95% air) (Sanyo Electric Co. LTD, Japan). For cells within collagen, cells were added to DMEM during the procedure of mixing the reagents to make collagen gel. The DMEM needed to make a collagen sample was split into 2 volumes. To one volume, the Co(II) was added to the required concentration and buffered to pH 7.6, and to the other, cells were added at a concentration of 5000 cells/mL of final collagen. These 2 volumes were then combined with collagen and NaOH (as previously described) and deposited in 12-well plates (ThermoFisher Scientific). After 3 hours of gelation at 37^{o}C, 2mL of fresh supplemented cell culture media was added to ensure cell viability and to prevent the CoCol gel drying out. Samples were then placed back in the incubator (37^{o}C, 5% CO_2, 95% air).

4.2.10. ICP-OES

Inductively coupled plasma optical emission spectrometry (ICP-OES) is a spectroscopic technique used to determine the amount of a given element in a sample. Widely used to determine concentrations of trace elements, ICP-OES excites the atoms and ions of a sample using inductively coupled plasma. This results in the emission of radiation at specific wavelengths characteristic of the excited elements. A given wavelength is observed, and the intensity is used to determine concentration from a calibration curve.

Collagen samples containing increasing Co(II) were prepared in 12-well plates to determine the release of Co into the surrounding after 1 and 6 days, with 3 repeats of each concentration at each time point. After preparation and gelation of the CoCol gels, 1.5mL sterile PBS was added to each well and incubated at 37^{o}C. PBS was used over culture media as it is a “cleaner” solution for the ICP-OES i.e. less complex due to numerous salts.

At day 1 and 6 the PBS supernatant was removed and frozen at -20^{o}C for later analysis. These samples were later thawed, diluted with 50% PBS to ensure saturation was not reached, and acidified to 2% w/v nitric acid (HNO_3). Samples were run through the ICP-OES (Optima 8000, PerkinElmer) using a flow rate of

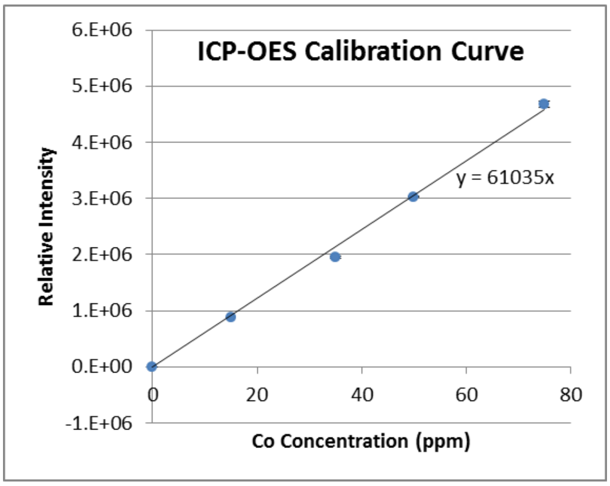

Figure 4.1: Calibration curve for inductively coupled plasma optical emission spectrometry (ICP-OES) between the relative intensity of counts at 228.616nm (characteristic peak of Co) and Co concentration. This was determined using Co-standards by running known concentrations on the ICP-OES.

1mL/min and counts at 228.616nm, a characteristic peak of cobalt, was recorded and averaged. A calibration curve was created using an in-house cobalt standard and measured counts were converted to concentrations (figure 4.1).

An independent-samples t-test was performed on the results to determine if the release of Co(II)from the CoCol gels, at a given Co(II)concentration, between days 1 and 6 was significant. This would indicate whether the any release of Co(II)was long term or not. Significance is observed for $p<0.05$ ($p<0.001$ being very significant), while $p>0.05$ is not significant.

4.2.11. MTT Assay

An MTT (3-(4,5-Dimethylthiazol-2-yl)-2,5-diphenyltetrazolium bromide) assay is a colorimetric assay. It is used to assess the cell metabolic activity which can be used to infer viable cell number in proliferation and cytotoxicity studies. In living cells, yellow tetrazole is reduced to purple formazan by mitochondrial enzymes. An increase in purple colouring corresponds to an increase in enzymes and thus metabolic activity. Under most standard conditions the number of enzymes is proportional to the number of viable cells. As such the MTT assay is widely used as a test for the number of viable cells compared to a control.

MC3T3 cells were seeded at a concentration of 7,500 cells/well in a 48-well plate and left in an incubator to allow attachment and proliferation using supplemented αMEM for 24hrs. The media was then aspirated and replaced with C-o-dosed culture media. Co-dosed culture media was prepared by adding Co(II) solution to supplemented αMEM at concentration of 200ppm Co(II) and buffering using 1M NaOH to pH 7.6. This working stock was diluted to a range of Co(II) concentrations (0, 5, 10, 15, 20, 25, 30, 40, 50, 100, 150 and 200ppm Co(II)) with supplemented αMEM. Cells were incubated for a further 24hrs in Co-dosed media prior to performing the MTT assay (Merck, USA).

A stock solution of sterile-filtered 5mg/ml MTT (Sigma, UK) in PBS was prepared and stored at 4°C in the dark. On day 3, 200μL/well of supplemented αMEM with 0.5mg/mL of MTT was added and incubated for 2hrs at 37°C for the formazan crystals to form. The MTT solution was then removed and 200μL/well of 0.22μm-filtered dimethyl sulfoxide (DMSO) added and the plate left to rock gently for another 2hrs at 20°C to dissolve the formazan crystals. The optical absorbance of the solution was measured at 570nm using a microplate reader (Promega, UK). The result was expressed as a percentage of the control sample.

4.2.12. Collagen Gel Contraction Assay

HDF cells were incubated within the collagen gel to determine the effect Co(II) inclusion has on the contraction of the collagen gel, also known as a collagen gel contraction assay (CGC assay) (160). Observing the contraction of a disk of collagen gel over time provides an insight into the "cell-mediated reorganisation" of the collagen matrix (160), as cells within the collagen gel are capable of compressing the fibrils resulting in a reduction of the gel diameter.

HDF cells were prepared in CoCol gels, as directed in section 4.2.9. A fixed volume of 0.5mL of CoCol gel was used to create a CoCol+HDF gel drops similar in size. This was incubated at 37^{o}C for 3 hrs and then imaged using a Canon DSLR camera to allow the whole gel to be captured in one field of view. 2mL of Co-free supplemented cell culture media was added to prevent the CoCol gel drying out. After 3 days the media was removed and the CoCol+HDFs were imaged and the diameter compared to the day 0 image. Standard deviation from the mean could not be calculated on these samples due to the lack of biological repeats

4.2.13. X-ray fluorescence (XRF)

An XRF scan of a 200ppm CoCol gel was performed using a benchtop Tornado M4 XRF (Bruker, UK). A scan area of 100ms/pixel was acquired with a speed of 30m/s for three cycles, for energies between 0-10keV. Co XRF images were produced using counts from 6.9keV, the characteristic Co-kα line (161). Ten regions of interest were taken over the entirety of the scan area containing both high and low intensity regions. This ensured a complete representation of the sample was observed. Differences in the peak heights at the Co-kα line were measured and the average difference used to give an increase in relative concentration of Co(II) ions.

4.2.14. Cell Staining

4.2.14.1 Live-Dead Staining

Calcein acetoxymethylester (calcein-AM) is a dye which rapidly permeates across the cell membrane. It is initially non-fluorescent, but in live cells, the ester bonds of calcein-AM are cleaved by intracellular esterases converting it to a green fluorescent calcein. This allows it to be used to determine cell viability.

Propidium Iodide (PI) is a nuclear and chromosome dye that cannot permeate the membrane of live or undamaged cells. As such PI, which is red-fluorescent, is frequently used to determine whether a cell is damaged or dead. Both Calcein-AM and PI can be excited at 490nm and therefore viewed simultaneously using an epi-fluorescence microscope. Although a more accurate method of visualisation is to image sequentially to prevent bleed-through effects. In this case, calcein-AM and PI are excited at 488 and 535nm respectively.

A stock solution of calcein-AM (ThermoFisher Scientific) was prepared in dimethyl sulfoxide to a concentration of 50µg/mL. PI (Invitrogen, UK) was diluted in sterile water at a concentration of 100µg/mL. A volume of 5µL of Calcein-AM and 25µL of PI was added, per 2mL of media, and left for 20 minutes in a dark incubator (37^{o}C, 5% CO_2, 95% air).

Stained cells were then imaged through x10 and x20 lenses on an inverted Olympus FX1000 confocal microscope. A lower magnification of x10 or x20 was used to ensure a wider field of view was observed. Excitation was at 488nm and 543nm for calcein-AM and PI respectively. The channels were imaged sequentially to prevent bleed through.

Results were acquired for MC3T3s on CoCol gels and in Co-dosed media for comparison. Imaging was primarily performed on day 2 to ensure the samples did not exceed ~80% confluency (MC3T3s, on standard cell culture plastic, take 2-3 days to reach 80% confluency at seeding concentrations). If a monolayer forms, this makes distinguishing cell boundaries in confocal microscopy more difficult.

4.2.14.2 Actin & DAPI Staining

Actin staining is commonly used to observe the structure of the cytoskeleton within cells. These actin filaments are essential for many functions, such as cellular adhesion, contraction and morphology. In many biological applications, fluorescent actin-staining is preferable. Actin stains typically contain a probe such as phalloidin, which selectively binds to F-actin, and is conjugated to a fluorescent dye. It is a popular method as it can be used in conjunction with other dyes such as DAPI (4',6-diamidino-2-phenylindole) for a better overview of cellular structure. DAPI is used to observe cell nuclei as it is capable of passing through a cell membrane and strongly bind to DNA.

Cells were cultured on/in collagen containing Co(II) using the methods in section 4.2.7. Once ready, culture media was removed, and the collagen-cell sample was gently washed with PBS twice. Cells were fixed with 4% paraformaldehyde (PFA) at room temperature for either 10 minutes for cells on collagen, or 20 minutes for cells within collagen. The collagen-cell sample was then rinsed with PBS twice, and cells were permeabilised using 0.5% triton X-100 (in PBS) for 5 or 10mins (for cells on or in collagen respectively).

Cells were then stained with ActinRed™ 555 (ThermoFisher Scientific) using 2 drops/mL in PBS at room temperature for 15 or 30mins (for cells on or in collagen respectively). The sample was then rinsed with PBS before staining with 1μg/mL of DAPI (ThermoFisher Scientific) in PBS at room temperature for 5 or 10mins (for cells on or in collagen respectively). Imaging was performed using an inverted Olympus FX1000 confocal microscope to image the two channels sequentially using 405nm and 543nm to excite DAPI and ActinRed respectively.

Results were acquired for HDFs both on and in CoCol gels at day 3. These time points were chosen to ensure the samples did not exceed ~80% confluency. On standard cell culture plastic, HDFs (similar to MC3T3s) take around 3 days to reach 80% confluency at seeding concentrations. HDFs were used as their more characteristic elongated cytoskeleton provided good contrast with actin.

<u>Experiments performed by Emma McCarthy</u>

4.2.15. AlamarBlue Assay

The AlamarBlue assay is a viability assay used to measure proliferation in cells. The active component of AlamarBlue (resazurin) is reduced within the cell to a fluorescent compound (resorufin).

MC3T3s were seeded in 12-well plates at a concentration of 2x10^{5}cells/mL on either CoCol gels or directly onto the cell-culture plastic. Cells seeded onto CoCol gels were incubated with supplemented αMEM, while those seeded onto plastic were cultured and incubated in Co-dosed αMEM. At day 3 the culture medium was removed and 300μL of fresh supplemented αMEM with 10% AlamarBlue dye (Thermo Fisher Scientific, UK) was added and incubated (37^{o}C, 5% CO_2, 95% air) for 4hrs. A volume of 100μL of media was then removed from each well and added to the well of a 96-well plate. Absorption was read at 570nm using a microplate reader (Promega, UK).

4.2.16. Raman spectroscopy

Raman spectroscopy measures the wavelength of light that has been inelastically scattered from a molecule. This scattering is dependent on the structure of the molecule, and as such the characteristic “finger-print” of the Raman spectrum enables the chemical structure of substances to be determined.

Two samples, 0ppm and 200ppm CoCol gels, with a volume of 1mL were analysed using an inVia Qontor confocal Raman microscope (Renishaw, UK). To remove any background signal from DMEM, used in the production of CoCol gels, PBS was used in its place. The rest of the CoCol production method remained the same.

Multiple regions throughout the bulk CoCol gels (0ppm and 200ppm) were interrogated. Scans within a spectral range of 100-4500cm^{-1} were acquired using a x60 water immersion lens and a 785nm laser (pinhole at 10% power) with an acquisition time of 30 seconds. The regions interrogated were re-scanned 30 times. Averaging and normalisation was then performed using Microsoft Office 365 Excel (2013). In order to further remove background noise the spectral range of the normalised spectra were reduced to 350-2650cm^{-1} using Prism5 (GraphPad Software, 2007).

Further analysis was performed using principal component analysis (PCA) on MatLab (R2017a). This allowed for the reduction of data dimensionality in generating a set of principal components (PCs) containing the largest variance within the data set. Plotting the first two PCs (containing the 1st and 2nd highest variance) against each other produced a scores plot. Alongside k-means clustering, this determined the presence of clusters within the data. A loadings plot was also produced, as intense peaks within this plot indicated deviations between spectra and suggest which wavelength contributed the most variance (162). This plot was produced by plotting the 1st PC loading vectors against the wavelength.

4.2.17. Differential Scanning Calorimetry

Differential Scanning Calorimetry (DSC), an analytical technique, is used to investigate a samples response to being heated, relative to a reference. For this application it was used to compare the amount of heat required to remove bound water from a collagen matrix containing 200ppm Co(II) compared with a control of 0ppm Co(II). Again, PBS was used in place of DMEM in CoCol gel production to prevent any background signal.

A Mettler Toldeo Differential Scanning Calorimeter (DSC) (Mettler Toledo, Schwerzenbach, Switzerland) was used to analyse the collagen gels (0 and 200ppm Co(II)). The samples were weighed into 46μL aluminium DSC pans (Mettler Toledo), capped with aluminium DSC lids (Mettler Toledo) and sealed with a press (Mettler Toledo). The DSC pans were then heated linearly between 25^{o}C-135^{o}C, at a rate of 5^{o}C min^{-1}, under nitrogen (flow rate 50 ml min^{-1}). Data acquired was calibrated using indium and zinc standards.

4.3. Results

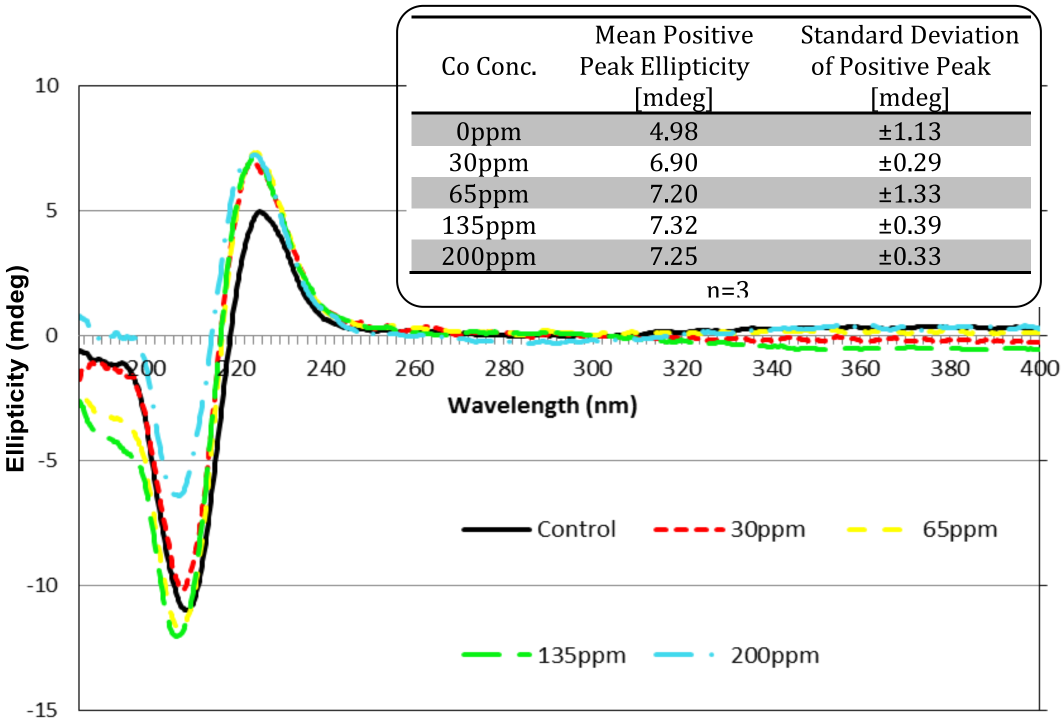

Co Conc.	Mean Positive Peak Ellipticity [mdeg]	Standard Deviation of Positive Peak [mdeg]
0ppm	4.98	±1.13
30ppm	6.90	±0.29
65ppm	7.20	±1.33
135ppm	7.32	±0.39
200ppm	7.25	±0.33

n=3

Figure 4.2: Circular dichroism of CoCol gels with a control of collagen only. Changes in the intensities of the positive and negative peaks potentially indicate the interference of Co(II) with the collagen triple-helix formation. Table insert shows the positive peak ellipticity for the CoCol gels

4.3.1. Determining the effect of Co(II) on collagen triple helix

The effect of Co(II) on the conformation of the collagen molecule was analysed using circular dichroism, as this provided an initial indication as to whether the characteristic structure of the collagen molecule was intact in the presence of Co(II). CD spectra, shown in figure 4.2, suggested the presence of Co(II) does not prevent the formation of the triple-helix in collagen. The characteristic positive and negative peaks were still observed at the same wavelengths seen in the control (no Co(II)). The addition of Co(II) corresponded with an increase in the positive ellipticity at all concentrations with respect to the control, which has been associated with tighter packing of the collagen molecule (129). In addition the negative peak ellipticity showed a decrease at 200ppm Co(II). This depletion is similar to that of denatured collagen (127). This suggested that Co(II) may be modifying the triple-helix in some manner.

4.3.2. Determining the effect of Co(II) on the formation of collagen fibrils

Since CD shows the triple-helix structure appeared to be largely intact, but potentially modified in some manner, it was logical to determine whether there was any change to the self-assembly process of collagen fibrils. The effect of Co(II) on the fibrillogenesis of collagen formation was assessed using a UV-Vis spectrometer. Acquiring turbidity profiles during the formation of collagen fibrils allowed the rate of formation to be evaluated *in situ*.

Figure 4.3 shows the characteristic sigmoidal turbidity profiles for the CoCol gels, suggesting the general process of collagen self-assembly was still occurring. However, the addition of Co(II) corresponded to an increase in the growth phase (time to complete the rise absorbance). This was quantified by finding the gradient of the linear increase in absorbance and extrapolating back to find t_{lag}, and forward to find t_p where the gradient intersects with the horizontal axis and lateral phase respectively. The ratio of the turbidity growth phase, with respect to the control, is shown in figure 4.4a. An increasing growth phase meant the time taken for fibril formation to complete increased, suggesting Co(II) concentration had a detrimental effect on the kinetics of collagen fibril assembly and that even low concentrations of Co(II) ions were interacting with collagen fibrils.

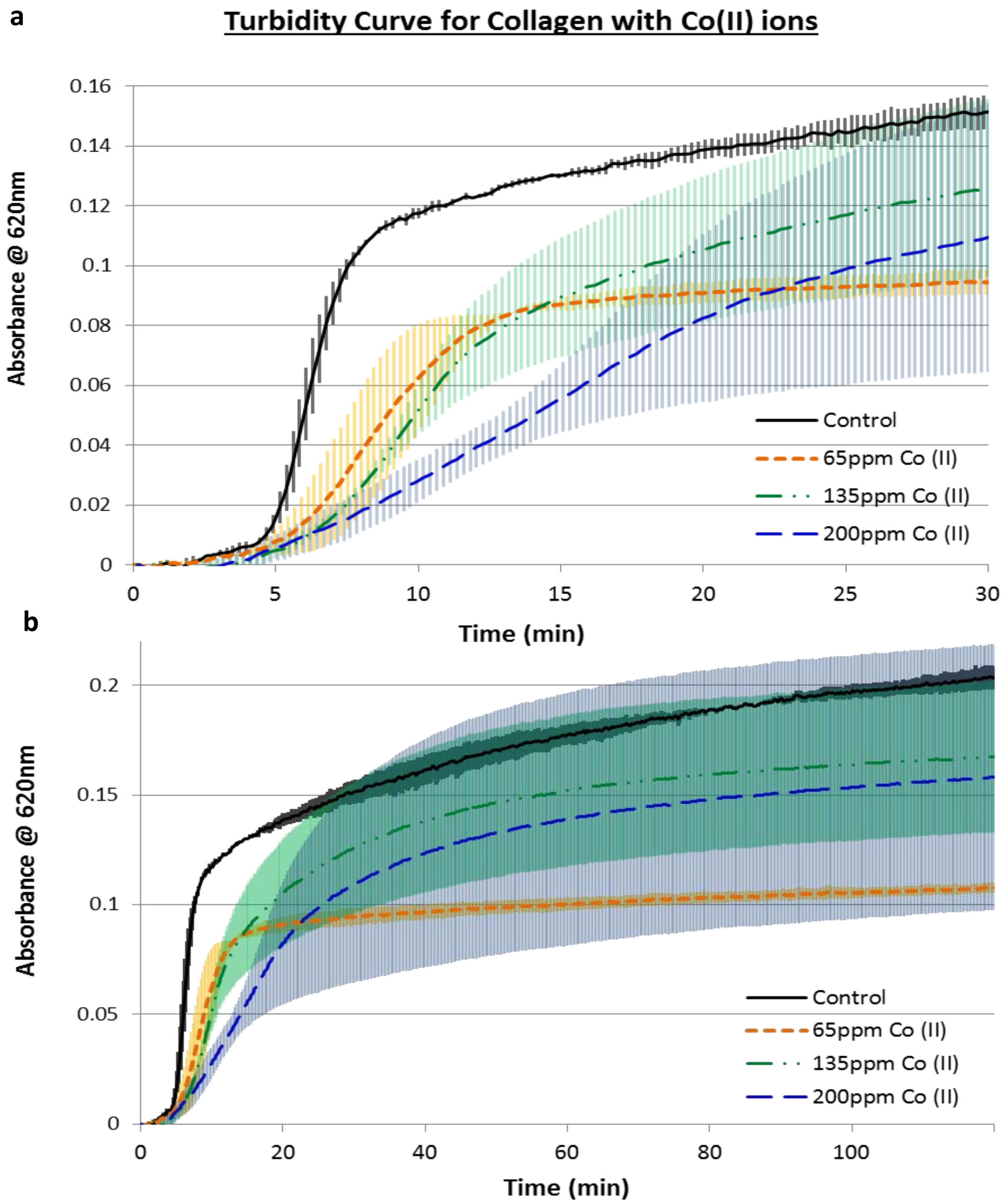

Figure 4.3: Mean turbidity profiles for Co dosed collagen at concentrations of 0, 65, 135 & 200 ppm. [a] Early turbidity profile to show growth phase with [b] complete profile. Error bars show the standard deviation for the repeats within each concentration, n=3.

Considering the implication that Co(II) ions were interacting with the collagen, a leaching study was undertaken to determine the loss of Co from the collagen gel over time, shown in figure 4.4b. The highest Co(II) concentration of CoCol (200ppm) gel released only 8ppm Co into the surrounding media after 6 days, which is small relative to the initial Co(II) concentration. An independent-

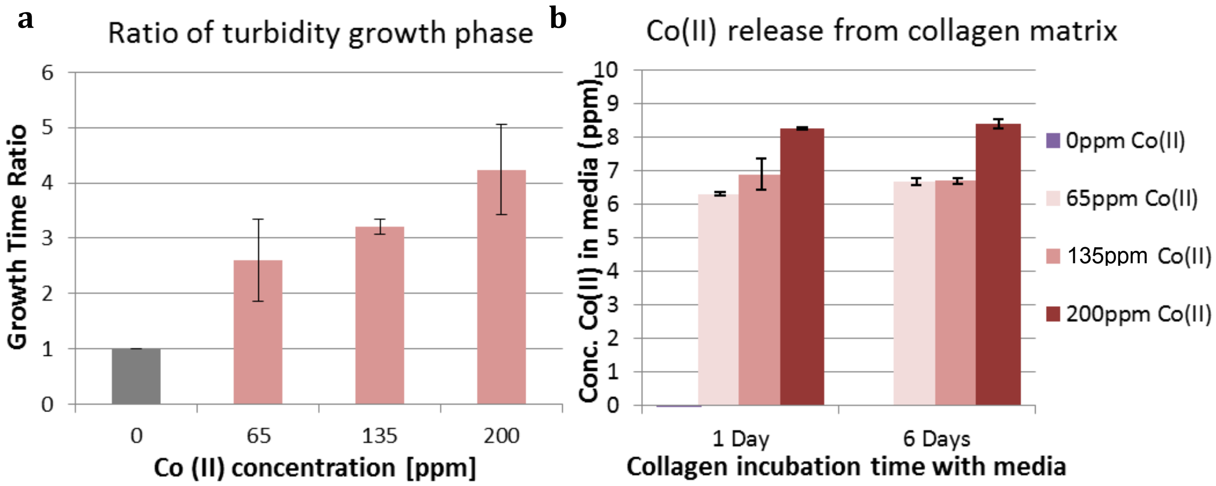

Figure 4.4: [a] Ratio of the growth phase at each Co concentration with respect to the control (0ppm) shows Co increases the time for collagen fibrillogenesis to complete, n=3. [b] Release of Co ions from the collagen matrix after 1 and 6 days for initial concentrations of 0, 65, 135 & 200ppm, n=9. No significanct difference was found between the Co released at day 1 vs. day 6 (p>0.05).

samples t-test was conducted to compare the concentration of Co released between day 1 and day 6. There was no significant difference ($p>0.05$) between the amount of Co released between day 1 and day 6 for any Co(II) concentration of CoCol gels:

- 65ppm Co(II) between day 1 (M=6.307, SD=0.049) and day 6 (M=6.679, SD=0.399), t(4)=-1.603, p=0.184
- 135ppm Co(II) between day 1 (M=6.903, SD=0.457) and day 6 (M=6.706, SD=0.060), t(4)=-0.738, p=0.501
- 200ppm Co(II) between day 1 (M=8.269, SD=0.037) and day 6 (M=8.401, SD=0.095), t(4)=-2.258, p=0.087

This suggested that whatever amount of Co was going to be released occurred early on, with no long-term leaching of Co(II) from the collagen matrix.

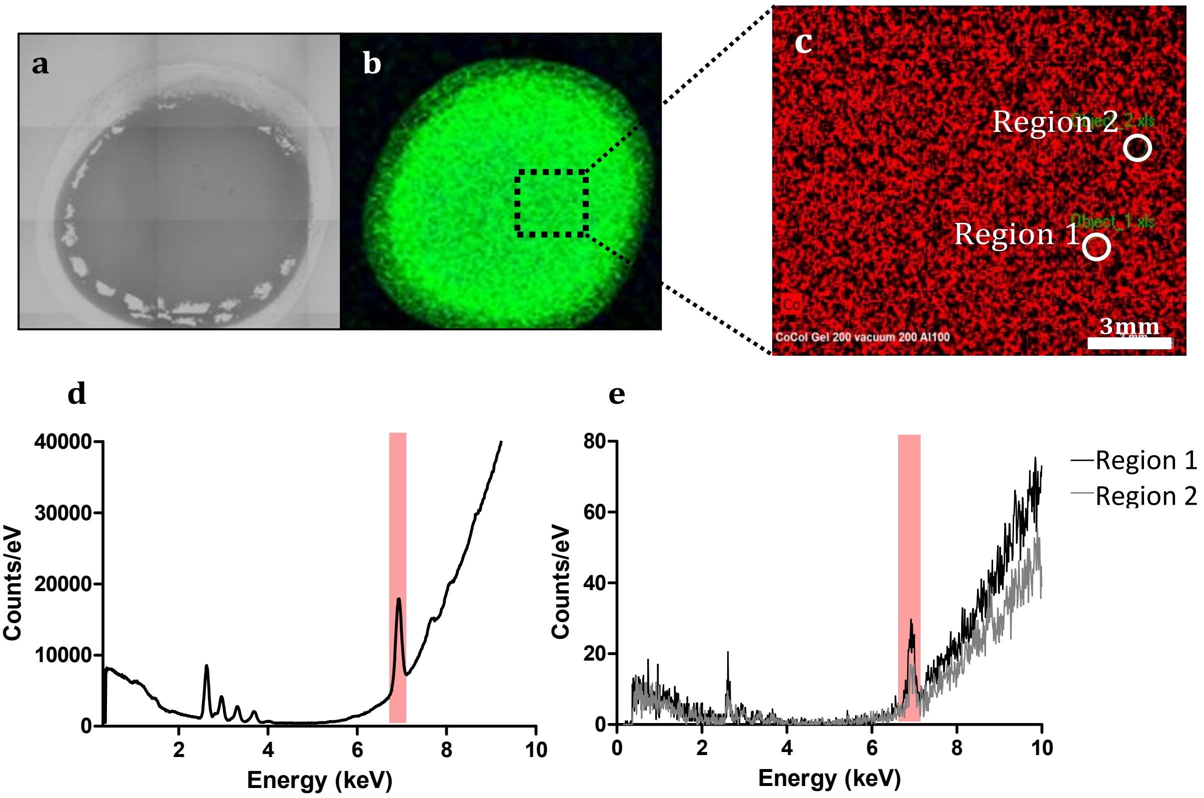

Figure 4.5: Benchtop X-ray fluorescent (XRF) measurements of Co distribution within a CoCol gel containing 200ppm Co(II). [a] Bright field image of CoCol gel. [b] Relative Co intensity map throughout CoCol gel. [c] Zoomed view of Co map showing positions of region 1 & 2 which represent high and low intensities of Co respectively. [d] Averaged spectra of overall gel, Co region highlighted. [e] Spectra of region 1 & 2 used to show an average 3-fold difference in Co fluorescence.

Given Co(II) ions are small (~70pm (158)) in size and there was no significant diffusion into the media over time, the Co(II) ions were unlikely to be sterically trapped within the collagen matrix. This suggested that the Co(II) ions were bound within the collagen matrix itself.

4.3.3. Determining the dispersion of cobalt throughout the bulk matrix

Given the results showing that Co(II) ions were unlikely to be sterically trapped, but rather bound in some manner within the collagen matrix; XRF was performed to produce spatial elemental maps to determine if the Co was homogeneously dispersed throughout the collagen gel. Figure 4.5b-c shows the relative Co intensity mapped throughout the 200ppm CoCol gel. Figure 4.5c highlights two regions demonstrating the presence of regions with high and low intensities of Co. Between these two regions, an average 3-fold increase in the relative intensity of Co fluorescence was seen between the two sites at E=6.9keV, the characteristic Co-kα line (161). This data cannot discern whether heterogeneity in the dispersion of Co observed here is due to heterogeneity in the binding of Co(II) to collagen or in the distribution of the collagen fibrils within the matrix. For that higher magnification imaging modalities must be used and correlated with microscopy of the fibrils.

4.3.4. Determining the effect of Co(II) ions on the collagen matrix

Given the heterogeneity of the dispersion of Co within the collagen matrix, shown in figure 4.5, AFM and RCM was performed to determine the effect Co(II) ions have on the structure of the collagen matrix.

AFM images of CoCol fibrils are shown in figure 4.6a-f. Analysis of these images showed the D-banding of the collagen fibrils not only decreased (figure 4.6g), but was more varied in the presence of Co(II) (figure 4.6h). An independent-samples t-test was conducted to compare the D-banding width for three concentrations of CoCol gels (0ppm, 135ppm & 200ppm). There was a significant difference in the mean D-banding width between 0ppm & 135ppm Co(II) samples ($p<0.001$) and 0ppm & 200ppm Co(II) samples ($p<0.001$), with an average decrease in D-banding of 5.5nm and 5.6nm respectfully. This suggested that Co(II) ions were binding in such a way that influenced the molecular ordering

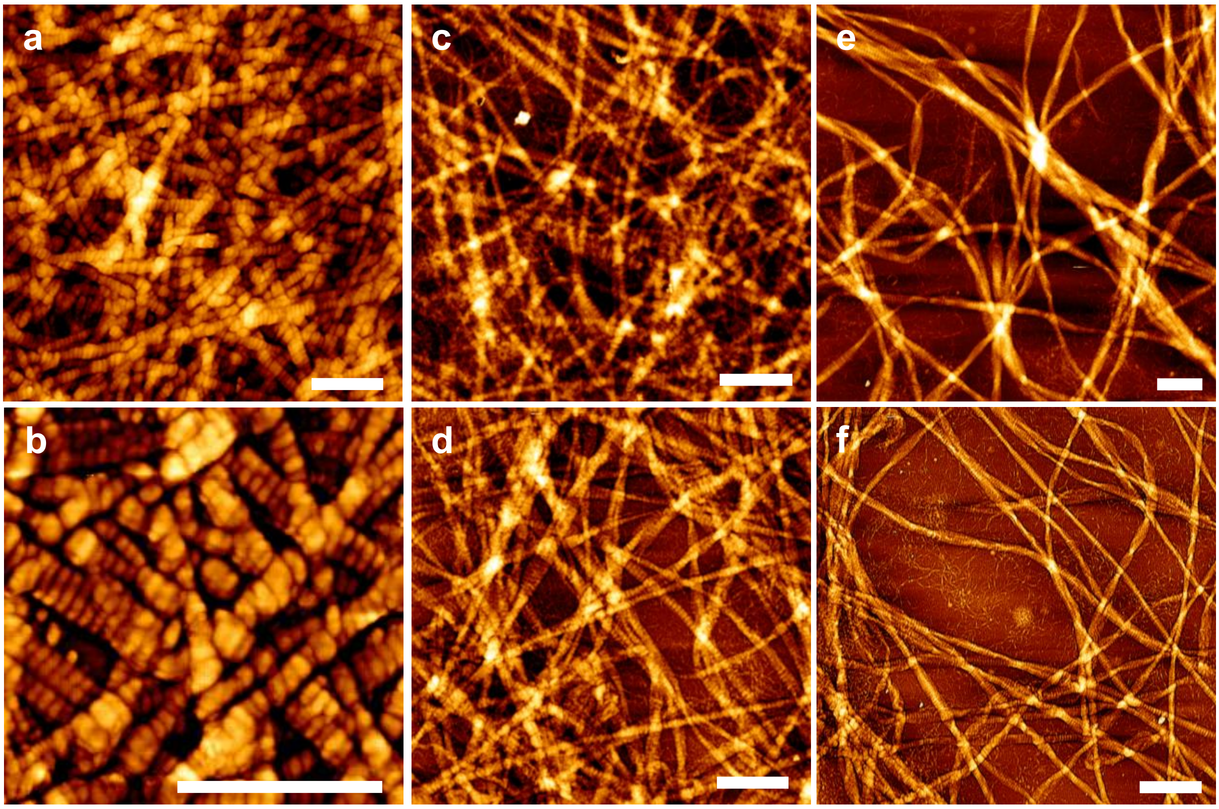

g

	Mean banding width	Standard Deviation
Control	66.3nm	±2.7nm
135ppm	60.8nm	±3.7nm
200ppm	60.7nm	±5.7nm

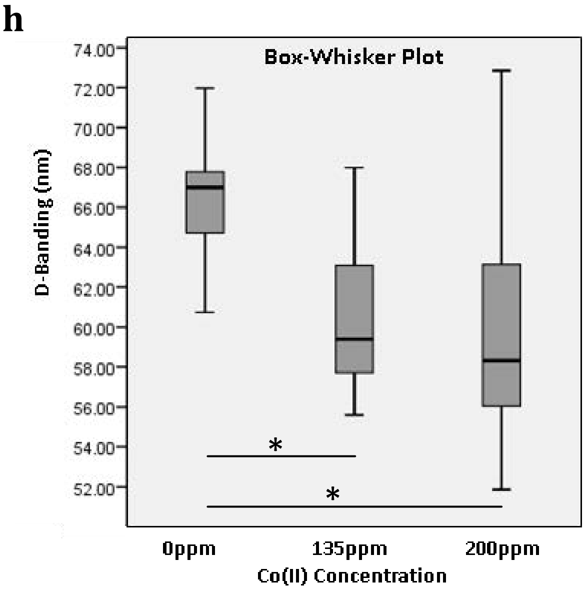

Figure 4.6: AFM images of collagen with [a-b] 0ppm Co(II), [c-d] 135ppm Co(II), [e-f] 200ppm Co(II). Scale bar is 1µm. [g] Table showing the mean D-banding width calculated from the AFM images, error is calculated as the standard deviation with n=68, using multiple fibril across 3 regions of the sample. [h] A box-whisker plot showing the range of D-bandings measured across the CoCol gel samples. 135 & 200ppm were found to be significantly different to the control ($p<0.001$)

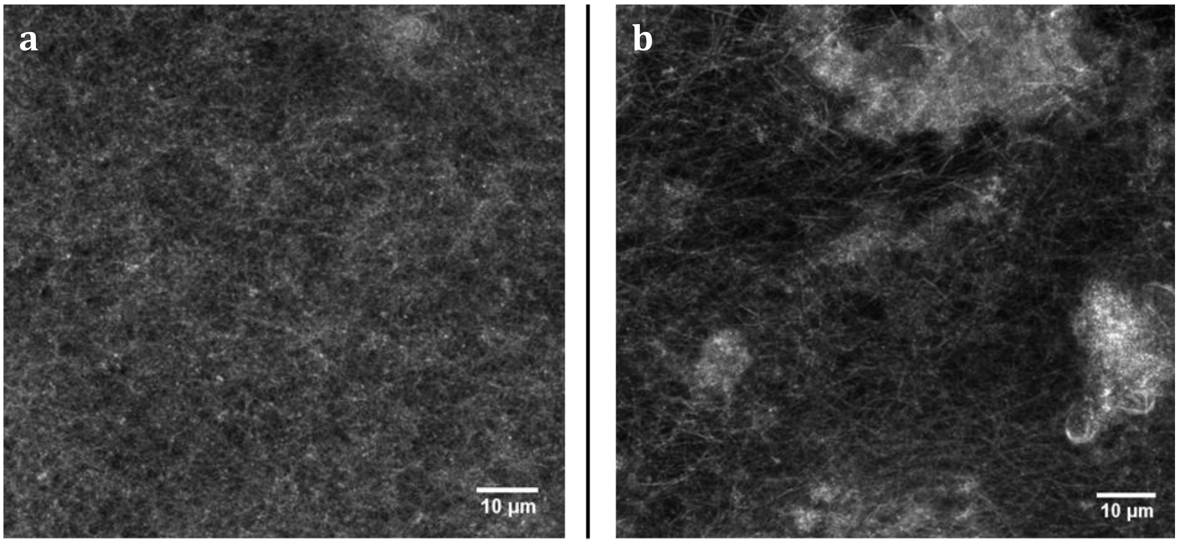

Figure 4.7: Reflection confocal microscopy images of the macro-scale network of collagen. A z-stack has been projected onto 2D for visualisation. [a] 0ppm and [b] 200ppm Co. The presence of Co results in heterogeneity in the collagen matrix.

of the collagen molecules during self-assembly. In addition, these images (figure 4.6a-e) showed more heterogeneity in the distribution of the collagen fibrils with increasing Co. This was most notable between the control and the 200ppm sample as there appears to be more agglomeration between the fibrils with increasing Co.

This observation was confirmed through reflection confocal imaging (figure 4.7), where the control showed a dense homogeneous network of fibrils compared to the heterogeneous network seen for 200ppm Co(II), which contained regions of higher and lower densities of fibrils. This indicated that Co(II) ions not only affect the structure of the collagen fibrils, but also affect the overall structure of the collagen matrix. It also suggested that the heterogeneity observed in the XRF spatial mapping of Co(II) is likely to be due to the distribution of the fibrils within the matrix.

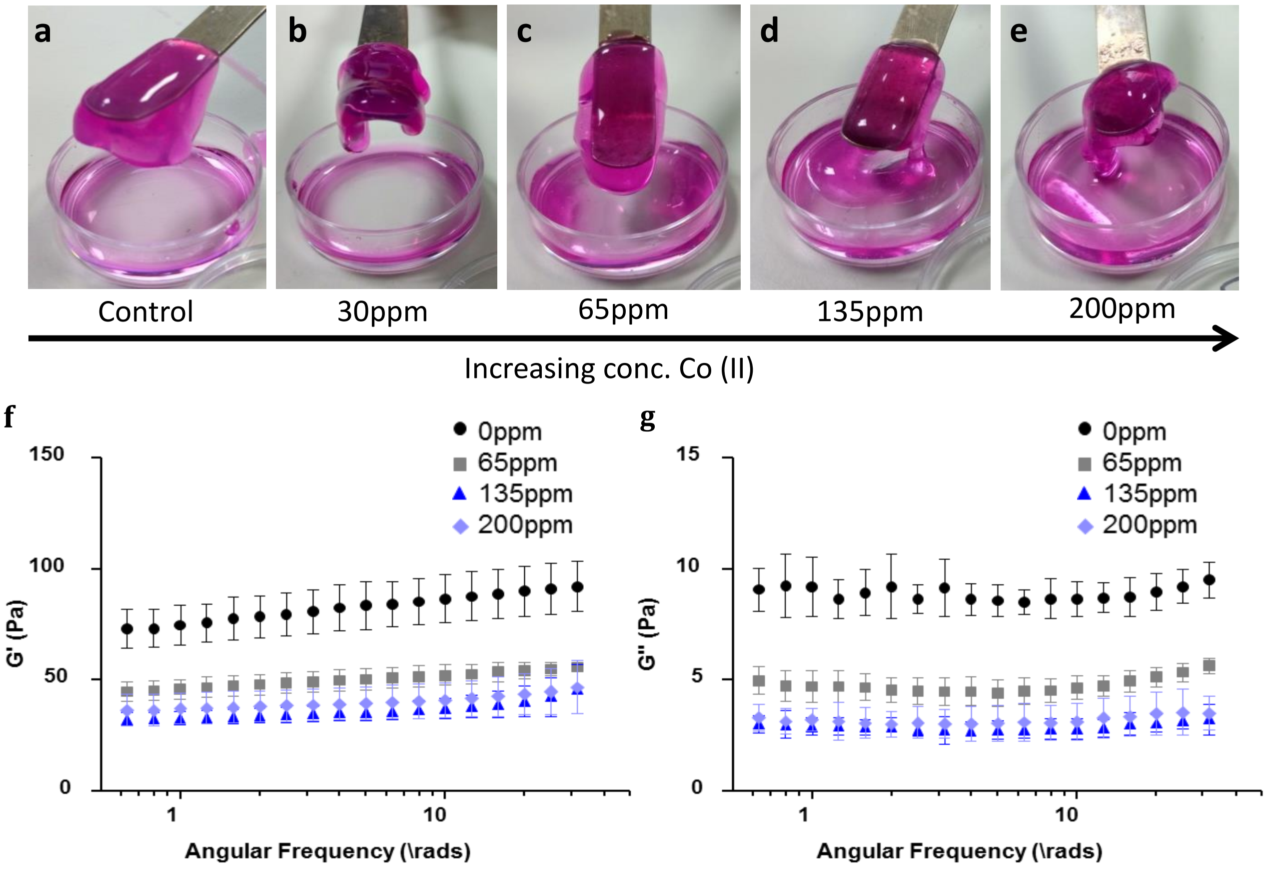

Figure 4.8: [a-e] Images of CoCol gels being lifted from dishes with increasing concentrations of Co(II). [f] Storage modulus, G' and [g] loss modulus, G" from a frequency sweep with a fixed strain. A decrease in the storage modulus of the gel indicates a reduction in stiffness.

The effect of these modifications to the network structure of the collagen matrix was determined using small-deformation oscillatory rheology, shown in figure 4.8f-g. There was an overall reduction in the storage (G') and loss (G") moduli of the collagen gels with the addition of Co(II) at all concentrations, which corresponds to a reduction in the stiffness of the collagen gel (138). It could not be determined whether the reduction in G' and G" were significant as the sample size was not large enough to produce reliable statistics, greater repeats would need to be performed.

The reduction in stiffness of the CoCol gels is shown visually in the images in figure 4.5a-e. At higher Co(II) concentrations the collagen gel matrix, at 1mg/ml collagen, was unable to maintain its structure. This reduction in bulk stiffness may be due to the heterogeneity observed (regions of low density fibrils) in AFM and RCM as a result of Co-collagen interactions.

4.3.5. Determining the cellular response to Co-collagen gels

Considering the underlying structure of the ECM provides the physical and chemical cues to direct cell function and proliferation, biological assays were performed to determine the cellular response to CoCol gels. MC3T3s and HDFs were cultured both on and in CoCol gels and imaged after 2/3 days respectfully.

MC3T3s maintained a relatively high viability, compared with the control, when seeded on CoCol gels up to Co(II) 135ppm (figure 4.9a), as seen by the number of live cells (green). In comparison, the viability of MC3T3s seeded on cell culture plastic within Co-doped media only maintained a high viability for Co(II) concentrations up to 65ppm (figure 4.9b). This was supported by an AlamarBlue assay (figure 4.9c). A concentration of 65ppm Co(II) corresponded with a 26.5% reduction in AlamarBlue when seeded in Co-doped media, compared with a 20% reduction on the CoCol gel. It can be seen that MC3T3s on CoCol gel with the highest Co(II) concentration corresponded to a lower reduction in AlamarBlue (23%) than at the lowest Co(II) concentration for cells within Co-doped media. This indicated a greater decrease (relative to the control) in cell proliferation when Co(II) is present in the media, rather than within the collagen gel. The MTT assay shown in figure 4.9d further indicated a steep decrease in the proliferation

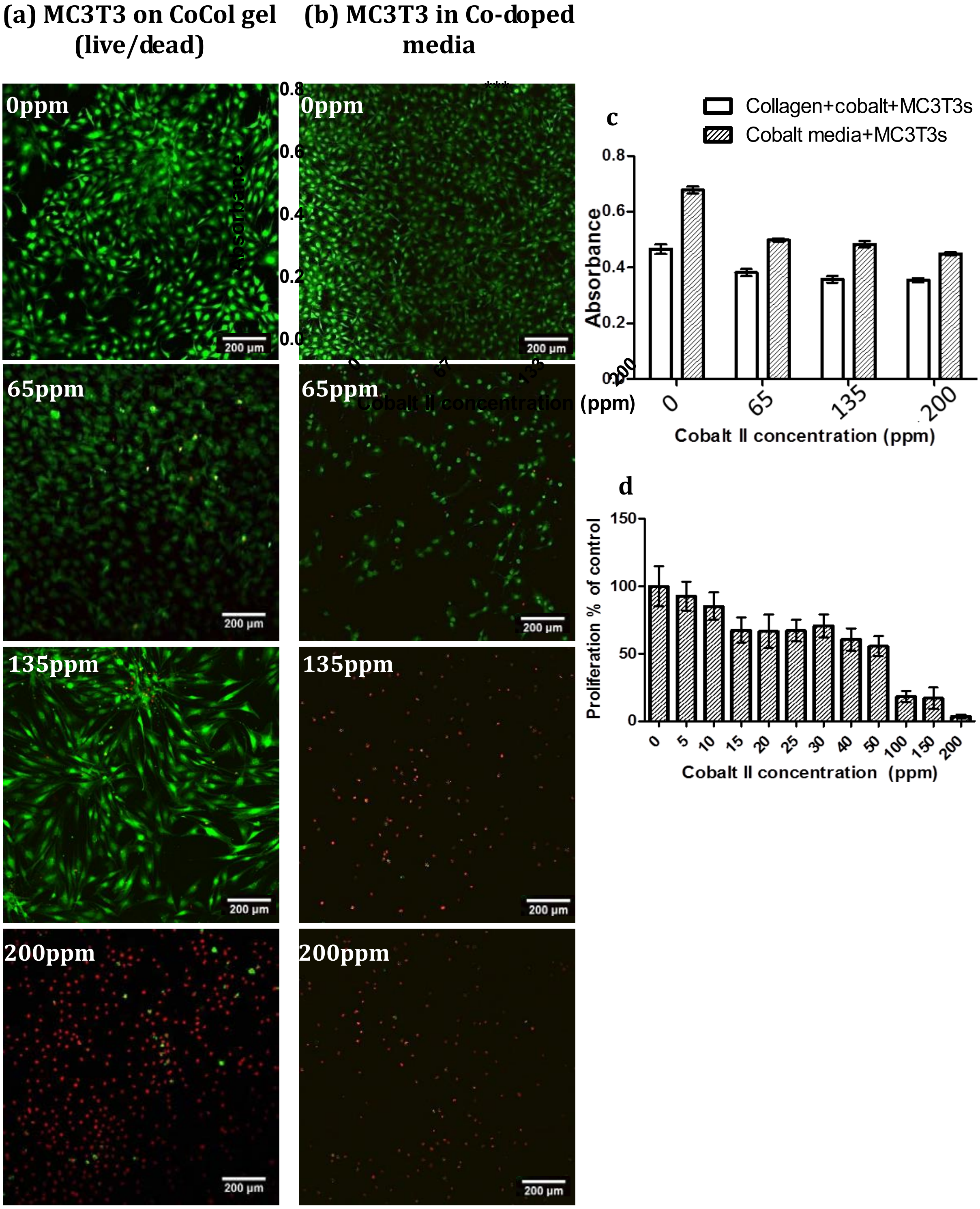
(a) MC3T3 on CoCol gel (live/dead)

(b) MC3T3 in Co-doped media

Figure 4.9: MC3T3 cells seeded [a] on top of CoCol gels and [b] within Co-doped media, after staining with calcein AM (green) and propidium iodide (red) for live/dead contrast. All images were acquired using a confocal microscope and imaged at day 2, scale bar = 200µm. [d] AlamarBlue assay performed on cells on CoCol gels and within Co-doped media. [e] MTT assay performed on cells within Co-doped media only to assess proliferation. All data suggests a decrease in cell viability and proliferation

of MC3T3s as a result of Co-doped media. These results, in combination, suggest that any change in cell viability or proliferation of cells seeded on CoCol gels is not due to direct cell-Co(II) ion interactions and thus further supports that Co(II) ions must be in some way bound within the collagen matrix.

In addition, a change in morphology of the cellular cytoskeleton was observed. HDF cells (used due to their characteristic elongation) were seeded both on and within CoCol gels and stained with ActinRed 555 to show the actin filaments (a primary structure within the cytoskeleton). Figure 4.10a-b shows that the characteristic elongation of the cells, both on the surface and within the CoCol matrix, is reduced at 135ppm Co(II) prior to reduction of the cytoskeleton entirely at 200ppm Co(II).

Furthering the cellular investigation, the effect Co(II) inclusion has on the cell-mediated contraction of the collagen matrix was examined by observing the contraction of the collagen matrix over time. Figure 4.10c shows no contraction was observed after 3 days for any Co-dosed collagen (note: increase in diameter likely due to collagen swelling from surrounding media). When cells attach and exert a force on collagen fibres, either the matrix will contract or the cells will be propelled (166). Given elongation was observed for lower Co(II) concentration (<65ppm), it would be expected that contraction would occur.

These results, in combination, suggested that the presence of Co(II) within the collagen matrix influenced cellular proliferation, morphology and function. It appears unlikely that this was due to direct cell-Co ion interactions, but rather that it may be the structure of the CoCol gel that is affecting cellular behaviour.

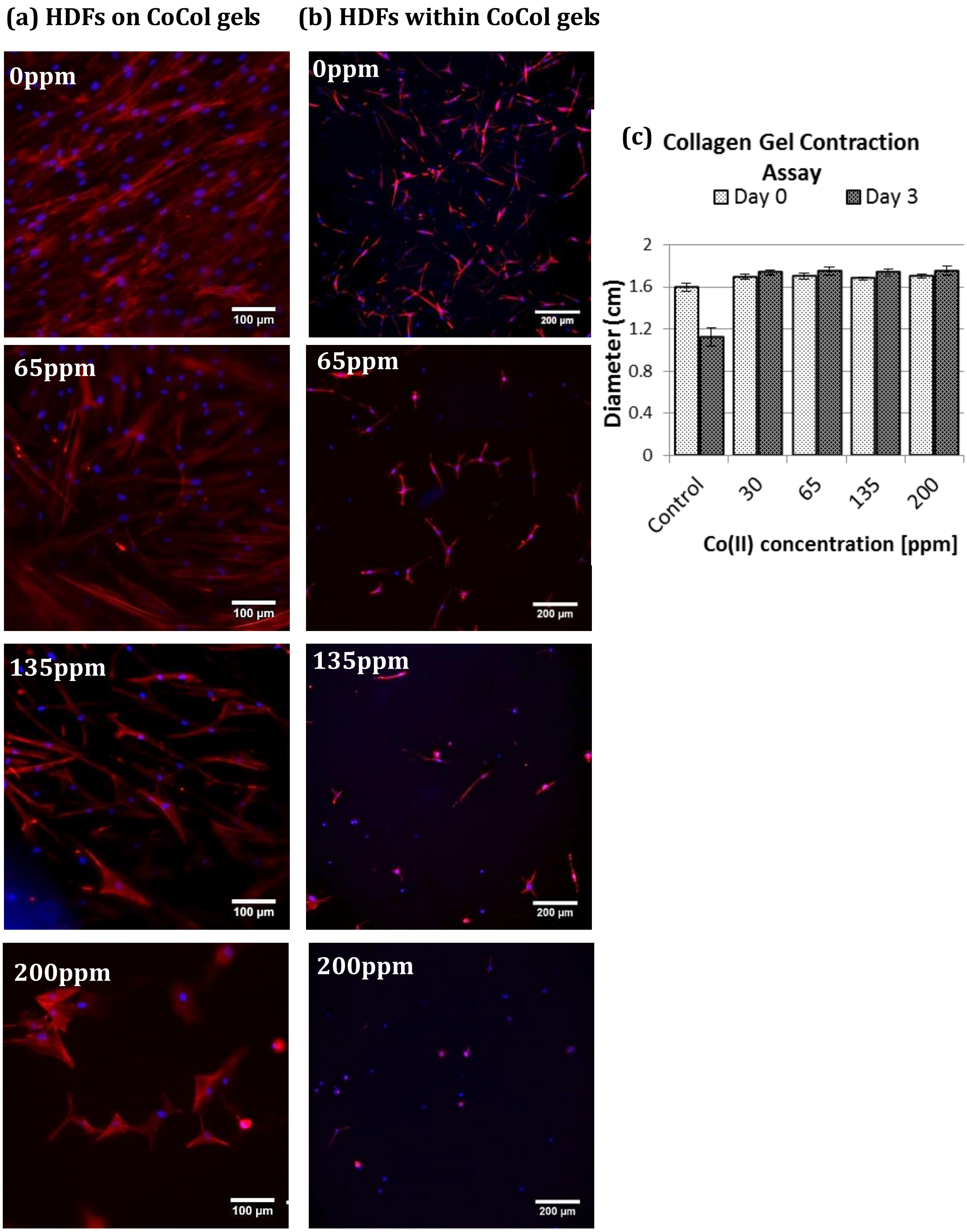

Figure 4.10: HDFs seeded [a] on the surface of CoCol gels, scale bar = 100µm and[b] within CoCol gels, scale bar = 200µm. Lower seeding densities for within CoCol gels meant a lower magnification was required to observe a larger field of view. All images show staining with ActinRed 555 (red) and DAPI (blue) for cytoskeleton/nucleus contrast and were acquired at day 3. [c] Shows the collagen gel contraction assay for HDFs within collagen after 3 days, n=3. No contraction was observed with the presence of Co(II).

4.3.6. Determining potential binding sites between cobalt ions and collagen

The release studies showed no significant release of Co(II) over time, and proliferation studies showed the presence of live cells on 135ppm CoCol gels. This suggested that Co(II) was bound within the matrix. As such, it was likely that the binding sites for Co(II) were directly affecting the way in which cells attached and therefore proliferated. In addition, a lack of available attachment sites may have prevented enough traction being exerted to result in compaction of the matrix. In order to determine the preferential binding sites between collagen and the Co(II) ions, Raman spectroscopy and differential scanning calorimetry (DSC) for 0 and 200ppm were performed.

Figure 4.11a shows the characteristic protein peaks present in the Raman spectra for 0ppm and 200ppm Co(II), such as the secondary amide peak (1205.08 and 1207.25cm^{-1}) and the C=O peak (1606.75 and 1607.76cm^{-1}) (163). Principal component analysis (PCA) produced two principal components (PCs) that contain the maximum variance from the data. PC1 and PC2 described 67.91% and 6.07% of the data respectively. A scores plot of these two PCs, revealing which spectra are similar, is shown in figure 4.11b, for which two clusters were obtained corresponding to the 0ppm and 200ppm collagen samples. Figure 4.11c shows the loading vector for the 1st PC as a function of wavelength. Intense peaks in this plot indicated which wavelengths contributed to the most prominent change between the sample and the reference (162). The largest variation between the Raman spectra for the control collagen gel compared to the 200ppm CoCol gel occurred at 869 cm^{-1} and 1000cm^{-1}, corresponding to a C-O bond (163), with this vibration being suppressed in the 200ppm CoCol gel.

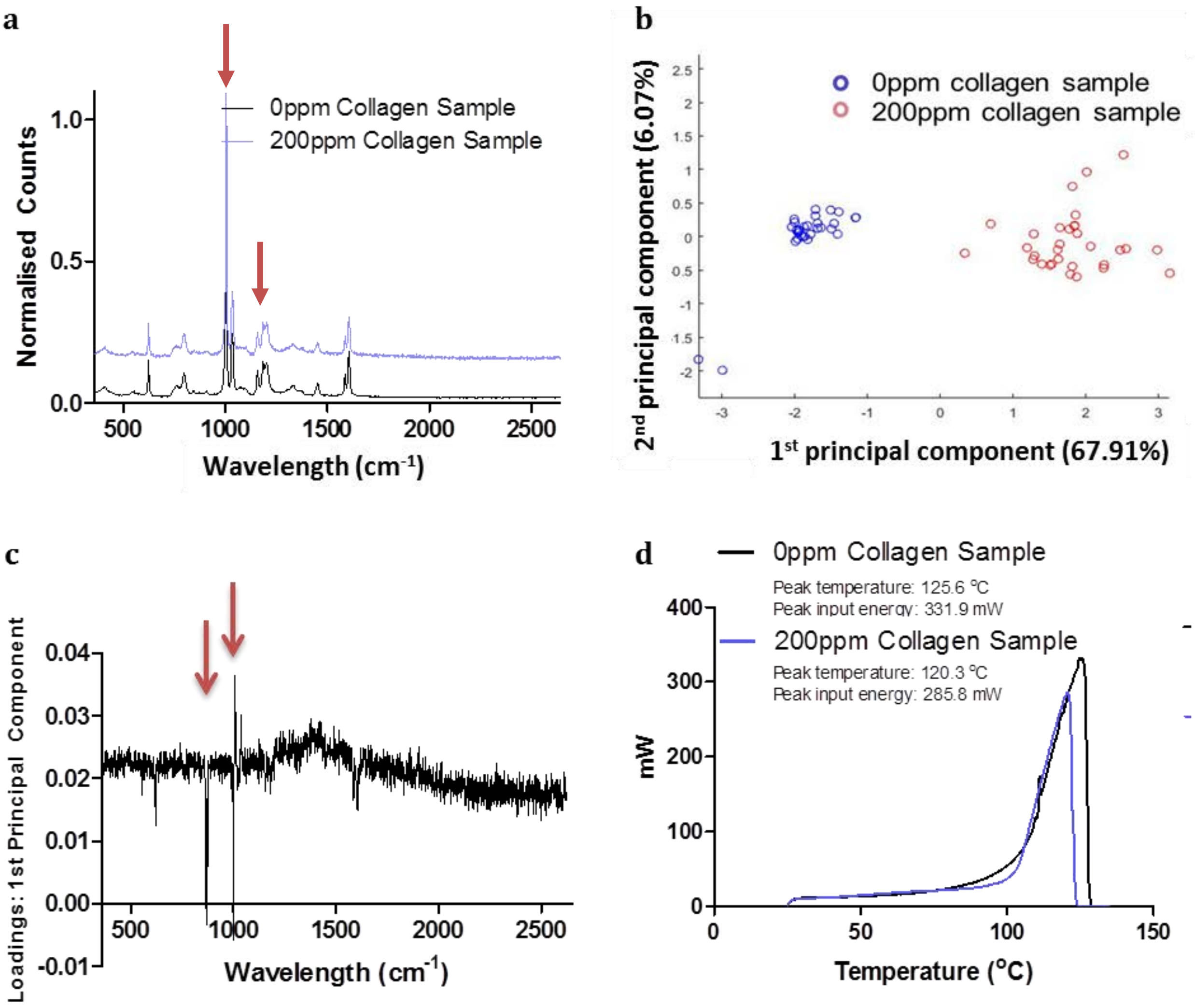

Figure 4.11: [a] Raman spectra of both 0ppm and 200ppm collagen gels, [b] a scores plot of the first two principal components shows the clusters corresponding to 0 and 200ppm, [c] A loadings plot of the first principal component indicating changes at 1000 cm^{-1} and 869 cm^{-1}, see the arrows. [d] Differential scanning calorimetry measurements indicating a reduction in energy required to remove bulk water between 0ppm and 200ppm CoCol gels.

In addition, the DSC results (figure 4.11d) show the bulk water within the 200ppm Co(II) collagen sample was removed at a temperature of 120.3°C, which is 5°C lower than that of the 0ppm collagen sample (125.6°C). Furthermore, the energy required to completely remove the water bound within the 0ppm collagen sample is 14% greater than that for 200ppm. This suggested that bulk water within the 200ppm CoCol gel was not bound as strongly as that within the 0ppm collagen sample. Considering the only difference between the two samples is the presence of Co(II), it was highly likely that the Co(II) was binding to the collagen fibril in such a way that reduced the number of tightly bound water molecules.

4.4. Discussion

The introduction of Co(II) ions to collagen gels resulted in changes to both the collagen gel structure and the cellular response to the collagen matrix. Co(II) ions had an impact upon the kinetics of fibril formation, as the time taken for fibrillogenesis to occur increased upon the addition of Co(II). This indicated Co(II) ions may have interfered with the molecular ordering of the collagen during self-assembly. This was supported by the results from the CD data where the presence of the characteristic positive and negative peak indicated that the collagen triple-helix was maintained (126, 127). However, this study contained limitations due to the equipment used. The usual operating region for this specific CD equipment is >200nm, as it suffers from low sensitivity below this. This suggested that the large variation around the negative peaks may have been due to low signal-to-noise and that the negative peak measurement may suffer from a "peak cut-off" effect[4]. The large negative peak should have occurred around 200nm, where sensitivity drops. Despite this, an increase in the amplitude of the positive peak with Co(II) concentration may be associated with tighter packing of the triple-helix (129). This measurement alone was insufficient to conclusively prove Co(II) caused

---

[4] This is where low signal-to-noise means the wavelengths in that region are not recorded, resulting in a sharp jump from the high signal-to-noise region to the low signal-to-noise region, effectively "cutting-off" the remaining section of the peak.

tighter packing of the collagen molecule. However, it did indicate that Co(II) may have modified the triple-helix in some manner.

Upon completion of fibrillogenesis, AFM and confocal microscopy (RCM) were able to show how the structure of the collagen matrix at different length scales was affected by the addition of Co(II) ions. AFM showed a significant decrease in the D-banding for Co(II) concentrations >135ppm compared with the control. If the characteristic band spacing is considered in terms of being ~¼ length of a collagen molecule (117), then any change in the collagen molecule packing could result from modifications to the collagen molecule itself. This data supported the results from the CD of collagen, whereby an increase in the positive peak amplitude was observed, implying (based on literature (129)) tighter packing of the triple-helix. In addition, the AFM images showed how the presence of Co(II) ions resulted in aggregation of individual fibrils. This fibrillar aggregation was seen in studies observing the effect Cr(III) on the structure of collagen (122, 123). Cr(III) formed nanometre-sized clusters between the fibrils, displacing water, resulting in additional inter-fibrillar cross-linking leading to aggregation. This was further supported through RCM. The collagen control (0ppm) showed a dense homogeneous network of fibrils, whereas the presence of Co(II) resulted in a heterogeneous network, containing regions with higher and lower densities of fibrils. This suggests that the Co(II) ions interact directly with the matrix to create these areas of agglomeration, indicating that Co(II) is most likely present within these high density regions.

The Co(II) distribution throughout this heterogeneous bulk matrix is interpreted through release studies and via x-ray fluorescence. Incubation of the

CoCol gels over time showed no significant difference between the amounts of Co released at day 1 vs. day 6, suggesting no long term release and that the Co(II) must be bound in some way within the collagen matrix. X-ray fluorescence showed an average 3-fold increase in the relative intensity of Co fluorescence observed at selected sites. While it is reasonable to assume that these areas of increased Co intensity corresponded to high density regions of collagen, higher magnification imaging modalities must be used and correlated with microscopy of the fibrils to confirm.

During the process of CoCol gel production the overall bulk structure appeared less stiff with increasing concentrations of Co(II). At higher Co(II) concentrations the CoCol matrix was unable to maintain its structure. As such the influence of Co(II) ions on the mechanical properties of collagen was investigated using oscillatory rheology. This showed a decrease in the storage and loss moduli (G' and G'' respectfully), which corresponded to a reduction in the overall stiffness (138). It is likely that the heterogeneity observed in local densities of the collagen matrix resulted in this change to the bulk matrix property, due to low density regions within the matrix acting as 'weak points' within the structure.

The combination of these results indicate a strong probability that Co(II) ions are bound within the collagen matrix in some manner, as is the case with Cr(III) (122, 123). This was further reinforced by the cellular investigations. The AlamarBlue assay showed that MC3T3s exposed to CoCol gels vs. non-bound Co(II)-doped media experienced a greater decrease (relative to the control) in cell proliferation when Co(II) was present in the media rather than within the collagen gel. This was echoed by the live/dead staining performed in figure 4.9a-

b. Therefore, this suggested that any decrease in proliferation and viability is not due to cell-Co(II) ion interactions, but rather, changes in the collagen matrix affecting the cell-collagen interactions.

Cells are known to interact with the extracellular matrix through integrin-mediated pathways depending upon the cell type (164, 165). These interactions play a key role in matrix formation as they facilitate cellular adhesion and signalling (166). Cellular adhesion is primarily regulated by GFOGER and/or RGD peptide sequences[5] (165), the expression of which are dependent upon the tertiary structure of the triple-helix (167). Changes in the conformation of collagen can result in alteration of the accessibility of the binding motifs required for integrin-mediated cellular attachment. This was observed in a study using collagen and gelatin formulations to investigate cellular binding mechanisms (168). Consequently, the decrease in proliferation observed with increased Co(II), given the small concentration of Co detected in the media, was most likely due to alterations of the collagen structure. As stated, the findings from CD and AFM suggested a tighter packing of the collagen triple helix. This change may result in the required receptor sites, through which collagen-cell interactions occur (169), no longer being exposed. Further fluorescent imaging also showed the presence of Co(II) changes the morphology of cells - reduction of the characteristic elongation of HDFs, prior to the reduction of the cytoskeleton completely at 200ppm Co(II) – and that the function of these cells is affected – no reduction in collagen diameter after 3 days during a collagen contraction assay. Given cellular attachment to collagen results in either cellular propulsion or matrix contraction (170), a lack of

---

[5] GFOGER has high affinity for $\alpha1\beta1$, RGD is a binding receptor for fibronectin.

available attachment sites may have prevented enough traction being exerted resulting in compaction of the matrix. In order to determine whether Co(II) is reducing the available attachment sites, the preferential binding sites for Co(II) were investigated.

When cobalt (II) chloride hydrate, the Co(II) source used, is dissolved in water, $[Co(H_2O)_6]^{2+}$ is the predominant cation (171). This positive complex has the potential to interact with either the individual fibrils directly, through the carbonyl or hydroxyl groups, or with the water molecules in the hydration layer, becoming incorporated into the water bridge (119, 120). Previous studies into the interactions between silica and collagen show preferential binding to terminal sites of the collagen molecule (172), while studies between Cr(III) and collagen shows Cr(III) displaces the bound water resulting in dehydration of collagen and fibril aggregation (122, 123). Raman spectroscopy showed a reduction in the C-O (hydroxyl) bond peak at 869 cm^{-1} and $1000cm^{-1}$, with this vibration being suppressed within the 200ppm sample. This suggested that the Co(II) ions were interacting with a C-O (hydroxyl) group (120, 173, 174). Given the previous studies mentioned, it is possible that Co(II) is may be binding with the C-O structure at the carboxylic (C-propeptide in figure 3.1) terminus. In addition the DSC shows a decrease in the required energy and temperature to remove bound water from the 200ppm CoCol gel. This suggests Co(II) interactions with the collagen may be preventing water binding by blocking/preventing the accessibility of these binding sites. This dehydration of collagen, seen in previous studies investigating Cr(III)-collagen interactions (122, 123), may also contribute to the fibril aggregation leading to the heterogeneity observed in AFM and RCM.

In addition, the possible inaccessibility of potential binding sites due to blocking or altering collagen assembly may contribute to the reduction in cellular attachment and function previously discussed.

4.5. Conclusion

This chapter has shown that Co(II) ions have an adverse effect on the formation of collagen fibrils in type I collagen gels. While the collagen triple-helix appears to be maintained, a significant decrease in the D-banding of the fibrils was observed (>135ppm Co(II)). In addition, an increase in the concentration of Co(II) ions (max. 200ppm) lengthens the time taken for the collagen matrix to form. The final matrix contains areas of both high and low fibril densities, resulting in structural heterogeneity and a reduced bulk stiffness of the collagen gel with increasing Co(II). This modification to the matrix reduces the attachment and proliferation of MC3T3 osteoblasts, results in a change in the cellular morphology of HDFs, and ultimately leads to a decrease in cell viability and cellular function (contraction). In addition, it has been shown that not only is there no significant release of Co(II) from the collagen matrix over time, suggesting that the Co is bound within the collagen matrix, but it has also been suggested that this binding occurs at the hydroxyl groups present within the collagen molecule. It is possible that this binding may block crucial bonds required for stabilisation of the matrix, leading to the decrease in bulk stiffness and water loss observed.

This chapter contributes insight into how type I collagen, the primary component of the extracellular matrix, is modified by Co(II), a metal degradation product of CoCr hip replacements. It cannot be concluded that observed tissue necrosis and unexplained MoM implant failures are a result of changes to the extracellular matrix. However this work emphasises the importance of studying matrix interactions in order to understand long-term biocompatibility, as current standards typically rely on 2D cellular cultures and do not take into account the complexity of the extracellular matrix. Ultimately, on a macroscopic level, Co(II) influences the properties of type I collagen gel which appears directly linked to how Co affects the microscopic level of collagen. This fundamentally changes how cells adhere to and will subsequently interact with collagen. Further work is required to determine the exact binding site of Co(II) to collagen and additional CD measurements with greater sensitivity <200nm will allow for better interrogation of the conformation of the collagen molecule itself. In addition, further experiments may be performed to assess the cellular response to the matrix itself, such as quantification of initial cellular attachment and the binding of fibronectin to the surface. This may inform how Co(II) is able to modify the matrix resulting in an adverse cellular response, as it will give an indication as whether integrin-mediated pathways are being affected by the presence of Co(II).

Chapter 5

Precipitation of metal ions in media

5.1. Introduction

Cobalt-chromium-molybdenum alloys have widespread commercial uses, particularly within the medical industry for load bearing metal implants, for example hip arthroplasty. However, even with their improved resistance to wear (38), these alloys still succumb to the generation of degradation products, consist of particulate and ionic debris. There are many published studies regarding the biological impact *in vitro* of CoCr debris on 2D cell cultures, however research typically focusses on CoCr/Co/Cr metal particles (11, 15, 16, 88, 154, 175) or Co(II)/Cr(III) ions (40, 79, 90, 113, 125, 147, 153, 154). In addition to literature discussing metal particulate and ionic debris, there are reports of Cr phosphate, $CrPO_4$, as an observed corrosion product, for which there is little research beyond some attempts at investigating cellular response in simple cultures (176). Corrosion of the CoCr metal has been shown to occur from either the bulk implant itself or from the wear particles produced (40, 53, 85), yet despite this, only one group has published in reference to precipitation produced by Co/Cr ions (85, 93, 94). The biological consequences of Co and Cr will depend on how they are presented - either in metallic form, ionic form or precipitated. Consequently, understanding the available degradation products is crucial to understanding potential cellular responses.

Tkaczyk et al. (85, 93, 94) reported that Cr(III) readily precipitated at low concentrations (50ppm) in Dulbecco's modified eagle medium (DMEM) and Roswell Park Memorial Institute 1640 (RPMI-1640) cell culture media with and without serum present. Co(II) or Cr(IV) precipitate greater than 0.4nm (the detection limit of the TEM) was not observed. The Cr(III) complexes that formed contained phosphates and proteins, however the exact composition varied depending on the media, and they were typically referred to as Cr-complexes. The fact that Cr(III) precipitates, may be a contributing factor in why Cr(III) ion levels detected in patients tends to be lower than Co(II) (80, 87). Current assumptions are that less Cr(III) is produced. However, these experiments involve leaving CoCr particles in various media for given time frames and then centrifuging the sample and testing ion levels in the supernatant only (6, 12, 88, 155). Therefore any precipitation formed is now in the discarded pellet.

While Tkaczyk et al. performed a comprehensive study into the size, composition and organic bonds present in the Cr-complexes, the study was only performed in DMEM and RPMI-1640 (cell culture media), and the effect of pH was not assessed. These are important factors because both fluid composition and pH can vary depending on the local environment around the hip implant. Hip arthroplasty revisions have observed highly acidic environments, due to crevice corrosion at mixed metal boundaries, resulting in pH <3.0 (177, 178).

The lack of investigation into the effect of pH on the precipitation of Cr-complexes is significant, given the prevalence for studies to disregard the concept of precipitation during their analysis and conclusions. For example, Posada et al.

(12) investigated the release of Co and Cr ions from CoCr particles at pH 4 and 7, and concluded that there was greater dissolution at a lower pH. Particles were incubated in cell culture media for 24 hours before centrifuging and the Co and Cr content in the supernatant measured. While it can be accepted that more dissolution will occur at a lower pH, given crevice corrosion theory (53), this method cannot be used to predict the concentrations of Cr(III) released when the measure for such a conclusion comes only from the Cr content measured in the supernatant, ignoring the pellet. This methodology is fundamentally flawed as the potential for precipitation has been disregarded.

The experiments in this chapter were performed to expand upon the work reported by Tkaczyk et al. (85, 93, 94) and aim to determine whether the pH and composition of the local environment impacts the amount of precipitation and speciation of precipitated products respectfully.

5.2. Methodology

5.2.1. Precipitation of Cr(III) in various media

A Cr(III) stock solution was made by dissolving chromium (III) chloride ($CrCl_3.6H_2O$) (Sigma-Aldrich) in sterile water and syringe filtered using a 0.22µm membrane. 50ppm of this Cr(III) stock solution was then added to 1mL of a given media, of neutral pH, and left at 37°C for 1hr. These samples were then centrifuged at 5,000rcf for 10 minutes in a micro-centrifuge, and the supernatant removed leaving a pellet of precipitation behind. The pellet was then 'washed' - re-suspended then centrifuged at 5,000rcf for 10 minutes – in sterile water (x3) and 100% ethanol (x1), before being left to air dry undercover. Ethanol was used in the final step in order to hasten the drying process, removing residual water leaving only the precipitate.

The media used were phosphate buffered saline (PBS), simulated body fluid (SBF), Dulbecco's modified eagle media (DMEM) (Sigma-Aldrich), DMEM with 5% added human serum (DMEM+5%HS), Roswell Park Memorial Institute 1640 Medium (RPMI-1640) (ThermoFisher Scientific), RPMI-1640 with 5% added human serum (RPMI-1640+5%HS), and *ex vivo* human synovial fluid (HSF).

For the DMEM and RPMI-1640 with HS samples, only 5% HS was used as this was in line with the study by Tkaczyk et al. (85), and this chapter began as an extension from that work.

5.2.2. Preparation of biological media (HS, HSF & SBF)

Human serum (HS) was obtained from whole blood of volunteers under ethical approval from the University of Birmingham (ref: ERN_12-1184). Serum was obtained using standard protocols. Whole blood was obtained by a medical professional and left to clot at room temperature. This was then centrifuged at 2000rcf for 10 minutes to remove the clot, resulting in a supernatant of serum. This supernatant was removed and stored at -80^{o}C until use.

Human synovial fluid (HSF) was acquired under ethics, obtained for this project, from the Human Biomaterials Resource Centre (HBRC) (Application N#: 14-198). The samples themselves were obtained from patients at the Royal Orthopaedic Hospital (ROH) undergoing revision surgery for MoM hip implants. During surgery, the samples were placed immediately in sterile containers and into a box of dry ice for transportation to the lab where they were stored at -80^{o}C. Before use, HSF was thawed and centrifuged at 2000rcf for 10 minutes to remove any tissue remnants and potential wear particles.

Simulated body fluid (SBF) was prepared using the protocol from Kokubo et al. (179). This protocol for SBF focuses on obtaining a solution, buffered to pH 7.4, with ion concentrations equal to that of human blood plasma.

5.2.3. Monitoring pH after addition of Cr(III)

A FiveGo™ pH Meter (Mettler-Toledo) was calibrated using a 2 point calibration method and used to automatically monitor pH over time, set to record pH every 2 minutes. This was used to record the change in pH of RPMI-1640 media after the addition of Cr(III).

A volume of 10mL RPMI-1640 media in a 50mL falcon tube was placed in a water bath maintained at 37^{o}C. After the temperature equalised, the pH of the media was adjusted, using hydrochloric acid or sodium hydroxide, to pH 4 or 7.5, respectively.

Cr(III) was then added, to a final concentration of 50ppm, in-line with the methodology from Tkaczyk et al. (85). The falcon tube was covered with plastic wrap to prevent evaporation and a pH probe inserted through a hole to allow measurements to be recorded every 2 minutes for 2 hours.

5.2.4. Flame Absorption Atomic Spectroscopy of Cr(III) in supernatant

Flame Absorption Atomic Spectroscopy (FAAS) is an analytical technique used to determine the concentration of metals present in a given sample (typically a liquid or dissolved sample). In FAAS, a nebulizer vaporises the solution containing the metal ions and the finest spray is aspirated into a flame. Here the atoms transition to the first excited state whereby they are able to absorb a defined wavelength of light from a lamp, specific to each element. The remaining light is detected and the amount of light absorbed is calculated, which is dependent upon the concentration of the element present. Concentration is determined through the use of a calibration curve using a range of standards with known element concentrations.

Volumes of 6mL unsupplemented DMEM, in a 50mL falcon tube, were pH adjusted, using hydrochloric acid and sodium hydroxide, to pH 4, 5, 6, 7, 8, and 9. The DMEM was brought to 37°C in an incubator (37°C, 5% CO_2, 95% air) (Sanyo Electric Co. LTD, Japan) and Cr(III) solution was added to a final concentration of 50ppm, before sealing and incubating (at 37°C) for 1 hour. Samples were then centrifuged at 16,000rcf for 10 minutes to separate out precipitation and the supernatant removed and stored at -20°C.

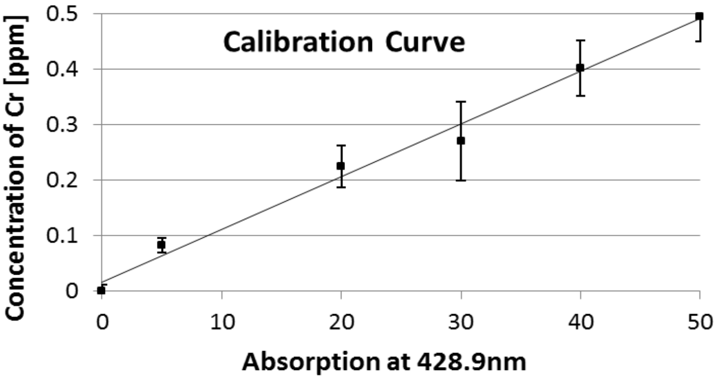

Figure 5.1: Calibration curve for flame atomic absorption spectroscopy (FAAS), produced using standards of known Cr(III) solutions. Measurements were performed in triplicate and the mean acquired, with error bars depicting the standard deviation. The linear line of best fit was produced by fixing the intercept at zero and using weighted linear regression.

FAAS measurements were performed on a Varian Spectra AA-300 flame system (Varian Inc, Agilent Technologies) with a lamp current of 7mA and acetylene fuel in air. The samples were fed into the FAAS to be nebulized. For the initial Cr(III) concentration of 50ppm, the emission wavelength measured was 428.9nm with a slit width of 0.2nm was used, which provided an optimum working range for 1-100ppm. Calibration standards were made by diluting Cr(III) stock solution in sterile water to various dilutions <50ppm. The calibration curve was produced using weighted linear regression with a fixed intercept at zero, shown in figure 5.1.

5.2.5. Scanning Electron Microscopy

Cr(III) complexes produced using the method in section 5.2.1 were re-suspended in ethanol and dried onto silica wafers. Ethanol was used due to the enhanced drying time in comparison to water. Samples were then and sputter coated with a 5-8nm conductive gold layer. Cr(III) complexes formed using RPMI-1690, DMEM, RPMI-1690 + 5%HS and DMEM + 5%HS were imaged using a field emission gun-scanning electron microscope (FEG-SEM) (Phillips XL30-ESEM-FEG), while those formed in PBS and SBF were imaged using a tungsten beam SEM (Carl Zeiss EVO MA 10 SEM). The SEM's were operated at acceleration voltage of 10kV, with a spot size of 3.0, working distance around 10mm, and detection via secondary electrons.

5.2.6. Particle size analysis of SEM images

After the acquisition of SEM images of Cr(III) complexes, particle size analysis was performed using Fiji, a Java-based processing package based on ImageJ (180). Images were thresholded in order to produce a binary, black and white, mask, and AnalyzeParticles (a standard plugin) was then applied to generate data on the diameter and volume of the particles present. Approximately 100 particles were used per sample to determine the mean particle diameter and standard deviation from the mean.

5.2.7. Synchrotron-XRF & Synchrotron-XANES

To interrogate at a sub-micron resolution, samples of precipitate were produced by doping HSF (preparation method in section 5.2.2) with Co(II) and Cr(III) at different concentrations. A Cr(III) only concentration was chosen as an extension to the precipitate generated in culture media. In addition, two ratios were chosen for Co(II) to Cr(III). The first, representing the ratio of the weight percent (wt%) contributions for the bulk CoCr base metal (51) and the second, the inverse of this as an extreme comparison (further ratios between these were prepared but time constraints at the beamline prevented their interrogation).

HSF was prepared and metal ions added in the following concentrations (future reference for each concentration given):

- **Control** – HSF only
- **CrHSF** - 100ppm Cr(III) in HSF
- **Co:2.6CrHSF -** 38ppm Co(II) & 100ppm Cr(III) in HSF, Co:Cr ratio is 1:2.6
- **2.6Co:CrHSF -** 300ppm Co(II) & 118ppm Cr(III) in HSF, Co:Cr ratio is 2.6:1

These samples were incubated for 12 hours at 37^{o}C before centrifugation (at 5,000rcf for 10 minutes), followed by x2 washes with sterile water and x1 with ethanol. In order to ensure samples were completely dry they were left in a desiccator for 2 days.

Samples were then transported to the European Synchrotron Radiation Facility (ESRF) (Grenoble, France) and spread onto 4μm thickness Ultralene windows (Spex SamplePrep, Metuchen, NJ, USA) and placed in a sample holder specific to the ESRF beamline. Analysis was performed under vacuum on the scanning x-ray microscope (SXM) end-station on the ID21 beamline.

ID21 uses a fixed exit double crystal Si(111) monochromator to select and scan the energy of the beam. This is then focused using a Fresnel zone plate. Measurements are made using energy dispersive detectors; a 7-element high purity germanium detector and silicon drift diode. The beam was focused to a footprint of 600 x 600nm, and an incident energy of 7.8keV was used to allow excitation of cobalt and chromium. XRF maps, windowed for Co and Cr were produced to define regions of interest for point XANES analysis, XANES spectra were produced by conducting energy scans at a total of 117 sequential energy points ([5970, 5985, 5], [5985.5, 6030, 0.5], [6033, 6099, 3], using notation: [starting energy (eV), finishing energy (eV), energy resolution (eV)]). Co XANES was not performed due to restrictions on large beam changes during the experiment.

5.3. Results

5.3.1. Determining the effect of pH on the initiation of Cr(III) precipitation

Expanding upon the work presented by Tkaczyk et al. (85, 93, 94) pH was investigated as a factor for the initiation of Cr(III) precipitation. An initial concentration of 50ppm Cr(III) was added to RPMI-1640, which had been pH adjusted (between pH 4-9). The Cr content remaining in the supernatant after 1 hour was determined through FAAS. While a pellet was only observed in samples of pH ≥6, pH 4 and 5 media only contained 36.4±7.3ppm and 21.1±8.0ppm respectfully. This suggests some precipitation may have occurred, otherwise it would be expected that Cr concentration would remain close to the initial 50ppm. Figure 5.2a shows how increasing the pH of the media results in a decreasing concentration of Cr measured in the supernatant, suggesting more Cr(III) precipitation is occurring. This is supported by the visual observations of the pellet size in figure 5.2b, where a higher pH corresponded with the largest pellets.

Following this, monitoring the pH of RPMI-1640 over time after Cr(III) addition was performed to determine whether pH was more likely to be influencing the yield or the initiation of precipitation. As it was noticed that the pH of a given media decreased upon the addition of Cr(III), the pH of RPMI-1640 was monitored over 2 hours for two starting conditions, pH 4 and 7.5, shown in figure 5.2c and 5.2d respectfully. For the starting condition of pH 4 (pH 3.7 after Cr(III) addition) there was a small decrease in pH over 2 hours. However, for the starting condition of pH 7.5 (pH 7.2 after Cr(III) addition), the pH increased in excess of the initial starting condition. In addition, both samples were centrifuged

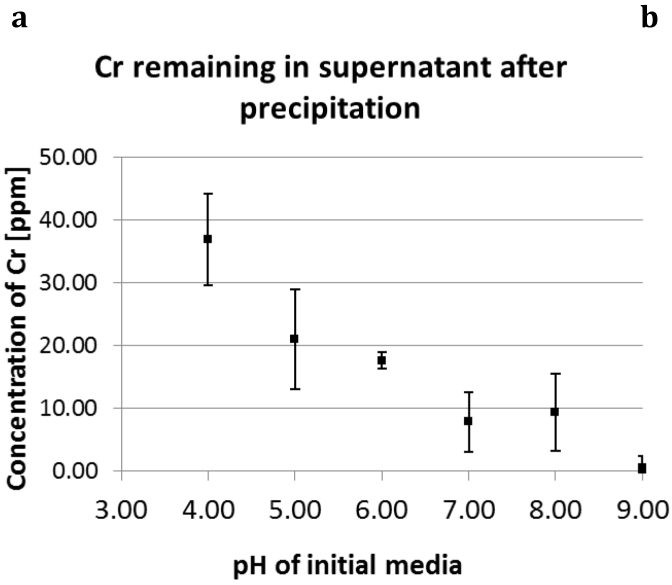

b

pH ref	pH before adding Cr(III)	pH (instantly) after adding Cr(III)	Notes
4	4.07	3.83	No pellet seen after centrifuging
5	5.18	4.85	
6	6.17	5.95	Small pellet seen
7	7.12	6.96	Largest pellets seen
8	8.02	7.49	
9	8.95	8.71	

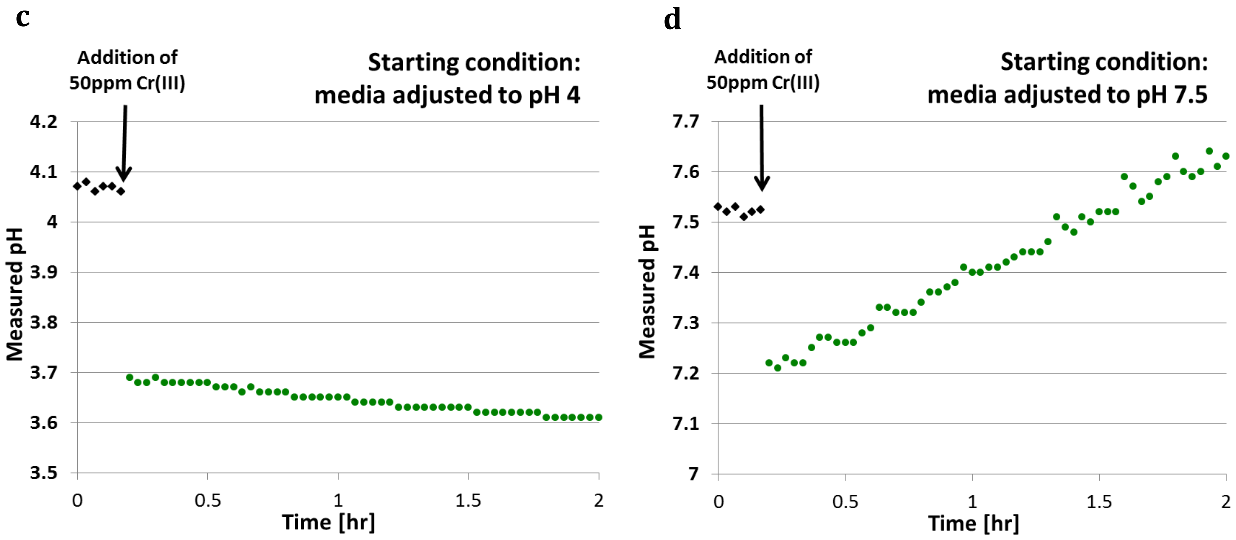

Figure 5.2: [a] FAAS results showing the concentration of Cr in the supernatant of DMEM incubated with 50ppm Cr(III) for 1 hour at various initial pH conditions. [b] The table shows the pH measured immediately before and after adding Cr(III), a decrease in pH is noted. For reference the initial pH condition is rounded. pH was measured over time for RPMI-1640 adjusted to starting conditions of [c] pH 4 and [d] pH 7.5. After addition of 50ppm Cr(III) pH decreased, before increasing for a starting condition of pH 7.5. Starting condition of pH 4 showed no increase in pH over time.

at 10,000rcf for 10mins in order to determine the presence of a pellet. As in figure 5.1b, no noticeable precipitate formed in RPMI-1640 with 50ppm Cr(III) after 4 hours for pH 4, while pH 7.5 did produce precipitate. This suggests that

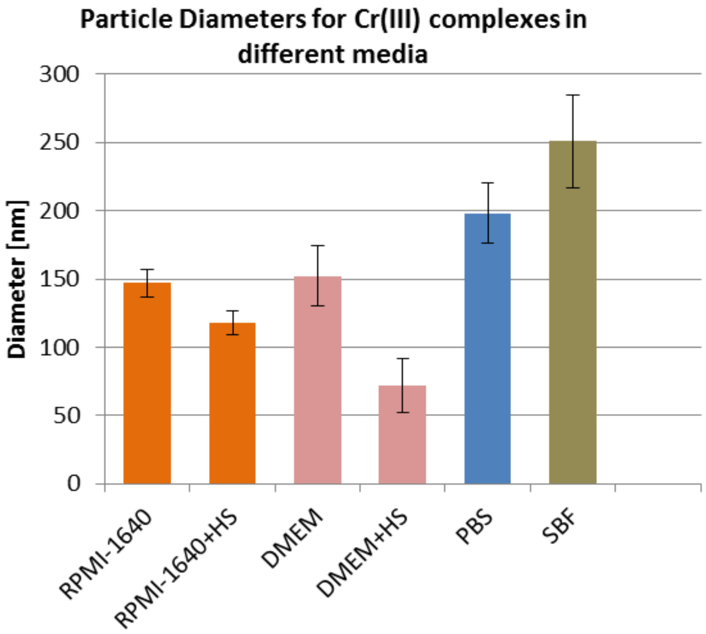

Figure 5.3: Size analysis performed on Fiji (based on ImageJ) to determine particle diameters observed in SEM images. For each sample, precipitation was formed in various environments: cell culture media (RPMI-1640 or DMEM) with or without human serum (HS), phosphate buffered saline (PBS) or simulated body fluid (SBF). The mean diameter and standard deviation from the mean are reported, n=100.

precipitation is accompanied by an increase in pH. As such, no increase in pH for an acid (pH 4) environment suggests that precipitation may not have initiated within 2 hours, rather than simply a lower yield. This suggests the pH of the local environment does contribute to the initiation of precipitation.

5.3.2. Observing the effect of media composition on Cr(III) precipitation

In order to visually observe the differences between the precipitates formed under various conditions SEM was utilised due to the resolution it could offer. SEM images in figure 5.4 show that, despite the media used, low concentrations of Cr(III) precipitate to form highly ordered structures with varying diameters. This is supported in figure 5.3, which shows the results of particle analysis on the SEM images.

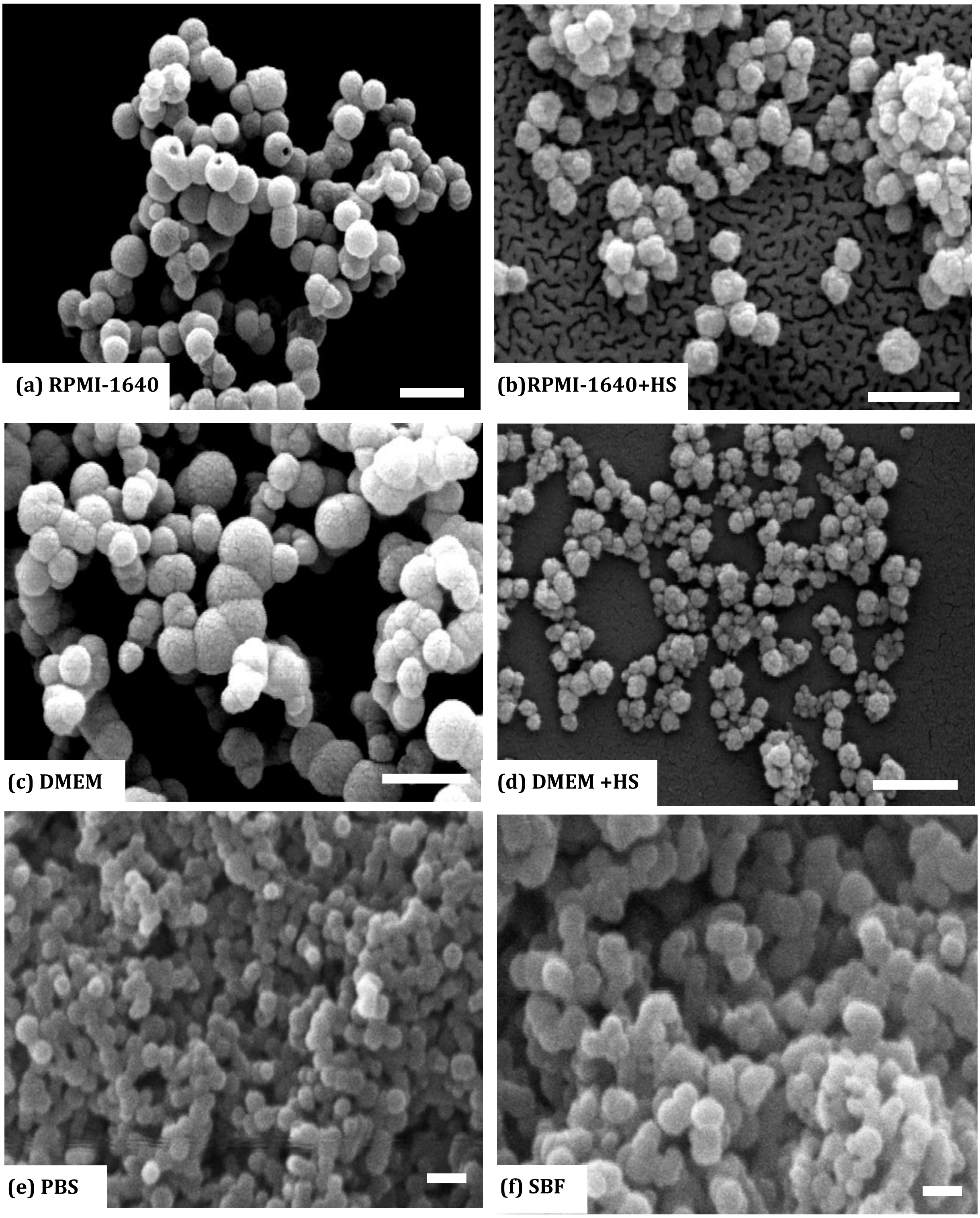

Figure 5.4: SEM images showing the Cr (III) complexes formed in different media (maintained at pH 7 for consistency) after 1hr. Media used were cell culture media (RPMI-1640 or DMEM) with or without human serum (HS), phosphate buffered saline (PBS) or simulated body fluid (SBF). Scale bar is 500nm for all images.

RPMI-1640 and DMEM with HS resulted in particles with a smaller diameter than RPMI-1640 and DMEM only, while PBS and SBF both resulted in larger diameter particles (>200nm). In addition, the precipitate surface for particles in the presence of HS is less smooth (observed in figure 5.4). This suggests that morphological properties of the Cr(III) precipitate are influenced by the composition of the local environment. As such, x-ray fluorescence (XRF) and x-ray absorbance near-edge spectroscopy (XANES) were used to investigate speciation of the Cr(III) complex in varying environments.

Due to time constraints at the synchrotron beamline, this interrogation of Cr(III) precipitate speciation focussed only on samples made in human synovial fluid and whether the presence of Co ions within the local environment had an impact on the speciation of Cr(III) precipitation. Samples consisted of a control (no metal ions added), CrHSF (Cr(III) only), Co:2.6CrHSF (Co(II):Cr(III) ratio of 1:2.6) and 2.6Co:CrHSF (Co(II):Cr(III) ratio of 2.6:1).

For the control, high centrifugation speeds were used in order to determine whether any CoCr degradation products were present after the initial HSF preparation method. Figure 5.5 shows the Cr-XRF elemental map for the control with the corresponding point-XANES measurement, taken at a containing a Cr signal (see arrow). The XANES spectrum is very noisy indicating weak signal, suggesting the Cr signal may have been produced by trace material left from initial HSF. As such, the HSF was determined to be relatively clear of Cr (after the initial prep); thus any further detection of Cr with a higher signal-to-noise would result from precipitation due to doping with Cr(III).

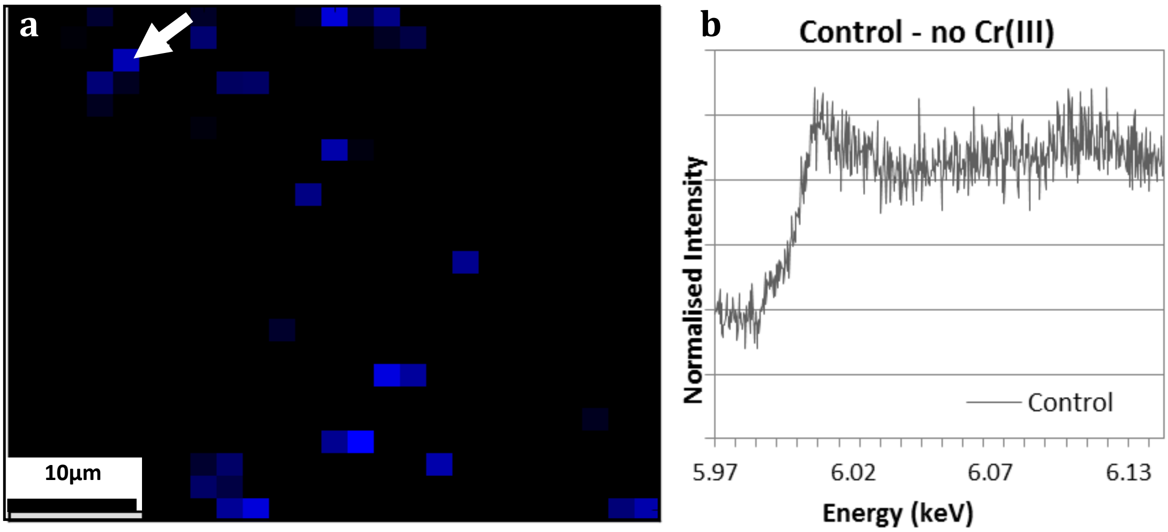

Figure 5.5: [a] XRF elemental map imaged at the Cr edge, 5.99keV of the control sample (human synovial fluid (HSF) with no Cr(III) doping). The arrow indicates the location of the single point Cr-XANES measurement shown in [b]. This Cr-XANES spectrum has a low signal-to-noise.

The elemental XRF maps for CrHSF and Co:2.6CrHSF samples, seen in figure 5.6a and 5.6b respectfully, show relatively homogeneous intensity distributions for Cr. Point XANES spectra were performed at random locations within the field of view (white arrows) to investigate Cr speciation of the precipitate. The Cr-XANES spectra for each sample gives rise to similar Cr spectra respectively, indicating no variation in the speciation of the Cr complex precipitated. However, between the two samples, in the post-peak region of the Cr edge, the first interference peak (for the Co-containing sample) is more resolved and the edge peak sharper (black arrow). This feature is reminiscent of Cr(III) phosphate ($CrPO_4$) (figure 5.7a), typically interpreted as the most abundant Cr(III) species present within tissues (68). This suggests that the presence of Co(II) ions in the local environment may alter the speciation of the Cr(III) precipitate.

Given the presence of a relatively small concentration of Co(II) (compared to Cr(III) concentration) resulted in sharpening of the post-edge peaks, the ratio of

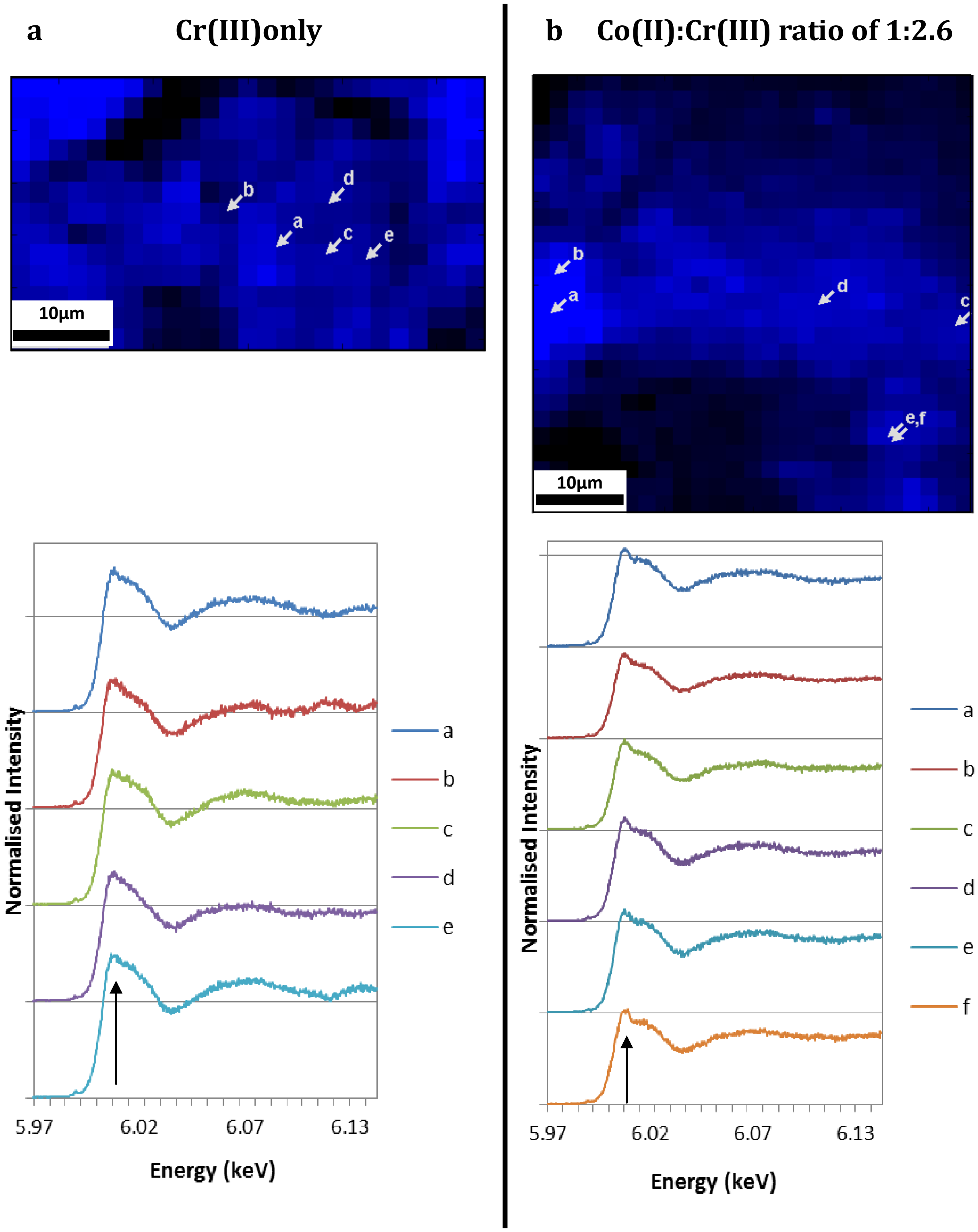

Figure 5.6: Elemental Cr-XRF maps at 5.99keV (Cr-edge) of precipitate formed in human synovial fluid doped with [a] 100ppm Cr(III) only and [b] 38ppmCo(II):100ppmCr(III). Below the XRF maps, the point XANES spectra are shown. Spectra correspond to the points in the XRF images indicated by the labelled arrows. The black arrows on the XANES spectra highlight the post-edge region, where the Cr-edge and first interference peak in [b] is more resolved.

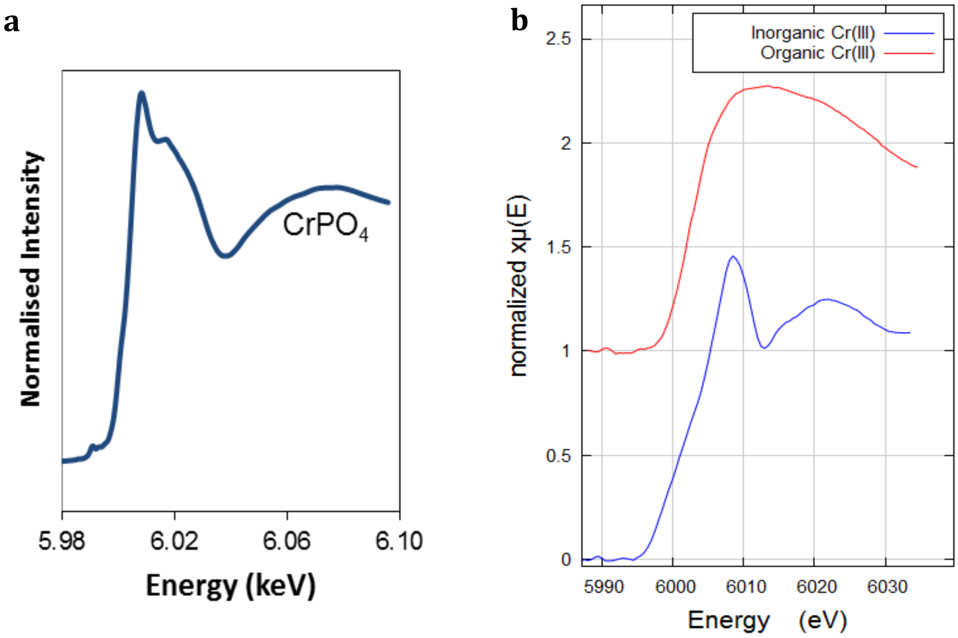

Figure 5.7: Cr(III) XANES references for [a] $CrPO_4$ standard obtained at Diamond Light Source and [b] reference spectra for inorganic and organic Cr(III) (181)

Co(II):Cr(III) was inverted to investigate higher concentrations of Co(II) in the local environment (figure 5.8). The Cr-XRF map (figure 5.8a) shows a heterogeneous intensity distribution, which suggests regions of higher and lower Cr concentrations. Thus a Co-XRF map was performed on the same region of interest (ROI). Increasing intensities of Cr do not correspond to increases in the Co intensities (figure 5.8b). This dissimilarity in the XRF intensities between the Co and Cr maps suggests that the precipitation produced is heterogeneous; otherwise the intensity changes would be mirrored in both Cr and Co maps. Rather than a consistent combination of Co and Cr, there are regions containing (referring to figure 5.8):

- Highest intensity Cr and no Co - seen at locations (a) and (b)
- Average intensity Cr and Co - seen at locations (c) – (f)
- Average intensity Cr and highest intensity Co - seen at locations (g) – (j)

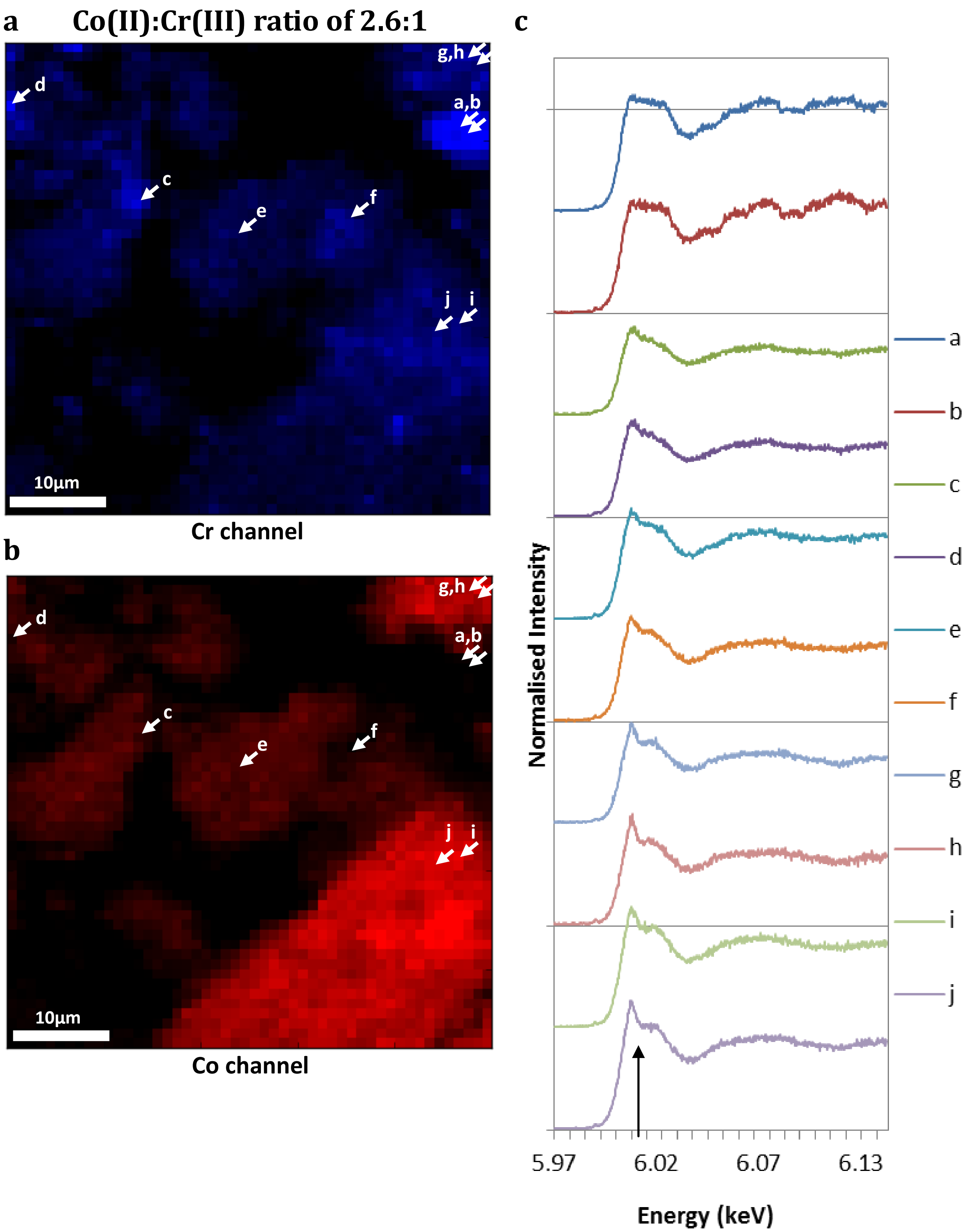

Figure 5.8: Elemental Cr-XRF maps of precipitate formed in human synovial fluid doped with 300ppmCo(II):118ppmCr(III). XRF maps acquired at [a] the Cr-edge, 5.99keV and [b] Co edge, 7.5keV. [c] Cr-XANES measurements are obtained from regions indicated by white arrows in the XRF maps. The black arrow indicates the post-edge region which becomes more resolved with increasing Co presence (from the Co-XRF).

In the areas of no apparent Co, (a) and (b), the Cr spectra match that of the spectra in the CrHSF sample (figure 5.6a). As the local Co XRF signal (which is proportional to concentration) increases, (c) to (f), the post-peak of the Cr edge becomes sharper and more resolved. This matches the Cr spectra of the Co:2.6CrHSF sample (figure 5.6b) and is reminiscent of $CrPO_4$ (figure 5.7a). In the highest intensity regions of Co-XRF signal, (g) to (j), the post-edge region shows a distinctive double peak. In terms of geometrical arrangement, as the local Co-XRF intensity increases, spectra (c) to (j), the same octahedral Cr(III) oxidation state is observed. However, this data suggests an evolution from an organic complex to a more inorganic complex, references for which are seen in figure 5.6b. This suggests that the local concentrations of Co will alter the speciation of the Cr(III) precipitate, and is further evidence to indicate local composition influences properties of the Cr(III) complexes.

5.4. Discussion

Previous work has shown the propensity for Cr(III) complexes to readily form within an hour in cell culture media (85, 93, 94). It was determined that organic proteins were present within the complexes, if available within the local environment during precipitation. However no further research into factors effecting Cr(III) precipitation has since been performed. Thus the experiments performed in this chapter were designed to investigate the effect of media composition and pH on Cr(III) precipitation.

Literature (12) implies that a lower pH, such as the pH found around the taper joint, results in and increased release of Cr (III) ions. However, figure 5.2

shows that a higher pH results in larger pellets of precipitation (figure 5.2b) and a decreased Cr content remaining in the supernatant after precipitation (figure 5.2a). In addition it is shown that in pH 4 media, precipitation does not appear to initiate as the pH over time does not steadily increase, as observed in pH 7.5 when precipitation forms (figures 5.2c and 5.2d). Therefore the conclusion that is drawn in literature (12), that more ions are released from CoCr particles at a pH 4 compared to pH 7.5, cannot be stated without determining whether increased ion level is due to more ion release at pH 4, or simply due to ions precipitating more readily at pH 7.5. Instead it can only be concluded that more Cr is left in ionic form at lower pH which is then detected by the ion measurement techniques used. It is important that this is highlighted as it changes the conceptual ideas of the processes occurring at sites around the implant. While a lower pH may result in an increase in ionic Cr due to dissolution processes, these Cr ions are then likely to remain as free ions until they have diffused to a region with a higher local pH, where the ions will readily take part in chemical processes resulting in precipitation.

In addition to pH, the composition of the local environment was also investigated for its impact on the precipitation of Cr(III) ions. In order to expand upon the media investigated previously (85, 93), various solutions were used, with and without the presence of HS (5% vol. in line with percentage of FBS used by Tkaczyk et al.). The diameters of all Cr-complexes formed in different mediums varied, with smaller diameter resulting from the presence of HS. In addition, the surface of these particles varied in apparent roughness. This suggests that morphological properties of the Cr(III) precipitate are influenced by the composition of the local environment. This diversity shows that the properties of the complexes formed are highly dependent upon the composition of the local environment. Consequently, these *in vitro* environments are inadequate to accurately determine the complexes that form *in vivo*, despite best efforts to create a simulated physiologically relevant media. As such, while the findings from Tkaczyk et al. (93, 94), regarding which proteins were bound to Cr(III) complexes produced in RPMI-1640 with FBS and HS is valid, its relevance to the matter of Cr ions within the body is questioned if the composition of the local environment can result in such variability. As such, the investigation into the speciation of Cr(III) complexes was only performed on HSF, given its greater biological relevance and a lack of beam time allocated for such an investigation.

XRF and XANES are classed as non-destructive techniques, used to determine the elemental composition of samples. Similar to normal fluorescence microscopy, XRF produces an image of where the element of interest is located. XANES however, allows us to interpret the speciation of that element by measuring the photo-absorption cross section for electron transitions between core and final states of an element, which are influenced by neighbouring atoms.

It was shown that as the local XRF intensity of Co increased (which is proportional to concentration), the edge and post-edge regions become more resolved and sharper, until a distinctive double peak is observed. This feature is reminiscent of Cr(III) phosphate ($CrPO_4$) (standard in figure 5.a), typically interpreted as the most abundant Cr(III) species present within tissues (68). This indicates a potential change in the configuration of the Cr complexes that contribute to the XANES signal (145).

Such a change may be related to inorganic Cr(III) vs. organic Cr(III) (see XANES references in 5.7b). Simply, if the concept of organic and inorganic Cr(III) species are considered - which is an oversimplification for the range of species (both organic and inorganic) that are likely to be encountered - inorganic Cr(III) species (indeed many inorganic transition metal complexes) have a tendency to have a higher scattering potential (181). This leads to the double feature in the post-edge region. In contrast, a more broad and featureless Cr K-edge is more reflective of an organic Cr(III) species, as seen in regions with no apparent Co signal, in either the CrHSF sample or Co-free regions of the 2.6Co:CrHSF sample. Consequently, this data suggests that the presence of Co(II) within the local environment causes the Cr(III) precipitation to evolve from an organic complex to a more inorganic complex. As the double peaks are not completely resolved one can conclude that there may be a combination of organic and inorganic Cr(III) present within the beam footprint.

Further interrogation of the samples by methods such as EXAFS, in combination with obtaining a greater range of standards, may provide better insight into the co-ordination of the complexes. Despite this, it can be concluded that there is different chemistry is occurring dependent upon the amount of Co present locally during Cr precipitation. This work suggests there is a level of nuance in the chemistry that was previously undiscovered by Tkaczyk et al. (93, 94).

5.5. Conclusion

A primary factor that determines whether the precipitation of Cr(III) ions occurs appears to be pH, whereas the composition of the local environment is what determines properties such as morphology and speciation. This impacts the conceptual understanding of implant derived debris as the concept of precipitation processes are widely overlooked, and could influence many studies.

This work has shown that despite where metal ions may be released, Cr(III) readily precipitates within an hour if the pH is above 5. Considering pH varies significantly between peri-implant sites (i.e. at a corrosion site where the local pH <3) (177, 178), and the wider environment, this suggests that the Cr level detected within a supernatant is dependent upon where a sample is taken. For example, after the release of Cr ions, once they have migrated away from the corrosion site, the pH will be typically higher, and thus precipitation will readily occur. Therefore, it is reasonable to conclude that by the time ion levels are measured in peripheral fluids (such as blood and urine levels) (87) much of the initial ion concentration released will not be detected. Especially considering metal ion release = ions detected in solution + precipitated content which is typically not measured. While this in no way discounts studies reporting high blood ion levels found in patients that required revision surgeries, or those which suggest acceptable upper limits for CoCr levels in peripheral fluids (83); the results presented here suggest that that ion quantification measured in peripheral fluids cannot address the complexity and individuality of the physical-chemical environment which will be driving adverse biological outcomes.

The vast majority of research in this area currently focusses on innate immune cell responses to metallic debris and soluble ions. However what is becoming abundantly clear is that there is a vast array of metal complexes generated at the time of release from the implant or generated later, following further processing within surrounding tissues (see chapter 6). These overlooked Cr-complexes represent an additional classification of metal degradation products, beyond just metal/metal oxide particles and metal ions, which are being exposed to the cellular environment and have the potential to interact. Given the chemical and physical properties of these complexes are dependent upon the local environment, which varies between sites within the body and patients (e.g. pH, composition, presence of biological molecules), commercial products are incapable of modelling the complexity of Cr(III) precipitates generated *in vivo*.

Further work is needed to characterise these Cr-complexes, such as determining whether pH and Co influences the morphology of the precipitate and examining the organic variability of these complexes (i.e. which proteins and organic acids are present). Understanding the chemistry and organic components of available degradation products is crucial to understanding potential cellular responses and may be highly significant in determining an individual's biological response. The effect of this additional class of degradation products can also be evaluated on 2D cellular systems for comparison to existing metal particle and ion studies.

Chapter 6

Multiscale Mapping of Metal Particles in Tissue Presenting an Approach

Contributions: *All work in this chapter was designed and written-up by the author Hayley Floyd (H.F.). Experimental work was performed in joint collaboration with Alexander Morrell (A.M.), a fellow PhD student from Aston University under the supervision of Prof. Owen Addison. Collection of beamline data was acquired by H.F. and A.M. for DLS and SLS, and by H.F. solely for ESRF. Analysis of raw beamline data on MANTiS (PCA and cluster analysis) was performed jointly by H.F. and A.M. (A.M. primarily responsible for writing Python scripts). All other analysis was performed by H.F. solely.*

6.1. Introduction

There has been interest in the biological reactions associated with metallic implant debris since the early 1990s when the "debris disease" was first described (182) and linked to peri-prosthetic bone loss observed decades earlier (183). While it is understood that 75% of implant failures are characterised by aseptic loosening and osteolysis (101); the underlying biological responses will be strongly dictated by local cellular interactions, which can be influenced by the physical and chemical properties of implant derived debris.

Metal degradation products are typically reported as particulate (2, 58, 60) or ionic (79, 80). Debris properties, such as size, composition and local concentration, are primarily influenced by implant type, the underlying mechanism of their production and the local environment (2). For example the dynamic nature of biomolecules adsorbing to nanoparticles can result in complex molecules which vary depending on their immediate surroundings (184). Furthermore, metal ions, produced through corrosion and dissolution processes, can precipitate to form complexes which are highly influenced by the pH and composition of the local environment (chapter 5). Studies have shown that cellular interactions and therefore subsequent inflammatory responses can vary depending on these inherent debris properties (2, 101, 105, 185, 186). As such investigating the chemistry of metallic debris in surrounding tissues may aid in further understanding why such a range of patient reactions are observed.

X-ray fluorescence spectroscopy (XRF) and X-ray absorbance near edge spectroscopy (XANES) can be employed to identify low concentration implant elements in tissues, whilst giving insight into metallic chemistry (142, 143). Synchrotron radiation sources are advantageous for these studies as the high flux allows the interrogation of ultra-dilute systems (141). Conventional XANES methods performed in the literature (75, 77) interrogate the absorption coefficients of a single element by scanning through selected energies at a single point. This reveals information regarding coordination and chemical speciation. However, samples containing multiple species can be problematic as the spectra produced is a weighted sum all the species within the cross-section of the beam. Higher resolution beams are typically used in order to increase the likelihood of observing a single chemical species within a heterogeneous sample. However in soft-tissues, this often results in a low signal-to-noise due to subtle movements of the source and/or tissue. This is a significant problem in many x-ray absorption spectroscopy studies, where the beam size approximates the size of the interrogated feature.

Previous studies interrogating *ex vivo* tissue from patients using spectroscopic methods have documented a range of different Cr(III) complexes found in tissues adjacent to metallic implants. Ektessabi et al. (75) reported a K-edge shift in Cr XANES measurements, indicating a partial oxidation of chromium. However the quality of their data suffered due to the large beam width (10μm). Hart et al. (77) improved upon the beam resolution used with a 4μm beam for XANES measurements on a variety of points and reported that a hydrated chromium phosphate complex was the most abundant chromium species present. However it is impossible to gain full chemical speciation insight when only interrogating a set number of user defined points. These studies used, at best, micron sized resolution measurements to interrogate the samples. Given resolution is limited by the width of the measurement probe (x-ray or light); this means that typically only the bulk composition of the debris is reported.

The understanding of Cr(III) speciation within *ex vivo* tissues at a sub-micron scale is limited and only one paper (92) has been published employing this approach for the application of interrogating *ex vivo* tissue. To reduce the problems associated with XANES, a mapping approach, similar to what is presented in this chapter, was used. However the data was interpreted in the context of the individual spectra acquired and not their spatial variation. Neither this group, nor any other group, has published any follow-up to this communication paper and as such it is felt that this paper failed to highlight both the novelty and potential significance of a XANES mapping approach to interrogating nano-scale metal debris.

To date there has been limited speciation identification of implant debris at sub-micron scales; as such this chapter presents a multi-scale approach to identify the spatial speciation in *ex vivo* tissues that once surrounded metallic implants. This first part of this chapter aims to determine whether conventional single point, micron-beam techniques accurately portray the speciation of wear debris. As single point spectra are more commonly used, there is no standard way to analyse the large quantity of spectra acquired during a XANES mapping approach. Therefore, the second half of this chapter suggests methods of analysis for interpreting the large data acquired by XANES mapping, and discusses limitations.

As this chapter is primarily presenting an approach, the XRF and XANES results are used as evidence to discuss the validity of the approach and the analysis methods. Thus the results and discussion are presented together for clarity.

6.2. Methodology

6.2.1. Preparation of Tissue

Ethics were granted by the Human Biomaterials Resource Centre (HBRC) at Birmingham – a Human Tissue Authority licenced biorepository - (ethical approval REC 09/H1010/75) for tissue collection. It covered the acquisition of fresh frozen peri-prosthetic tissue samples, taken from locations adjacent to the implant site, following scheduled revision surgery of failing metal hip prosthesis. Locations requested consisted of synovial membrane and tissue adjacent to the taper joint, as it was predicted these regions may contain larger concentrations of metal debris, due to the proximity to an articulating surface or a corrosion site respectively. Tissues were orientated, immediately placed on dry ice in theatre and transported to the HBRC before collection and storage at -80^{o}C at a HBRC approved site at the University of Birmingham.

From the tissue provided, a piece from the synovial membrane was chosen. The frozen tissue was sectioned into 1cm^3 blocks, such that the exposed face for imaging exposed the tissue layers present within the synovial membrane as one moves radially away from the implant. The tissue 'block' was embedded in Optimum Temperature Cutting (OCT) compound before sectioning. Cryosections between 4-8µm in thickness were prepared using a cryotome, at -20^{o}C, using a tungsten carbide blade. Sections were then mounted onto either silicon nitride membranes (Silson, Ltd) or Ultralene (SPEX®SamplePrep). 'Adjacent' sections were acquired to allow for complimentary histological staining and spectroscopy imaging. Samples for spectroscopic imaging were air dried and stored in falcon tubes before imaging.

6.2.2. Diamond Light Source

Tissue samples were initially interrogated at the Diamond Light Source (DLS) (Harwell Science and Innovation Campus, UK) using the micro-focus spectroscopy beamline, I18, which uses Kirkpatrick-Baez mirrors to focus the beam. This allows for a micron-sized beam to be produced. The beam is cycled through the required energies using a liquid nitrogen cooled Si(111) monochromator.

Samples imaged at Diamond were mounted on Ultralene and placed in beamline specific sample holders at 45° to the incident source. The beam was then focused, by a beamline scientist, to produce a 3μm beam (beam with a footprint of 3x3μm). Parameters used included an acquisition time of 0.2s/pixel, and a horizontal and vertical (x-y) step size of 3μm. All data was acquired at atmospheric pressure.

XRF maps were acquired using an incident energy of 8.5keV. As this is above the Co excitation energy, Co, Cr and all elements below this down to chlorine can be detected. Single point XANES measurements of dilute elements in organic matrices, using a nano and small micron sized beams, can be complicated by relative movements between the beam and point of interest either due to movement of the feature within the sample (x-ray damage of the matrix) or, due to beam movement (monochromator induced). To overcome these issues, a newly established technique of XANES mapping was deployed.

XANES maps were generated by acquiring XRF images at a range of energies below and above the excitation energy of Cr for a single region of interest. A total of 91 sequential energy points were chosen. Using the notation [starting energy (eV), finishing energy (eV), energy resolution (eV)], the range of energies used were - [5940, 5982, 6], [5988, 6009, 0.5], [6010, 6034, 1.2], [6033, 6263, 10]. These individual maps were windowed for Cr Kα fluorescence (±200eV) and then arranged to produce a 3D 'stack' where z represented the Cr-Kα spectra for a single pixel in x-y. The data was aligned and normalised prior to analysis with standard in-house methods at the beamline.

6.2.3. Swiss Light Source

Micron-sized XRF was also performed on the Swiss Light Source (SLS) at the Paul Scherrer Institute (Zurich, Switzerland) on the microXAS beamline (X05LA). X05LA provides a broad energy range to allow excitation of the Mo edge and enabled correlation of Co,Cr and Mo fluorescence signals. X-rays are provided via an in-vacuum undulator which then passes through pairs of slits, a monochromator, and Kirkpatrick-Baez mirrors; all designed to collimate, filter and focus the beam respectfully.

Samples, sourced from the same 'tissue block' as the samples used at Diamond, were sectioned and again mounted on Ultralene. They were then imaged at 8.5keV to acquire Co and Cr XRF maps. As this beamline is able to reach the higher energies required to detect molybdenum (Mo), present in most Co-alloy hip implants, Mo XRF maps were also acquired following Co-Cr XRF maps. Regions of high intensity Co and Cr regions were chosen to observe any correlation with Mo. Mo XRF maps. Were acquired using a beamline energy of 20.05keV.

6.2.4. European Synchrotron Radiation Facility

For sample interrogation at sub-micron resolutions, neighbouring tissue samples to those imaged at Diamond and Swiss Light Source were mounted on silicon nitride membranes and taken to the ID21 at the European Synchrotron Radiation Facility (Grenoble, France) (ESRF). ID21 uses a fixed exit double crystal Si(111) monochromator. The beam was focused to a footprint of 600x600nm using a Fresnel zone plate. To acquire measurements energy dispersive detectors (7 element, high purity germanium detector and a silicon drift diode) were used.

Two incident energies were used to acquire XRF maps: 7.8keV used to detect Co and Cr, and 6keV, on the same regions, to detect low Z-elements found in tissues. This energy was chosen as it would still detect Cr allowing for any correction to be made for geometric shifts as a result of monochromator movement.

To produce XANES maps a total of 117 sequential energy points were chosen. Using notation [starting energy (eV), finishing energy (eV), energy resolution (eV)], these energies were: ([5970, 5985, 5], [5985.5, 6030, 0.5], [6033, 6099, 3]. Using ESRF in-house scripts (based of SIFT linear stack alignment), these individual maps were stacked, aligned (accounting for sample and/or beam movement), windowed for Cr Kα fluorescence (±200eV) and normalised prior to analysis.

6.2.5. Histological Staining

Neighbouring tissue slices to those imaged at Diamond were sectioned at the same time and mounted on Suprafrost slides for later histological staining. Standard H&E (haematoxylin and eosin) staining was used to provide tissue contrast for light microscopy imaging. Haematoxylin appears dark blue/violet and binds to negatively charged substances such as DNA/RNA in nuclei. Eosin is a red/pink stain that binds to positively charged substances such as amino acids/proteins in the cytoplasm and extracellular fibres (i.e. collagen).

For H&E staining the tissue must be flat on the Suprafrost slides. Either a drop method or a batch dipping method may be used. For these samples dipping was used as samples appeared thin enough to maintain adhesion (due to static) to the glass. Samples were first fixed using 4% paraformaldehyde (PFA) (SigmaAldrich, UK), then washed with deionised water (dH_20) twice. Following fixation they were stained with 0.1% mayer's haematoxylin (SigmaAldrich, UK) for 10minutes then rinsed in dH_20 for 3minutes. 0.5% Eosin (SigmaAldrich, UK) was then added for 2 minutes followed by quick dips in dH_20 then in concentrations of 50%, 70%, 95% and finally 100% ethabol. Samples were then washed with xylene and a coverslip was mounted using DPX mountant (SigmaAldrich, UK) and left to cure overnight.

Imaging was performed using a benchtop light microscope with a motorised stage that permitted automatic mosaic imaging. A large section (~$1cm^2$) of tissue was imaged at a high magnification by sequentially imaging smaller regions and stitching them together. Imaging was performed at a variety of magnifications using standard brightfield and reflection mode on an in-house modified Zeiss microscope at the Diamond Light Source.

6.2.6. XRF Analysis

6.2.6.1 Producing XRF Maps

To produce XRF maps the data was batch fitted using PyMca 5.0.0 (Copyright ESRF). This involves background subtraction on a pixel by pixel basis, and fluorescent peak fitting/identifying. Batch fitting and calibration files depend on the specific instrument set up (incident energy, object to detector distances etc.) being used for each x-ray measurement at a specific light source. A PyMca .cfg configuration file was generated for each set of measurements taking into account the instrumental variation at each site. Parameters include x-ray beam energy, element peaks to include in the model and anything along the experimental set up between the sample and detector that can attenuate the beam. Once fitted, the fluorescent maps were generated as RGB images to allow clear visual representation of the elemental distribution within the tissue.

6.2.6.2 Correlation of Co and Cr with Mo signals

To confirm whether high CoCr intensity regions in the XRF maps are metal particles Co and Cr XRF maps were correlated with molybdenum (Mo) XRF maps. Two regions of high CoCr intensity were selected for Co and Cr XRF mapping at the Swiss Light Source (SLS). After mapping, the energy of the beam was shifted up to 20.02keV to map the same locations for Mo.

After acquisition the XRF data was loaded into MatLab R2011a for processing. The intensity values for the Mo maps were then plotted against the intensity of the corresponding pixel for the Co and Cr maps separately. If all the points (for Mo vs. Co and Mo vs. Cr) align linearly this indicates correlation between the three metals.

6.2.7. XANES Analysis

6.2.7.1 Metallic Contribution

To determine the contribution of metallic Cr vs. Cr(III) from other species, linear combination fitting (LCF) was performed on selected spectra at radial locations from the centre of a feature. Starting from a high fluorescence intensity centre which becomes region 1, the pixels immediately surrounding this becomes region 2, and so on. These regions are referred to as the radial selections, or selections moving radially outwards.

During LCF, the range at which the LCF algorithm operates was reduced to just the pre-peak and edge only, as the first interference peak (post peak) experiences multiple scattering events which makes fitting more difficult. Reference spectra were acquired from a beamline in-house database, from investigation using the same experimental set-up. References obtained consisted of metal-CoCr and chromium hydroxide ($Cr(OH)_3$), chromium oxide (Cr_2O_3) and chromium phosphate ($CrPO_4$). The results were then plotted as metallic Cr fraction and Cr(III) fraction.

6.2.7.2 Principal Component Analysis and Clustering

Principle components analysis (PCA) and cluster analysis was performed on the XANES data due to the large number of spectra acquired through the mapping approach. Both techniques were performed using MANTiS (Multivariate Analysis

Tool for Spectromicroscopy) (187). Prior to analysis each spectrum was first normalised by dividing the whole spectrum by the intensity of the last energy point using ATHENA (part of Demeter System 0.9.25 by Bruce Ravel, National Institute of Standards and Technology). This eliminates principal components (PCs) being generated based on intensity rather than spectral differences. PCA is typically used to reduce dimensionality by determining the minimum number of components that can be used to describe a system. In theory the number of principle components (PCs) would match the number of species observed.

The spectra were then clustered using k-means clustering, with the determined number of PCs as the variable (number of clusters). This method groups the spectra based on their spectral similarity into X number of groups (X = N# PCs). The spectra within each group were then averaged together to produce a reduced number of spectra, which should describe the whole ROI. These were then compared with Cr(III) standard spectra.

6.2.7.3 Linear Combination Fitting

Linear combination fitting (LCF) was performed again in ATHENA on normalised spectra. LCF was used for two purposes, to determine the metallic Cr contribution on radial selections (previously described in 6.2.7.1), and to determine the best combination of standards that fit to the experimental data after PCA and clustering.

Despite the combination of standards used, all LCF had a set of common parameters. First, all weights were forced to sum to 1 and must be between 0 and 1; this ensures a realistic fit. In addition, the edge position was not allowed to change, i.e. spectra could not shift in x-direction (energy); this was fixed because instrument calibration against standard spectra was always performed prior to experimental data acquisition. Finally, the range of the spectra used for fitting was modified depending on the purpose. For determining metallic contribution, the fitting region was reduced to the pre-edge and edge peaks only; as the pre-peak is a main discriminator between metallic and Cr(III) species. For the fitting of clustered data, the fitting region was extended to encompass the whole spectra as typically it is the post-peak region in XANES spectra that is the main discriminator between different Cr(III) species.

6.2.7.4 ESRF Data Binning

For validation of the sub-micron measurement approach the 600nm resolution XANES data was binned to represent a larger beam footprint simulating a measurement with a relaxed lateral resolution. To represent a 3µm beam, a 5x5pixel region (5*600nm x 5*600nm) was selected and the spectra averaged. Consideration was made to select regions that included high intensity pixels to mimic the location choice for single point XANES measurements taken previously at DLS.

6.3. Results and Discussion

6.3.1. Histological Staining

Figure 6.1: Main tissue block - primary source for tissue slices for beamline interrogation. Sample originated close to the acetabular cup, arrows indicate the edge closest to the implant. Due to sample storage the tissue folded back on itself.

Figure 6.1 shows the 'main tissue block' acquired from the ROH, from which all subsequent tissue sections interrogated were sourced. The tissue originated from the synovial membrane, close to the acetabular cup. The arrows indicate the edge closest to the implant, and discolouration in the tissue layers can be seen (green colour). Standard brightfield images were obtained in mosaic mode using automated stitching (figure 6.2a). Aggregation of black particles can be seen following the tissue boundary closest to the implant. Reflection microscopy was then used as metal particles are highly scattering (figure 6.1b). This provides an imaging modality that is sensitive to the presence of metallic particles within soft tissues.

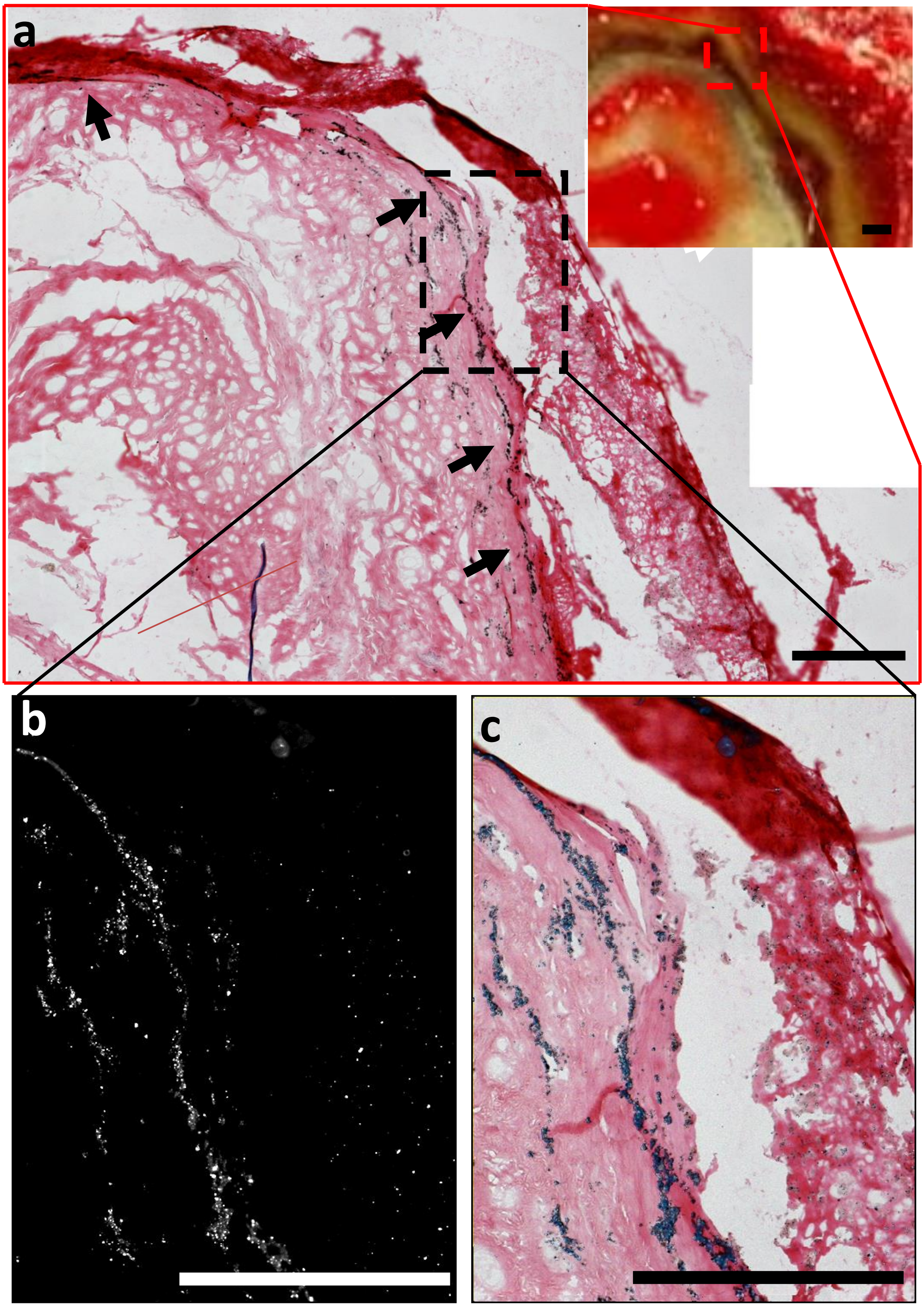

Figure 6.2: [a] Brightfield image of H&E stained tissue slices adjacent to beamline interrogated samples. Arrows indicate metal particles aggregating along tissue boundaries. [b] Reflection mode image highlights the metal debris within the tissue. [c] Overlay of reflection (blue) and brightfield modes. Scale bar = 100µm

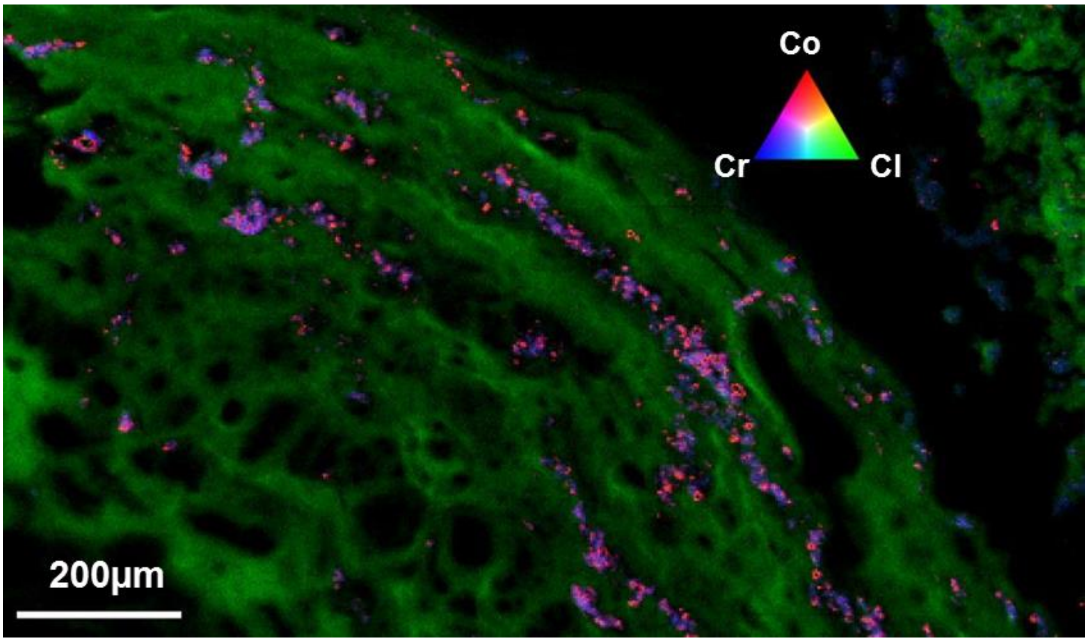

Figure 6.3: XRF image of *ex vivo* synovial sheath using a 3µm beam at Diamond Light Source. Cobalt, chromium and chlorine (Cl was used as a tissue marker to observe tissue geometry) are represented by the red, blue and green channels respectively.

The histological staining shows the preference for metal debris to aggregate along the tissue boundaries within the synovial membrane. It is along these boundaries that XRF and XANES mapping was performed, in order to maximise the chance of finding a CoCr signal within a reduced region of interest.

6.3.2. Spectroscopic Mapping Approach

6.3.2.1 Micron-Scale Mapping

Previous approaches using XRF/XAS to interrogate *ex vivo* tissues have predominantly used micron-scale beams (ranging between 3 and 10um in focus) (75-77) to produce XRF maps showing elemental distribution, and used single point XANES (with an equivalent micron-sized beam foot-print) to determine speciation of wear debris across the tissue. To replicate these methods, and confirm similar

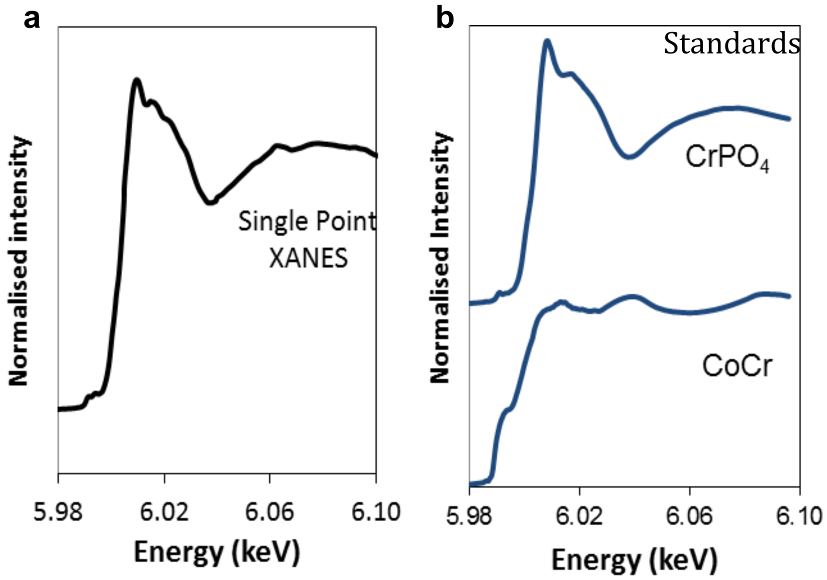

Figure 6.4: [a] Static single point XANES measurement, using a 3μm beam on a region with high Cr signal. [b]$CrPO_4$ and CoCr standards acquired using the same beam set-up.

results for the given tissue samples (seen in figures 6.1 & 6.2), a lateral resolution (beam width) of 3μm was used for initial measurements at DLS.

At this resolution, regions of interest of approximately $1mm^2$ were imaged using XRF (figure 6.3). These maps complimented histology findings by showing Co and Cr signals, represented by red and blue, accumulating along the tissue planes of the synovial sheath. Low-Z elements such as Cl (used here) are typically good markers of organic tissue and can used to show the underlying tissue architecture. Typically high intensity areas of co-located Co and Cr signals were seen surrounded by lower intensity, more diffuse Cr regions.

In accordance with previous methods (75-77), XRF mapping was used to inform locations for performing single point XANES measurements. The locations typically chosen had high intensity CoCr signals, as these tend to result in measurements with a higher signal-to-noise ratio, therefore maximising the chance of interpreting the data set. This introduces a selection bias which is infrequently reported in the literature.

The single point XANES spectra acquired demonstrate post-edge spectral features characteristic of chromium (III) phosphate ($CrPO_4$), using a standard examined on the same experimental set-up for comparison (figure 6.4). This supports the previous findings by Hart et al. (76, 77) who, using similar experimental techniques, interpreted that the most abundant species of Cr present was hydrated $CrPO_4$. Additionally, it was observed that the pre-edge peak appeared broader than that in the $CrPO_4$ standard, characteristic of metallic Cr (see CoCr standard in figure 6.4b). This suggests that the single point XANES spectrum is likely to be a combination of at least two distinct Cr species within the cross-section of the x-ray beam, indicating variability on a smaller scale.

Typically, multiple point XANES measurements would be sampled to confirm Cr species across the tissue; however, a XANES mapping approach (using a 3µm beam) was used instead. This reduced the bias in selecting single points and allowed for a more rigorous interrogation of spatial variability.

Figure 6.5a shows the XANES map after PCA and clustering (using MANTiS software). Cluster analysis involves grouping the spectra based on spectral similarity. In theory the number of PC/clusters would match the number of Cr species observed. The sum of the spectra in each cluster (shown in figure 6.5b) appears to follow the intensity of the metallic signal. The centre of the high intensity areas (red) contained a larger contribution of metallic Cr than the surrounding regions, evident by the broader pre-peak around 5.99keV (see arrow

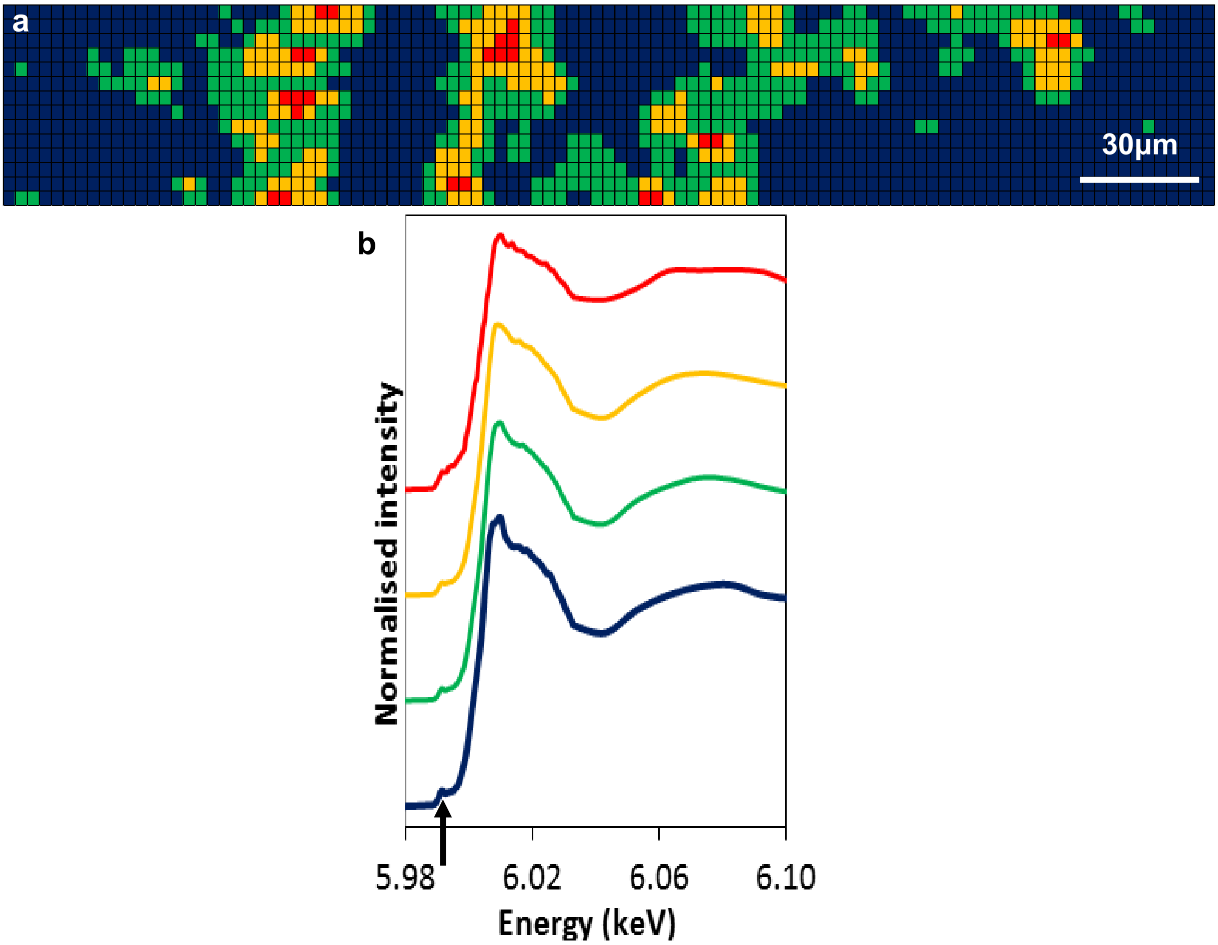

Figure 6.5: [a] XANES map (~300x45μm in size with a 3μm beam) showing the clusters generated through PCA analysis using software package *MANTiS* , the spectra in these clusters were summed to produce the spectra in [b]. The arrow shows the location of the pre-peak for Cr(III) species which can give an indication of metallic Cr content

in figure 6.4b). The surrounding regions showed the same spectral features as the point XANES measurements, characteristic of $CrPO_4$. The only difference between the [yellow, green and blue] spectra is the sharpness of the edge peak. It is likely this is due to changes in the contributions of various Cr species, as each spectrum (in figure 6.5b) is a summation of the pixels within a given cluster, and each pixel is a summation of all Cr species within the cross-section of the beam at that point.

This two phase observation of a distribution of high intensity regions of Co-Cr, typically characteristic of a metallic Cr suggesting wear particles, surrounded by a lower intensity Cr(III) complex, such as $CrPO_4$, has previously been reported (77). However, if studies continue to use only the standard approach of single point XANES, they risk simply repeating previous data and not addressing the concept of additional variation in speciation within the cross-section of a micron sized beam. This was the reasoning for moving towards a XANES mapping approach.

6.3.2.2 Sub-Micron Mapping

Elemental distributions within the tissue can be observed at higher resolutions using the ID21 beamline at ESRF. Subsequent XRF and XANES mapping was performed on tissue slices from the same 'tissue block' (approximately 1cm separation between slices) using 4μm and 600nm beam footprints. A total of 4 larger (4μm) XRF maps (figure 6.6a) were acquired, and were used to inform regions of interest for the 19 higher resolution 600nm maps (6.6b) acquired. From figure 6.6b while it is apparent that high intensity regions of co-located Co and Cr are still seen (pink regions), it is more evident at the submicron level that Cr is present in areas without the presence of a Co counterpart. As previously stated, this two phase observation has been seen before (77) and while this does not confirm speciation variability, it is indicative. This also links to the findings in the previous chapter, where lone regions of Cr precipitate were observed even when Co was added to the solution.

Following XRF mapping, 4 ROIs were selected to perform XANES mapping. To maximise the potential variability within a smaller ROI (limited at ~10x10μm due to mapping time), regions containing high Co-Cr signals were chosen, based

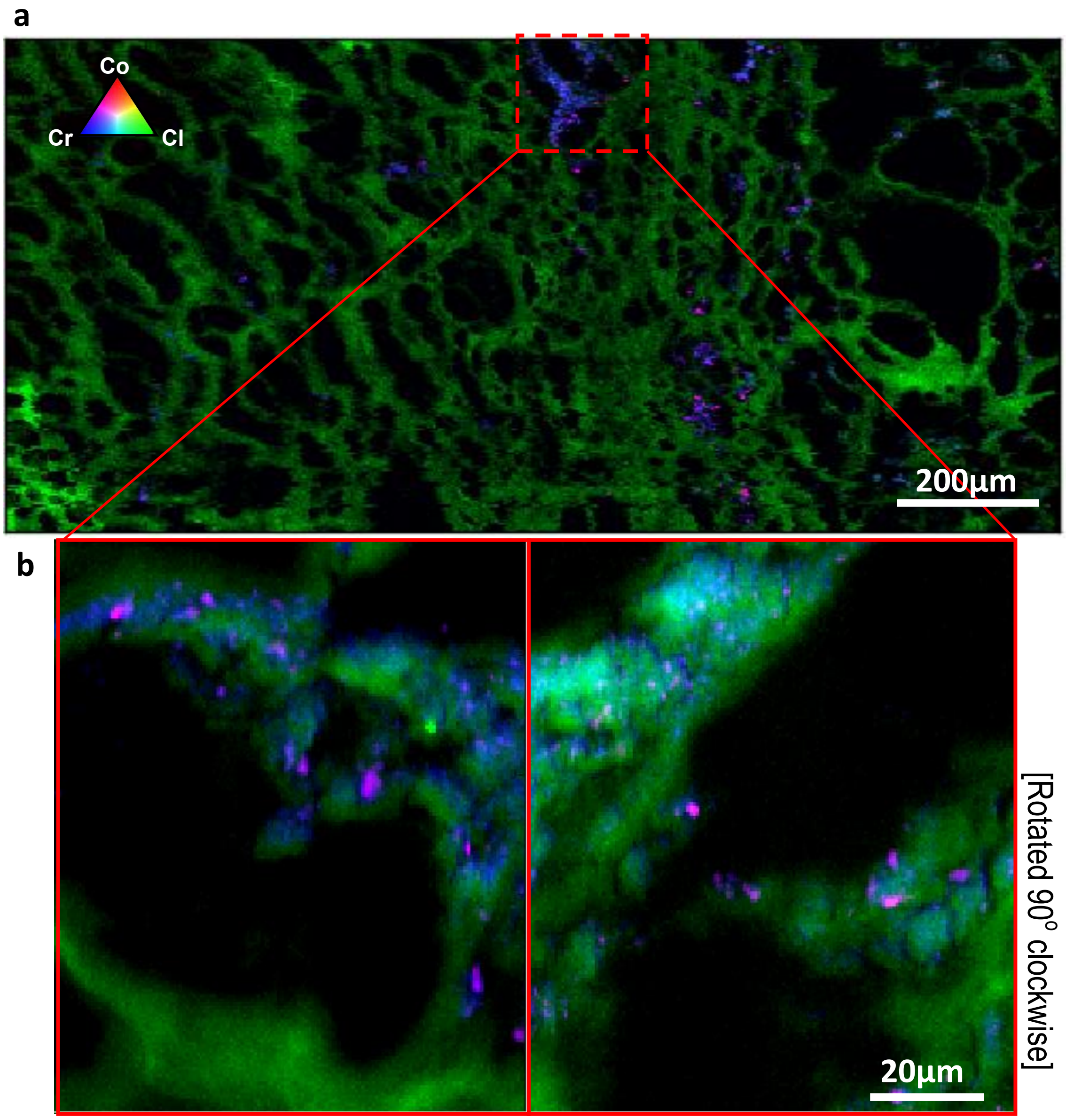

Figure 6.6: XRF images, performed at ESRF, using [a] 4µm beam followed by [b] 600nm beam on smaller ROI's. Co, Cr and Cl are represented by red, blue and green respectively, the latter acquired at a lower energy in [b] to improve signal-to-noise.

on the assumption that high intensity regions of Co-Cr are potentially indicative of wear particles representative of the bulk implant metal (figure 6.5). By centring on a wear particle the expectation was to interrogate speciation radially from a CoCr source within the tissue.

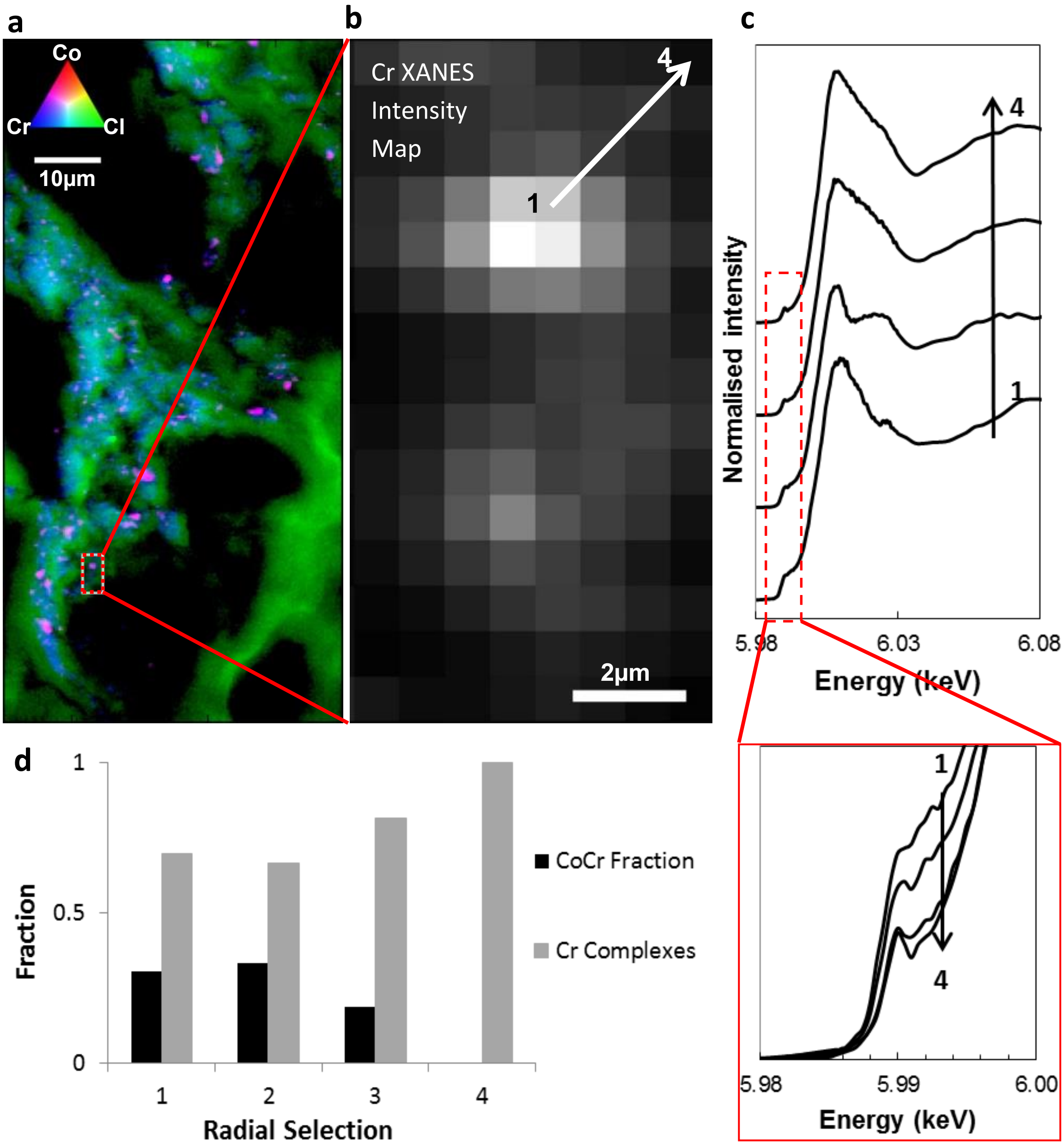

Figure 6.7: [a] XRF map used to select ROI for XANES mapping (both 600nm). [b] A XANES intensity map - each pixel is a Cr XANES spectrum. [c] Four averaged radial selections (see arrow) of the XANES spectra across the 'particle' - pre-edge range is magnified in in the inset. [d] Graph representing the contribution of Cr metallic fraction vs. other Cr species as determined by linear combination fitting using ATHENA. Metallic Cr contribution is seen to decrease moving radially outwards from the centre of a high intensity region of CoCr.

The Cr-XANES intensity map in figure 6.7b mirrors the Cr distribution in the XRF map. To generate an appreciation of how the chemical species changed across the wear particle, radial averages were taken, indicated by the arrow in figure 6.7b, moving outward from the 2x2pixel high intensity centre. For each

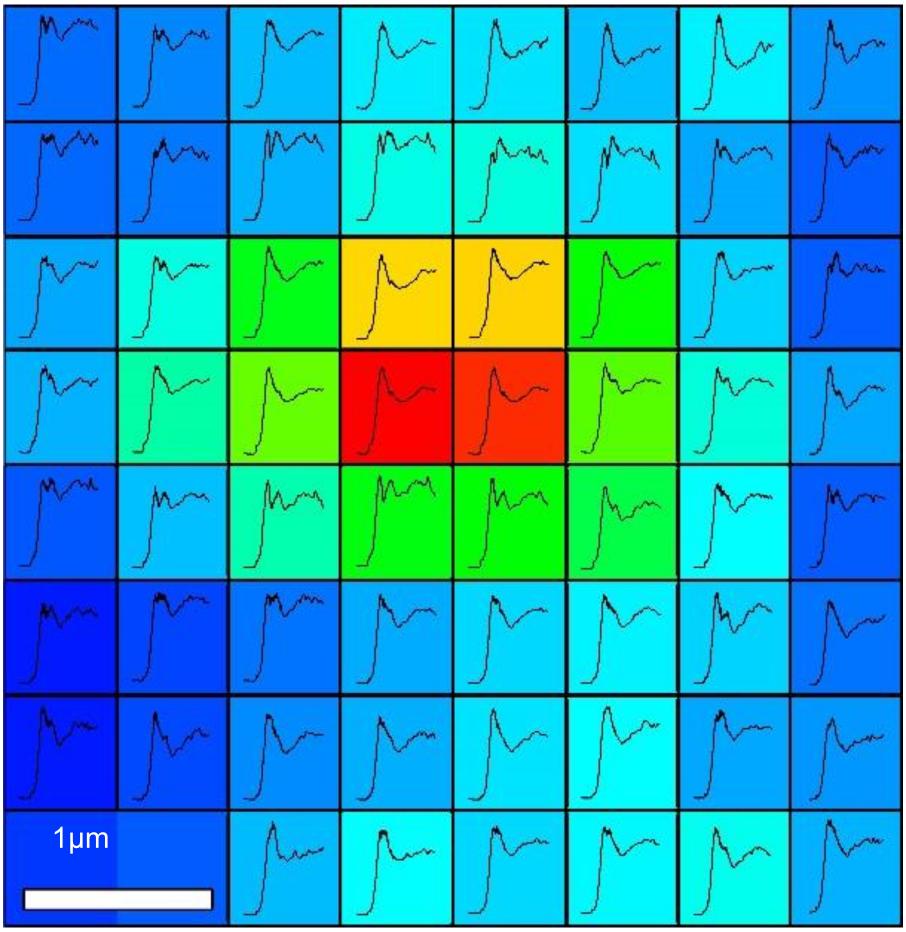

Figure 6.8: Cr-XANES intensity map with XANES spectra at each pixel overlaid. This illustrates the dissimilarity of the spectra moving radially outwards from the high intensity (red) centre. This suggests chemical variability on a submicron scale.

selection the spectra were averaged and the results are presented in figure 6.7c. A clear decrease in the pre-peak is observed moving outward from the high intensity centre, indicating a reduction in metallic fraction (see standards in figure 6.4). This was confirmed with linear combination fitting in ATHENA using a metal-CoCr and other Cr(III) species as standards. This supports the conclusion from DLS using a 3µm beam (figure 6.5). However, this method of analysis does not make allowances for dissimilar spectra within each radial selection – it must be considered that wear particles/aggregates are not guaranteed to be spherical. This is illustrated by figure 6.8 which shows an 8x8pixel excerpt from the XANES map in figure 6.7b with the XANES spectra overlaid. Radial selections outward from the high intensity centre (2x2pixel – red and yellow), contain dissimilar spectra in the post-edge region.

To identify which Cr(III) complexes were present, PCA analysis was conducted on the XANES map in figure 6.8. A similar approach was used for the data collected at I-18 at Diamond. Using MANTiS, four clusters were subsequently generated and grouped based on spectral similarities (figure 6.9).

LCF suggests that the most abundant cluster (cluster 1) is best represented as a combination of $CrPO_4$, $Cr(OH)_3$ and CoCr. The presence of these species are commonly reported within literature (77). Cluster 2 presents a difficult species to identify. A unique feature is observed at ~6025eV which is consistent in all spectra contributing to that cluster. This spectrum could not be explained from any of the organic Cr standards shown in figure 6.9. However, the broad, and mostly featureless, spectrum does compare to the organic Cr(III) spectrum in figure 5.6 and reflect the Cr-XANES spectra obtained for Cr-precipitation in the absence of Co ions (chapter 5). Clusters 3 and 4 are likely to be combinations of Cr complexes, with the highest fractions being species with similar geometry to Cr malate and Cr acetate hydroxide respectively.

Nonetheless, regardless of the species observed the spectral features of these clusters are significantly different from those seen with micron-beam XANES in figure 6.5. The lower resolution beam resulted in clusters with post-edge spectral features predominantly resembling $Cr(OH)_3$/$CrPO_4$ only, with the

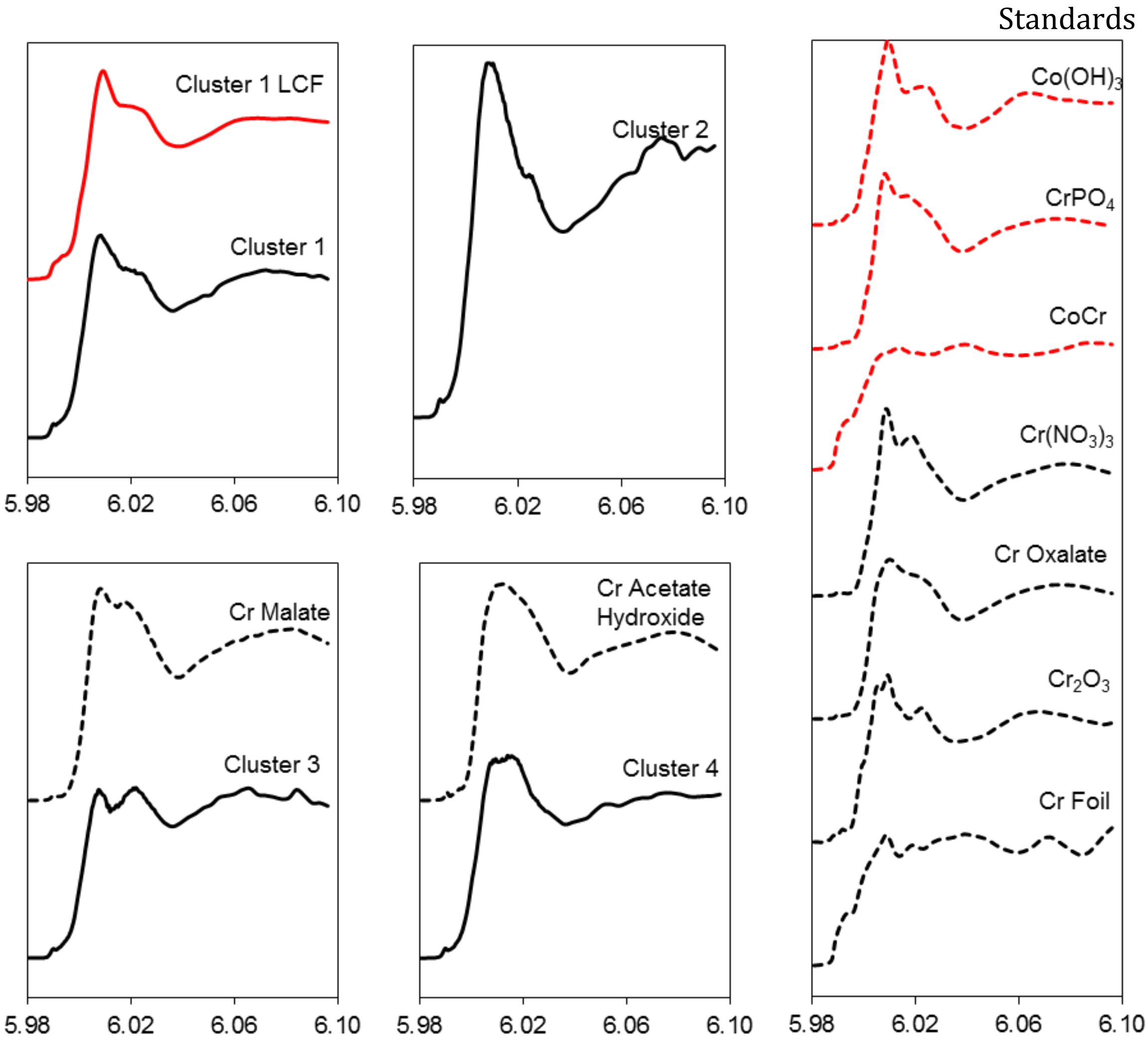

Figure 6.9: Clusters were produced of the XANES map in figure 6.8 using k-means clustering, after principle component analysis determined 4 components were sufficient to represent the majority of the data. Cluster 1 could be represented via linear combination fitting of the 3 standards in red, while clusters 3 and 4 have similar spectral features to Cr malate and acetate hydroxide. [right] Cr standards, acquired using similar beam set-ups are shown.

only variation in spectra being the contribution from metal-CoCr, apparent in the pre-edge.

These clusters (using sub-micron beam) were produced from interrogating sections from the same ‘tissue block’, and the criteria for selecting ROIs for XANES mapping (map across high intensity ‘particles’) were consistent between the micron and sub-micron measurements. Therefore, this suggests the reason for

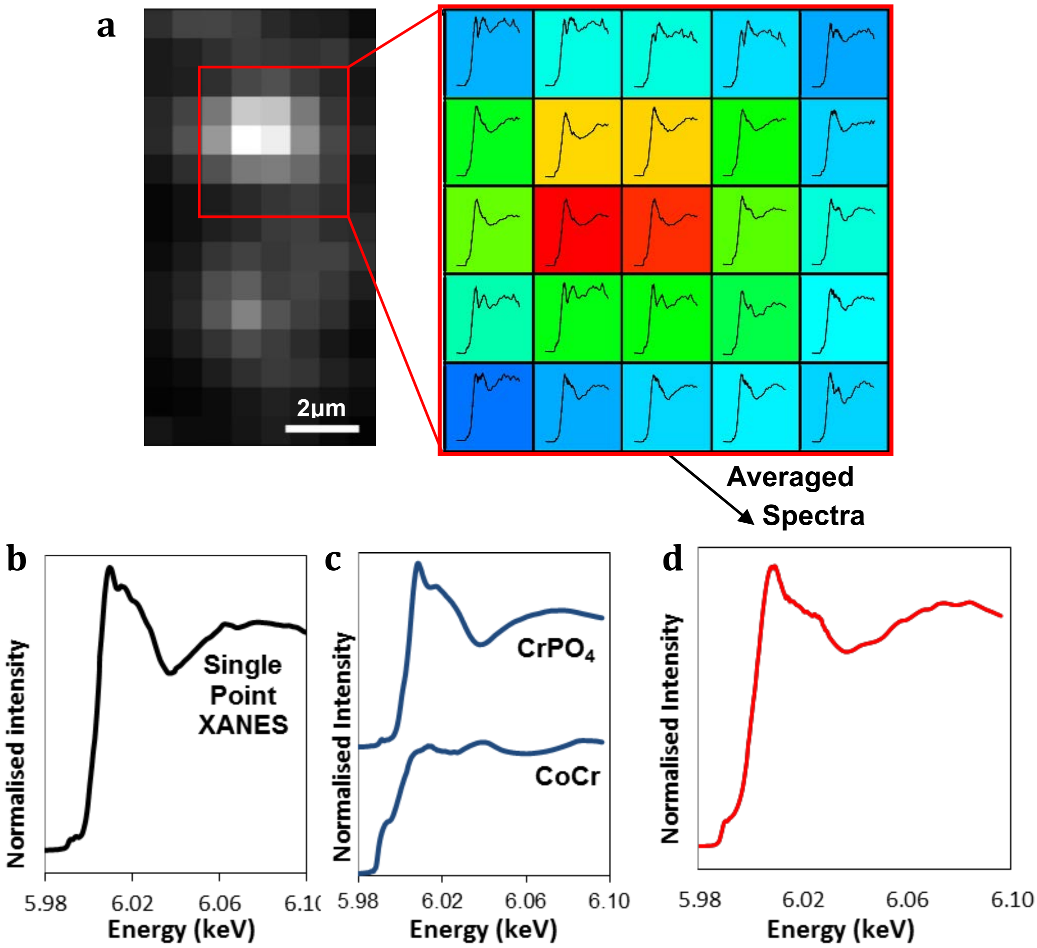

Figure 6.10: A 5x5pixel region, centred on the high Cr intensity point selected for spectral binning to mimic a 3µm beam. The spectra presented are [b] single point spectrum from Diamond, [c] reference spectra, and [d] averaged spectrum from 5x5 region.

such variation in the detected spectra is due to the target feature having spatial variability in speciation below the scale of the lateral measurement resolution (i.e. x-ray beam width). To confirm this, the higher resolution XANES map was 'binned' to imitate a 3µm resolution map.

6.3.2.3 Validation of Sub-Micron Mapping Approach

To mimic a single point XANES spectrum from a 3µm beam, spectra from a 5x5pixel region of the 600nm beam XANES map were averaged together (figure 6.10). The 5x5pixel region, centred on the high Cr intensity pixel, was consistent with the criteria for single point XANES measurements. Figure 6.10 shows a comparison between the single point XANES spectra acquired from a 3μm beam, concluded to correspond with literature reports of the main constituent measured being $CrPO_4$, and the averaged spectra from the XANES map.

Comparing the averaged spectrum and the single point spectra, it can be seen that they both contain the broadened pre-peak characteristic of metal-CoCr, and similar edge and post peak regions suggesting primarily CrPO4 content. However, it can be seen that the first interference peak (immediately after the edge) is of a lower intensity, compared to the edge peak, in the averaged 'binned' spectrum. The subtle intensity difference is likely due to dissimilar contributions from Cr(III) species at this location. Most importantly it is evident that averaging over an area of heterogeneous speciation is not an accurate representation of the species present. The most abundant species dominates the overall spectra and therefore lower concentration spectral features are lost.

To conclude, averaging a 5x5pixel region does produce a spectra which can be interpreted as containing predominately $CrPO_4$, which is in line with the single point XANES using a 3μm beam and the literature from Hart et al. (76, 77) using a 4μm beam. Bearing in mind the spectral variation that has been shown across this ROI, this indicates that micron-scale XANES analysis overlooks subtle changes in Cr speciation that is only seen using higher resolution approaches. Sub-micron XANES analysis has been performed on *ex vivo* tissue in this manner once before by Goode et al. (92) (in association with Hart), however they did not focus on the variation of Cr(III) species present. Instead, the paper concentrated on discussing the near absence of Co (implying localised rapid corrosion) and the presence of two distinct phases; a metallic core of CoCr surrounded by a majority of Cr(III). Variation in the species of Cr(III) using the sub-micron approach, compared to comparative micron-scale single point measurement approaches, were not discussed. It is believed this may have resulted in the potential for sub-micron XANES mapping being understated and a contributing factor as to why there were no additional follow-ups using this technique by this group or others.

6.3.3. Analysis Methods for Mapping Approach

6.3.3.1 Conformation of Metal Particle

Much of the XANES analysis performed centres around high Co-Cr intensity points. The rationale for this is the higher signal-to-noise and that these regions are likely to be metal particles. However, confirmation of this fact is preferable for the given tissue samples, as time restrictions for sub-micron XANES mapping restricted ROI selections max 10x10μm vs. the 300x45μm map with a micron beam. Therefore, at the SLS, which was capable of reaching very high energies, an experiment was performed to determine whether Mo co-located with high Co-Cr intensity points. Mo was chosen, as together with Co and Cr, they form the bulk composition of the MoM implant. It is expected that correlation of these 3 metals in tissue is highly indicative of a metal wear particle with at least a core composition reflective of the bulk metal. The XRF images in figure 6.11 have been normalised to the same scale for presentation. XRF intensity values can be used to inform relative amount when comparing images (i.e. higher intensity indicates more signal detected due to higher concentration). Consequently, assuming a

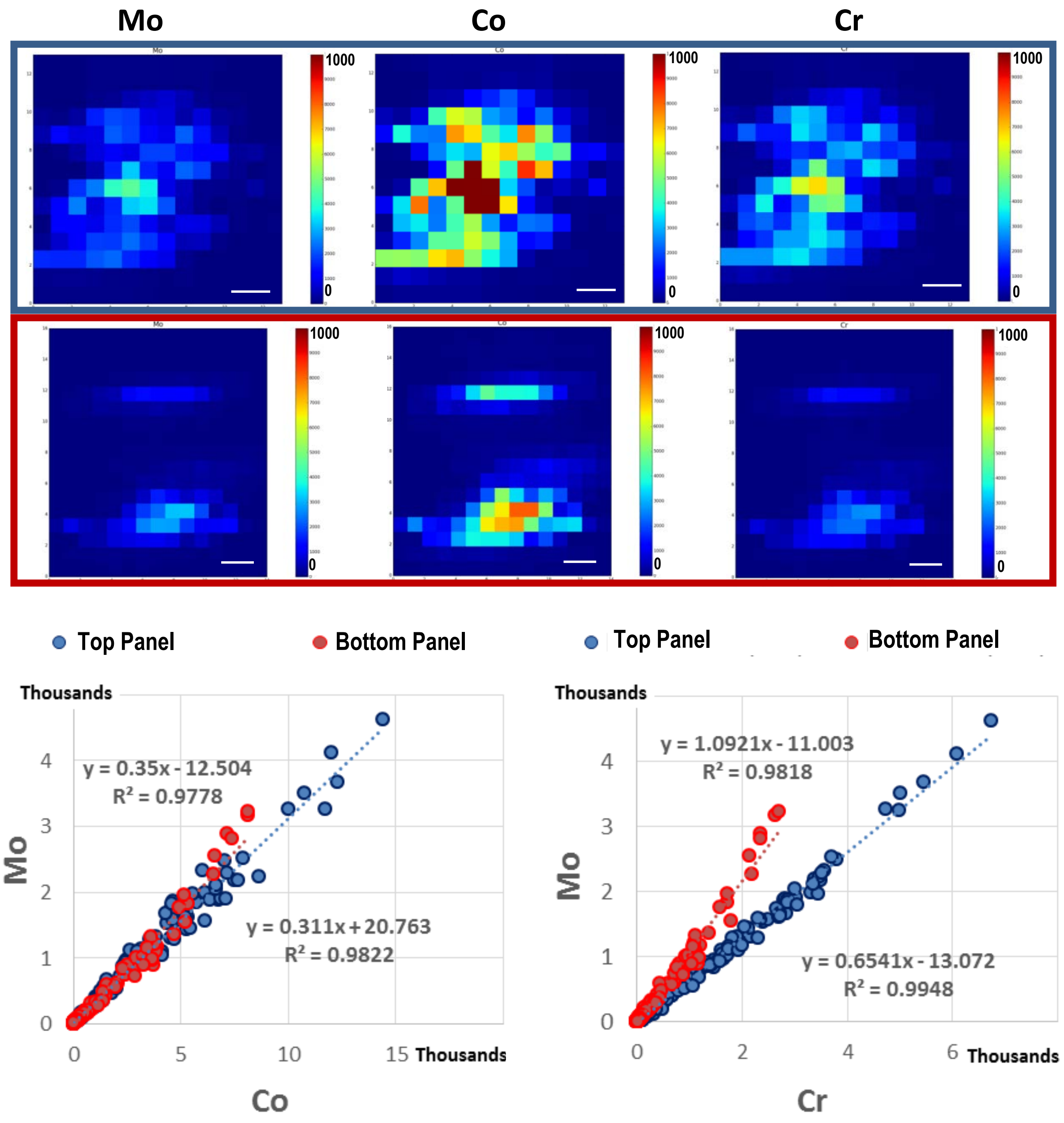

Figure 6.11: [Top] Two XRF intensity maps centred on a region of high Co. For each regions maps of Mo, Co and Cr were taken at the Swiss Light Source using a 20.02keV beam (Mo) and a 8.5keV beam (Co and Cr). [Bottom] Scatter plots showing the correlation between Mo & Co and Mo & Cr.

‘bulk’ metal particle is present, the intensities of these maps follow the expected trend of most to least intense being Co, Cr then Mo.

The graphs in figure 6.11 demonstrate positive correlation between Mo vs. Cr and Mo vs. Co for two high Co-Cr intensity regions, as the points align along a straight line. However a more rigorous test of the strength of correlation is to perform linear regression on the scatter plot and assess the R-squared value, which is a measure of the linear relationship between two variables and is between 0 and 1. A strong correlation is described as one that has an R-squared value close to 1 (188). Both of the selected regions appear to have a high correlation between Mo, and Co and Cr respectfully. Consequently, this strongly indicates confirmation that high Co-Cr intensity XRF points are characteristic of metal particles from MoM implants at the time of imaging.

6.3.3.2 Principal Component Analysis & Clustering

PCA analysis is ideal for large data sets. Reduction of dimensionality to a set of components which describe the majority of the system speeds up analysis and increases the signal-to-noise for spectra that may otherwise be classed as ‘background’. However due to the nature of the measurements performed (XANES), the application and interpretation of the generated PCs and clusters must be considered carefully. This is because not only does the beam size have a finite size, and thus the spectra acquired will almost always contain contributions of different species, but there will always be some very small relative movement between object and beam. As such the ideal situation of the number of PCs generated being equal to the number of species will most likely never occur as the spectra measured are not that of sole Cr species. Therefore it is most likely that a number of averaged clusters generated will contain linear combinations of reference spectra in differing ratios. This means that care must be taken when stating how many species one believes is present within a sample.

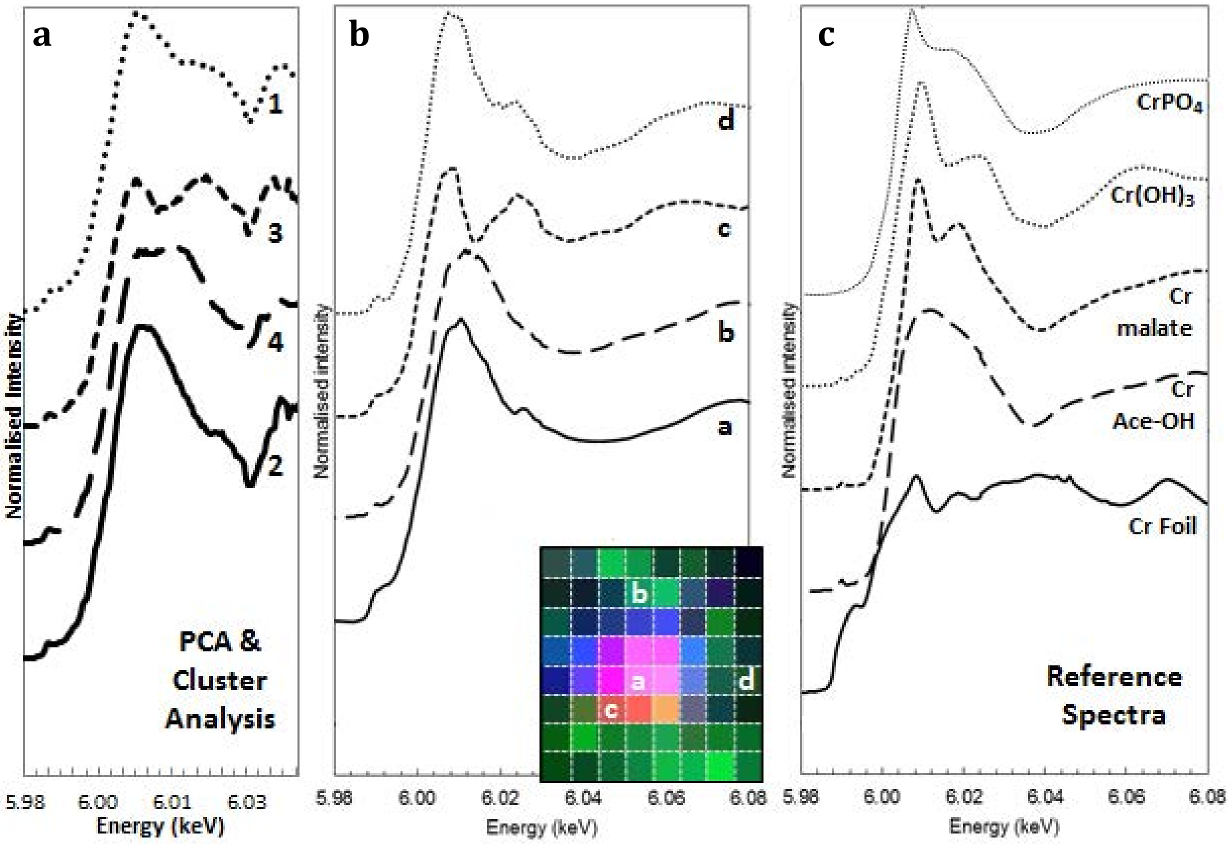

Figure 6.12: [a] Spectra from principal component and cluster analysis from figure 6.9 and [b] selected spectra from the inset Cr-XANES map from figure 6.8. These spectra originated from data acquired with the 600nm beam at ESRF. [c] Standards with similar spectral features to the corresponding spectrum acquired using a similar experimental set-up.

Figure 6.12 shows select spectra within the ROI that underwent PCA-clustering analysis, alongside the four generated clusters. Comparing the spectra generated from clustering to the selected spectra, it can be seen that the edge and post-edge regions are similar. This supports the use of PCA-cluster analysis, as long as the aforementioned concerns are considered; that the number of clusters generated through PCA-cluster analysis is on par with the number of unique spectra within the ROI analysed.

6.4. Conclusion

It has been demonstrated that, within tissues associated with CoCrMo metal-on-metal hip replacements, chemical variability at the nanometre scale is observed. The focus of this chapter was not to fully quantify the exact species of chromium within soft tissues originating from metallic prosthetics. Such an attempt would require biological repeats in addition to multiple patient samples. Rather, this work has shown that multiple species are present within the periphery of a single wear particle. This suggests further processing of implant debris within tissues at sites distant from the implant itself, where tribocorrosion processes are understood. Understanding the chemistry of particles within tissues is fundamental to understanding (i) how they arrived and how they are processed in the tissue, and (ii) how the particle composition, surface, size and the combination of these factors including variability of these dictate biomolecule association and cellular behaviours.

This chapter has demonstrated that a few point spectra with a broad (micron-sized) beam cannot represent the full chemical variability present within the tissue. It was shown that averaging a 5x5pixel region from a XANES map (using 600nm beam) produces a spectra which can be interpreted as mainly $CrPO_4$, which is reported in the literature as the predominant species for single point XANES using a micron-beam (76, 77). This proves that a submicron level of detail with a mapping approach is needed to fully understand the chemistry and determine species of interest that can impact cellular interaction and immune response to better inform biomaterial wear testing. This is complemented by the

Cr-precipitation studies in chapter 5, which show independently that chemical variability exists depending on the local environment, resulting in an additional classification of degradation products. Consequently, the use of only commercially purchased Co and Cr products for use in *in vitro* modelling overlooks the chemical complexity presented to the cellular/biological environment *in vivo*.

In addition, this chapter has presented a method of using PCA and cluster analysis to reduce the dimensionality of the large data sets resulting from XANES mapping. Given the edge and post-edge features in the clusters, generated from the XANES mapping data from ESRF, are similar to those observed around regions of high Co-Cr intensity, PCA and clustering of the data appears successful. However the method is limited by a preference of prior knowledge regarding the number of species likely to be present. If this is not known, care must be taken when stating how many species one believes is present within a sample.

Currently there are a very small number of groups worldwide using such advanced techniques applied to the problem of wear debris. However, the distinctiveness of the sub-micron XANES mapping approach presented in this chapter is that it enables the entire chemical variability of an image field to be captured; as opposed to simply identifying which element is present or measuring speciation at single user defined points. This does not change the impact or validity of previous studies; however it does highlight the problem associated with adhering to commonly used protocols, that there is a risk of simply repeating results with different samples. Further interrogation of *ex vivo* tissue, on a sub-micron scale, using the approach presented in this chapter will ultimately aid in producing more appropriate bio-modelling experiments and help in understanding why such a wide range of immunological reactions are observed across different patients. To fully understand the chemistry of wear particles within soft tissues multiple patients and tissue sites should be recorded utilising a sub-micron XANES mapping approach.

Chapter 7

Discussion

7.1. Overall Discussion

Implants and prostheses are an effective way of restoring function and managing pain. They have revolutionised the treatment of degenerative musculoskeletal conditions and increased the expectation for a good quality of life for patients. However, the concern of degradation products, such as ionic and particulate debris, is one that impacts all biomaterial research and understanding implant debris is fundamental to the development of new materials and devices.

There are many types of implant materials (28, 65, 178); however this thesis focused only on degradation products from metal-on-metal CoCr hip implants. The literature investigating CoCr implant derived debris is vast (11-18, 53, 59, 64, 67, 68) and has contributed to our understanding of the properties of the Co/Cr debris produced and the adverse cellular responses to such products. Yet, there is still a lack of comprehension regarding both the variability of implant derivatives generated and the effect such products can have on biological components other than just cells.

For example, studies typically focus on the effects degradation products have on 2D cell cultures, showing little to no consideration for the extracellular matrix (ECM) (112, 113, 121, 147, 157). As the ECM plays a crucial role in directing cell function, it is noteworthy that it is not considered when investigating the influence metal products have on the surrounding biological components. Given literature from the leather tanning industry (122, 123) regarding the effect of metal ions on collagen (the primary component of leather), it was hypothesised that metal ions may affect collagen assembly.

In addition, the biological consequences of implant derived debris will depend on how it is presented - either in metallic, ionic or precipitated form. Consequently, a thorough understanding the available degradation products is crucial to developing accurate *in vitro* modelling and understanding the potential cellular responses. Typically, literature reports the properties of particles produced through articulating wear (4, 58, 59) and ion levels in periphery bodily fluids (79, 86, 90). Only Tkaczyk et al. considered the effect of metal ion precipitation (93, 94), however this work was never expanded. Given the complexity of the biological surroundings it was reasonable to hypothesise that the local environment could influence the generation of precipitates.

Following on from this, the precipitation likely to form can be interrogated using non-destructive methods, such as x-ray fluorescence (XRF) and x-ray absorption near edge spectroscopy (XANES). However, to date there has been limited speciation identification of implant debris at sub-micron scales. Typically larger length scales are used (3-10μm), resulting in spectra which represent an average of all species within the cross-section of the x-ray beam. It was hypothesised that a broad (micron-sized) beam would not be able to represent potential chemical variability at the sub-micron scale.

The aforementioned hypothesises formed the basis of the three research questions addressed in this thesis. The first question, understanding how Co ions affect collagen assembly, aimed to determine the effect Co ions have on the structure of, and biological responses to, collagen gels as a model for type I collagen in the ECM. Chapter 4 showed that the presence of Co(II) has an adverse effect on collagen fibril assembly which impacts upon the subsequent collagen network. While the collagen triple-helix appeared to be maintained upon the addition of Co(II), a significant decrease in the D-banding of the fibrils was observed (>135ppm Co(II)). The addition, the presence of Co(II) resulted in fibril formation itself being retarded and the final bulk stiffness of the collagen matrix was reduced. In addition the fibrillar network was no longer homogeneous, and instead regions of varying density were observed, both in reflectance confocal and atomic force microscopy (RCM and AFM). This subsequently changed how cells interacted with the collagen, impacting functions such as cellular attachment and collagen gel contraction.

This work is the first of its kind to investigate how type I collagen can be modified by Co(II) ions, a metal degradation product of CoCr hip replacements, and how this effects subsequent cellular interactions with the modified matrix. However the results must be interpreted carefully. The ECM is a complex structure that, while consisting primarily of type I collagen, contains other fibrous proteins such as elastin and fibronectin, proteoglycans and water (189). As such, while it can be concluded that Co(II) has an adverse effect on type I collagen matrices, it cannot be stated that this causes the osteolysis and tissue necrosis observed during CoCr implant revisions (9, 10, 36). Nevertheless, the primary impact of this investigation is that ultimately, Co(II) ions have the potential to interfere with the organisation of ECM. This highlights the importance of studying possible matrix interactions with ionic debris in order to understand long-term biocompatibility, as current standards typically rely on 2D cellular cultures only.

The second question, investigating the precipitation of chromium ions, aimed to determine whether the composition and pH of the local environment impacted the precipitated products. Only Tkaczyk (85) had investigated the concept of precipitation, however they did not use address factors such as pH (which can vary around implant and tribocorrosion sites (177)), or non-simulated environments. The results showed that pH is a crucial barrier in initiating precipitation. Lower pH inhibits precipitation resulting in higher measurements of Cr ions within a supernatant, however biologically relevant pH (~7) results in rapid precipitation within an hour. Consequently this means that tribological studies investigating metal degradation, using centrifugation for separation analysis; need to be aware that there is not only two populations of degradation products (ions or wear particles). Instead, depending on the pH, a third population is also present. This third population can exist with a high degree of variability in properties such as size and composition depending on the local environment. For example, speciation studies using x-ray absorption near-edge spectroscopy (XANES) suggested that both organic and inorganic Cr-complexes are present; however the pivotal factor observed which determined the dominant species appeared to be the presence of Co(II). Overall, this work highlights an overlooked population of metal degradation products which directly impacts studies looking to evaluate the biological effect CoCr products have on cellular functions and the immune response. It is also the first to show that there is a level of nuance to the chemistry of Cr-precipitation which is highly dependent upon the local environment.

The third question, presenting a multiscale XANES mapping approach for metals within tissues, aimed to determine whether conventional single point, micron-beam techniques accurately portray the speciation of wear debris. The literature contains several studies investigating the distribution of cobalt and chromium speciation within tissues (75, 77, 92, 146). Current approaches predominantly use x-ray fluorescence (XRF) maps of tissues to inform locations for single point XANES observations to determine the speciation of the target element (i.e. Cr or Co). These single point XANES measurements effectively take an average over several microns due to the large beam width used for acquisition (typically 3-4μm). Given the observation of nano-scale CoCr wear particles (2, 4, 6, 58) and Cr precipitation (chapter 5) (93, 94), it was postulated that this method may omit small scale changes in speciation. As such, a mapping approach was developed acquire XRF maps to inform locations to perform XANES mapping using a higher resolution (600nm beam). It was not the objective of this thesis to use this mapping approach to determine the exact species present within the tissue at this scale, doing so would require greater patient numbers and biological repeats. The objective was instead to conclude whether such an approach would provide information as to the system that was otherwise omitted by previous methods. Chemical variability was observed across wear particles showing that Cr does not simply exist as Cr phosphate ($CrPO_4$), as interpreted by previous works (75, 77). While this thesis is not the first to use a sub-micron beam to acquire a

XANES map of a tissue section (92), it is the first to emphasise the importance of this method as an approach. Specifically, it demonstrates that the observed variation in species across a wear particle averages to produce a spectrum that reflects $CrPO_4$. This proves that a broad (micron-sized) beam, several orders of magnitude larger than the target, cannot represent the full chemical variability present within the tissue. Such an approach can be applicable to not just interrogating the chemical variability within tissue surrounding metal hip implants, but any implant of any material, as long as the target element is unique i.e. not naturally found in large concentrations within tissues.

The work presented in this thesis was performed to explore gaps in the knowledge relating to the implant derived debris from CoCr hip implants. It is understood that particulate wear debris is generated at the articulating surface of the hip joint (38, 57, 190). Typically these particles will end up in the surrounding tissues, becoming internalised by cells (147), initiating immune responses (13, 155) and cell death (153, 191). In addition, ionic debris is also generated at the bulk implant site. However corrosion processes are known to occur at various locations, such as the taper joint and implant crevices (177, 178, 192), as well as through dissolution of particulate wear (12, 88). What is becoming abundantly clear is the presence of another class of metal complexes within the tissues, either generated from ionic debris or following further processing within surrounding tissues (see chapter 6). The ions released at various locations surrounding the implant will encounter environments that vary in local composition and pH. If local pH <5 (which is common at corrosion sites (178)) precipitation processes will not initiate until pH >6(figure 5.2). The morphology and speciation of this precipitate will vary depending upon the composition and presence of other metal ions (figure 5.4 and figures 5.5-5.8 respectively); for example Cr(III) precipitation resulted in an evolution from an organic complex to a more inorganic complex with an increasing presence of Co(II). Variation in the speciation of the complex will impact upon the cellular response to such particles, as Tkaczyk et al. found when Cr(III)-complexes, formed in human serum, were more easily internalised than those formed in bovine serum (94).

The variability of speciation of Cr(III) precipitates was observed *in vivo* by performing XANES mapping with a high-resolution (sub-micron) beam. This approach enabled the entire chemical variability of the image field to be captured, showing the diversity of the Cr(III) species within the tissue. The smaller beam size allows for a greater level of discrimination between neighbouring points, and thus better determination of the changes in speciation. Previous methods used larger (micron sized) beams (75, 77), which reported primarily $CrPO_4$. When a region of the 600nm XANES map, equal to the micron sized beam, is averaged it approximates the micron sized beam (figure 6.10). This proves that micron sized beams cannot represent the full chemical variability within the tissue sample and a sub-micron XANES approach must be used. Consequently, the use of only commercially purchased Co and Cr products, such as bulk metal, $CrPO_4$ and metal oxides, for *in vitro* modelling overlooks the chemical complexity presented to the biological environment *in vivo*. In addition, the application of any Co/Cr product, whether commercially purchased or not, to a 2D cell culture is an over simplification. Not only is the ECM a complex system which produces biological responses that can vary patient to patient (149), but Co(II) ions can modify the 3D network of collagen changing the cellular response to the matrix (chapter 4).

Ultimately, all the work presented in this thesis contributes to the conclusion that current approaches to biological modelling *in vitro* of CoCr implant debris lacks the chemical complexity of the biological environment. This is not to suggest that previous biological studies (101, 104, 106, 149, 193) reported in the literature are not valid, as such studies are necessary in order to build an understanding of cellular responses and potential immune pathways leading to aseptic loosening. Rather, it needs to be acknowledged that observations of precipitate debris in tissues (with chemical variability showing both organic and inorganic species); suggests that commercially purchased, inorganic particles are insufficient to represent the chemistry of the particles presented to the cellular environment *in vivo.* In addition, the experimental results showing the adverse effects Co(II) ions can have on collagen suggests that the potential for ionic debris to interact with the non-cellular environment is disregarded.

The work in this thesis was designed to actively challenge and explore the gaps in knowledge that the literature portrays. While there is still work to be done to further explore the research presented in these chapters, the results discussed contributes to, and develops, the current knowledge surrounding the chemical variability of metal degradation products derived from CoCr hip implants and the impact ionic debris has on collagen (a main component of the ECM). In addition, this thesis has successfully presented a sub-micron XANES mapping approach capable of distinguishing the chemistry around the surface particles in tissues.

7.2. Future Works

It has been interpreted that Co(II) may affect the packing of the collagen molecules during assembly which may change the D-banding width and the availability of receptors for collagen-cell interactions. The next steps to further elucidate the mechanisms by which Co(II) is influencing fibril assembly is to determine exactly how Co(II) binds to the collagen molecule allowing for the structure to be modelled. This will provide further insight into how the mechanical properties are being altered. CD with increased sensitivity at lower wavelengths is essential to investigate the degree of triple-helical folding. In addition NMR (nuclear magnetic resonance) and x-ray crystallography should be considered, as it has been noted previously that NMR on collagen can provide residue-specific characterisation of the triple-helix (194). This may provide the insight to allow for determination of the protein structure and Co(II) binding locations, which may in turn indicate whether packing is likely to have been affected and thus influence the D-banding and availability of cellular attachment sites.

In addition, further exploration into cellular attachment or lack thereof, may provide a better understanding of how the collagen-cell interactions have been affected. More thorough quantification through attachment assays should be performed initially, followed by integrin-collagen studies. For example, fibronectin, a known glycoprotein for collagen-cell attachment, can be placed on an AFM tip and brought into contact with the collagen surface. If available binding sites have been reduced, due to the Co(II), the fibronectin will interact less with the surface producing less resistance, which is measured by the AFM tip (force measurements).

With respect to Cr(III) precipitation, future works include SEM and TEM (scanning and transmission electron microscopy) of precipitation produced in human synovial fluid, alongside XRD (x-ray diffraction) of precipitation formed in all media presented in chapter 5. SEM and TEM will provide size and morphology information while XRD will provide insight into the crystallography of the Cr-complexes. These experiments will allow for further fundamental characterisation of these Cr-complexes produced in human-derived biological media. However, what is important to include is variability in source of the human synovial fluid. Previous collaborations highlighted the ability for different immune responses to occur in response to CoCr added to whole blood *in vitro* (149). This implied patient specific reactions to wear debris. As such it would be interesting to consider the possibility that the organic Cr-complexes observed may vary across patients (i.e. which proteins and organic acids are present). In addition, the effect of this additional class of degradation products should also be evaluated on 2D cellular systems for comparison to existing metal particle and ion studies.

Finally, in relation to the mapping approach, extended energy maps need to be performed, i.e. XANES mapping (as seen in chapter 6) extended to include the EXAFS regions for improved speciation discrimination. In addition, performing biological repeats across a range of patient groups (i.e. age and sex) and determining whether the spatial variability in speciation changes significantly may aid in producing more appropriate bio-modelling experiments. This may ultimately help in understanding why such a wide range of immunological reactions are observed across different patients. Ultimately the goal would be to systematically quantify the variability in distribution and variability of chemical speciation of implant derived metals within peri-implant soft tissues taken at the time of revision surgeries and directly correlate this with the severity of the inflammatory response.

References

1. Learmonth I, Young C, Rorabeck C. The Operation of the Century: Total Hip Replacement. *The Lancet*. 2007; 370(9597):1508-19.

2. Billi F, Benya P, Ebramzadeh E, *et al.* Metal Wear Particles: What We Know, What We Do Not Know, and Why. *SAS J*. 2009; 3(4):133-42.

3. Catelas I, Medley J, Campbell P, *et al.* Comparison of in Vitro with in Vivo Characteristics of Wear Particles from Metal-on-Metal Hip Implants. *J Biomed Mater Res*. 2004; 70B(2).

4. Doorn P, Campbell P, Worrall J, *et al.* Metal Wear Particle Characterization from Metal on Metal Total Hip Replacements: Transmission Electron Microscopy Study of Periprosthetic Tissues and Isolated Particles. *J Biomed Mater Res*. 1998; 42:103-11.

5. Mischler S, Munoz A. Wear of Co Cr Mo Alloys Used in Metal-on-Metal Hip Joints: A Tribocorrosion Appraisal. *Wear*. 2013; 297(1-2):1081-94.

6. Shahgaldi B, Heatley F, Dewar A, *et al.* In Vivo Corrosion of Cobalt-Chromium and Titanium Wear Particles. *J Bone & Joint Surg(Br)*. 1995; 77B:962-6.

7. Campbell P, Yeom B, McKellop H, *et al.* Isolation of Predominantly Submicron Uhmwpe Wear Particles from Periprosthetic Tissues. *J Biomed Mater Res*. 1995; 29:127-31.

8. Sethi R, Neavyn M, Rubash H, *et al.* Macrophage Response to Cross-Linked and Conventional Uhmwpe. *Biomaterials*. 2003; 24(15):2561-73.

9. Harris W. Wear and Periprosthetic Osteolysis: The Problem. . *Clin Orthop Relat Res*. 2001; 393:66-70.

10. Purdue P, Koulouvaris P, Nestor B, *et al.* The Central Role of Wear Debris in Periprosthetic Osteolysis. *HSS J*. 2006; 2(2):102-13.

11. Papageorgiou I, Abberton T, Fuller M, *et al.* Biological Effects of Clinically Relevant Cocr Nanoparticles in the Dura Mater: An Organ Culture Study. *Nanomaterials*. 2014; 4:485-504.

12. Posada O, Gilmour D, Tate R, *et al.* Cocr Wear Particles Generated from Cocr Alloy Metal-on-Metal Hip Replacements, and Cobalt Ions Stimulate Apoptosis and Expression of General Toxicology-Related Genes in Monocyte-Like U937 Cells *Toxicol Appl Pharmacol*. 2014; 281(1):125-35.

13. Catelas I, Wimmer M, Utzschneider S. Polyethylene and Metal Wear Particles: Characteristics and Biological Effects. *Seminars in Immunopathology* 2011; 33(3):257-71.

14. Ingham E, Fisher J. Biological Reactions to Wear Debris in Total Joint Replacement. *Proc Inst Mech Eng H*. 2000; 214:21-37.

15. Neale S, Haynes D, Howie D*, et al.* The Effect of Particle Phagocytosis and Metallic Wear Particles on Osteoclast Formation and Bone Resorption in Vitro. *Journal of Arthroplasty*. 2000; 15(5):654-62.

16. Revell P. The Combined Role of Wear Particles, Macrophages and Lymphocytes in the Loosening of Total Joint Prostheses. *J R Soc Interface*. 2008; 5:1263-78.

17. Vermes C, Chandrasekaran R, Jacobs J*, et al.* The Effects of Particulate Wear Debris, Cytokines, and Growth Factors on the Functions of Mg-63 Osteoblasts. *J Bone Joint Surg Am*. 2001; 83A(2):201-11.

18. Vermes C, Roebuck K, Chandrasekaran R*, et al.* Particulate Wear Debris Activates Protein Tyrosine Kinases and Nuclear Factor Kb, Which Down-Regulates Type I Collagen Synthesis in Human Osteoblasts. *J Bone Miner Res*. 2000; 15(9):1759-65.

19. Haynes E, Metal Alloy. US patent 873745. 1907.

20. Haynes E, Metal Alloy. US patent 1057828. 1913.

21. Mishra AK, Hamby MA, Kaiser WB. Metallurgy, Microstructure, Chemistry and Mechanical Properties of a New Grade of Cobalt-Chromium Alloy before and after Porous-Coating. *Cobalt-Base Alloys for Biomedical Applications*. 1365: ASTM International; 1999. p. 71-88.

22. Hyslop D, Abdelkader A, Cox A*, et al.* Electrochemical Synthesis of a Biomedically Important Co–Cr Alloy. *Acta Mater*. 2010; 58(8):3124-30.

23. Al Jabbari Y. Physico-Mechanical Properties and Prosthodontic Applications of Co-Cr Dental Alloys: A Review of the Literature. *J Adv Prosthodont*. 2014; 6(2):138-45.

24. Tarzia V, Bottio T, Testolin L*, et al.* Extended (31 years) Durability of a Starr-Edwards Prosthesis in Mitral Position. *Interact Cardiovasc Thorac Surg*. 2007; 6(4):570-1.

25. Smith-Peterson M. Evolution of Mould Arthroplasty of the Hip Joint. *Bone Joint J*. 1948; 30-B(1):59-75.

26. Baker J, Vioreanu M, Khan H. Smith-Petersen Vitallium Mould Arthroplasty: A 62yr Follow-Up. *J Bone & Joint Surg(Br)*. 2001; 93-B(9):1285-6.

27. Knight S, Aujla R, Biswas S. Total Hip Arthroplasty - over 100 Years of Operative History. *Orthop Rev*. 2011; 3(2).

28. Gomez P, Morcuende J. Early Attempts at Hip Arthroplasty: 1700s to 1950s. *Iowa Orthop J*. 2005; 25:25-9.

29. McMaster W. Early Development of Total Hip Arthroplasty. In: Schwarzkopf R, (ed.). *Modern Techniques in Total Hip Arthroplasty: From Primary to Complex*. JP Medical Ltd; 2014.

30. Peltier L. A History of Hip Surgery. In: Callaghan J, Rosenberg A, Rubash H, (ed.). *The Adult Hip, Volume 1*. Oxford: LWW; 2007.

31. Brand R, Mont M, Manring M. Biographical Sketch: Themistocles Gluck (1853–1942). *Clin Orthop Relat Res*. 2011; 469(6).

32. McKee G. Total Hip Replacement - Past, Present and Future. *Biomaterials*. 1982; 3:130-5.

33. Charnley J. *Low Friction Arthroplasty of the Hip: Theory and Practice*. Berlin: *Springer*; 1979

34. Liao Y, Hoffman E, Wimmer M*, et al.* Cocrmo Metal-on-Metal Hip Replacements. *Phys Chem Chem Phys*. 2013; 15(3):1-26.

35. NJR. *National Joint Registry's 10th Annual Report*. 2013.

36. Evans E, Freeman M, Miller A*, et al.* Metal Sensitivity as a Cause of Bone Necrosis and Loosening of the Prosthesis in Total Joint Replacement. *J Bone Joint Surg*. 1974; 56(B)(4):626-42.

37. Cuckler J. The Rationale for Metal-on-Metal Total Hip Arthroplasty. *Clin Orthop Relat Res*. 2005; 441:132-6.

38. Clarke I, Good V, Williams P*, et al.* Ultra-Low Wear Rates for Rigid-on-Rigid Bearings in Total Hip Replacements. *Proc Inst Mech Eng H*. 2000; 214(4):331-47.

39. Sieber H, Rieker C, Kottig P. Analysis of 118 Second-Generation Metal-on-Metal Retrieved Hip Implants. *Journal Bone & Joint Surgery* 1999; 81(1):45-50.

40. Vendittoli P, Roy A, Mottard S*, et al.* Metal Ion Release from Bearing Wear and Corrosion with 28 Mm and Large-Diameter Metal-on-Metal Bearing Articulations. *Journal Bone & Joint Surgery (Br)*. 2010; 92-B(1):12-9.

41. Mahendra G, Pandit H, Kliskey K*, et al.* Necrotic and Inflammatory Changes in Metal-on-Metal Resurfacing Hip Arthroplasties. *Acta Orthop*. 2009; 80(6):653-9.

42. Kwon Y, Glyn-Jones S, Simpson D*, et al.* Analysis of 118 Second-Generation Metal-on-Metal Retrieved Hip Implants. *J Bone & Joint Surg(Br)*. 2010; 92-B:356-61.

43. Wooley P, Schwarz E. Aseptic Loosening. *Gene Ther*. 2004; 11:402-7.

44. Silverman E, Ashley B, Sheth N. Metal-on-Metal Total Hip Arthroplasty: Is There Still a Role in 2016? *Curr Rev Musculoskelet Med*. 2016; 9(1):93-6.

45. SCENIHR. *Opinion On: The Safety of Metal-on-Metal Joint Replacements with a Particular Focus on Hip Implants.* 25 September 2014.

46. Food and Drug Administration. *Effective Date of Requirement for Premarket Approval for Total Metal-on-Metal Semi-Constrained Hip Joint Systems.* Department of Health and Human Services, 2016 FDA-2011-N-0661.

47. Ohnsorge J, Holm R. Surface Investigations of Oxide Layers on Cobalt–Chromium Alloyed Orthopaedic Implants Using Esca Technique,. *Med Progr Technol*. 1978; 5:171-7.

48. ASTM. F75: Standard Specification for Cast Cobalt–Chromium–Molybdenum Alloy for Surgical Implant Applications. *Annual Book of Astm Standards: Medical Devices and Services*. 13.01. Philadelphia, PA,1998. p. 4-6.

49. Li YS, Wang K, He P*, et al.* Surface-Enhanced Raman Spectroelectrochemical Studies of Corrosion Films on Implant Co–Cr–Mo Alloy in Biosimulating Solutions. *Journal of Raman Spectroscopy*. 1999; 30(2):1097-4555.

50. McTighe T, Brazil D, Bruce W. Metallic Alloys in Total Hip Arthroplasty. In: Parvizi J, Goyal N, Cashman J, (ed.). *The Hip: Preservation, Replacement, and Revision*. Data Trace Publishing Company; 2015.

51. Muratoglu O, Kurtz S. Alternative Bearing Surfaces in Hip Replacement. In: Sinha R, (ed.). *Hip Replacement: Current Trends and Controversies*. CRC Press; 2002.

52. Yan Y, Neville A, Dowson D. Tribo-Corrosion Properties of Cobalt-Based Medical Implant Alloys in Simulated Biological Environments. *Wear*. 2007; 263:1105-11.

53. Bellefontaine G. The Corrosion of Cocrmo Alloys for Biomedical Applications: University of Birmingham; 2010.

54. Kaesche H. *Corrosion of Metals: Physicochemical Principles and Current Problems*: *Springer Science* 2003

55. Royhman D, Patel M, Runa M*, et al.* Fretting-Corrosion in Hip Implant Modular Junctions: New Experimental Set-up and Initial Outcome. *Tribology International*. 2015; 91:235-45.

56. Landolt D, Mishler S. *Tribocorrosion of Passive Metals and Coatings*. Lausanne: *Woodhead Publishing*; 2011

57. Halim T, Clarke I, Burgett-Moreno M*, et al.* A Simulator Study of Adverse Wear with Metal and Cement Debris Contamination in Metal-on-Metal Hip Bearings. *Bone and Joint Research*. 2015; 4:29-37.

58. Brown C, Williams S, Tipper J*, et al.* Characterisation of Wear Particles Produced by Metal on Metal and Ceramic on Metal Hip Prostheses under Standard and Microseparation Simulation. *J Mater Sci Mater Med*. 2007; 18:819-27.

59. Catelas I, Bobyn D, Medley J, *et al.* Size, Shape, and Composition of Wear Particles from Metal-Metal Hip Simulator Testing: Effects of Alloy and Number of Loading Cycles. *J Biomed Mater Re*. 2003; 67:312-27.

60. Mears D, Hanley E, Rutkoski R, *et al.* Ferrographic Analysis of Wear Particles in Arthroplastic Joints. *J Biomed Mater Res*. 1978; 12(6):867-75.

61. Langkamer V, Case C, Heap P, *et al.* Systemic Distribution of Wear Debris after Hip Repleacment. *J Bone & Joint Surg(Br)*. 1992; 74B(6):831-9.

62. Firkins P, Tipper J, Ingham E, *et al.*, editors. Quantitative Analysis of Wear Debris from Metal on Metal Hip Prostheses Tested in a Physiological Hip Joint Simulator. 45th Annual Meeting of the Orthopaedic Research Society; 1999 February; Anaheim, California.

63. Tipper J, Firkins P, Ingham E, *et al.* Quantitative Analysis of the Wear and Wear Debris from Low and High Carbon Content Cobalt Chrome Alloys Used in Metal on Metal Total Hip Replacements. *J Mater Sci Mater Med*. 1999; 10:353-62.

64. Pourzal R, Catelas I, Theissmann R, *et al.* Characterization of Wear Particles Generated from Cocrmo Alloy under Sliding Wear Conditions. *Wear*. 2011; 271(9-10):1658-66.

65. Campbell P, Dorey F, Amstutz A. Wear and Morphology of Ultra-High-Molecular-Weight-Polyethylene Wear Particles from Total Hip Replacements. *Proc Instn Mech Engrs*. 1996; 210H:167-74.

66. Wang A, Essner A, Stark C, *et al.* Comparison of Size and Morphology of Uhmwpe Wear Debris Produced by a Hip Joint Simulator under Serum and Water Lubricated Conditions. *Biomaterials*. 1996; 17(865-871).

67. Catelas I, Bobyn D, Medley J, *et al.* Effects of Digestion Protocols on the Isolation and Characterization of Metal-Metal Wear Particles. I. Analysis of Particle Size and Shape. *J Biomed Mater Res*. 2001; 55(3):320-9.

68. Catelas I, Bobyn J, Medley J, *et al.* Effects of Digestion Protocols on the Isolation and Characterization of Metal-Metal Wear Particles. Ii. Analysis of Ion Release and Particle Composition. *J Biomed Mater Res*. 2001; 55:330-7.

69. Schmiedberg S, Chang D, Frondoza C, *et al.* Isolation and Characterization of Metallic Wear Debris from a Dynamic Intervertebral Disc Prosthesis. *J Biomed Mater Res*. 1994; 28(11):1277-88.

70. Williams S, Isaac G, Hatto P, *et al.* Comparative Wear under Different Conditions of Surface-Engineered Metal-on-Metal Bearings for Total Hip Arthroplasty. *Journal of Arthroplasty*. 2004; 19(8):112-7.

71. Maloney W, Smith R, Schmalzried T, *et al.* Isolation and Characterization of Wear Particles Generated in Patients Who Have Had Failure of a Hip Arthroplasty without Cement. *J Bone & Joint Surg(Br)*. 1995; 77A:1301-10.

72. O'Connor J, Sexton B, Smart R. *Surface Analysis Methods in Materials Science*. 2 ed: *Springer Science & Business Media*; 2013

73. Tomaszewska E, Soliwoda K, Kadziola K, *et al.* Detection Limits of Dls and Uv-Vis Spectroscopy in Characterization of Polydisperse Nanoparticles Colloids. J Nanomater. 2013. Available from: doi:10.1155/2013/313081.

74. Shanbhag A, Jacobs J, Glant T, *et al.* Compositions and Morphology of Wear Debris in Failed Uncemented Total Hip Replacement. *Journal Bone & Joint Surgery (Br)*. 1994; 76-B:60-7.

75. Ektessabi A, Shikine S, Kitamura N, *et al.* Distribution and Chemical States of Iron and Chromium Released from Orthopedic Implants into Human Tissues. *X Ray Spectrom*. 2001; 30:44-8.

76. Hart A, Quinn P, Lali F, *et al.* Cobalt from Metal-on-Metal Hip Replacements May Be the Clinically Relevant Active Agent Responsible for Periprosthetic Tissue Reactions. *Acta Biomaterialia*. 2012; 8:3865-73.

77. Hart A, Quinn P, Sampson B, *et al.* The Chemical Form of Metallic Debris in Tissues Surrounding Metal-on-Metal Hips with Unexplained Failure. *Acta Biomaterialia*. 2010; 6(11):4439-46.

78. Sidaginamale R, Joyce T, Lord J, *et al.* Blood Metal Ion Testing Is an Effective Screening Tool to Identify Poorly Performing Metal-on-Metal Bearing Surfaces. *Bone Joint Res*. 2015; 2(5):84-95.

79. Dobbs H, Minski M. Metal Ion Release after Total Hip Replacement *Biomaterials*. 1980; 1:193-8.

80. Hartmann A, Hannemann F, Lutzner J, *et al.* Metal Ion Concentrations in Body Fluids after Implantation of Hip Replacements with Metal-on-Metal Bearing – Systematic Review of Clinical and Epidemiological Studies. *PLoS ONE*. 2013.

81. Hedberg Y, Wallinder I. Metal Release and Speciation of Released Chromium from a Biomedical Cocrmo Alloy into Simulated Physiologically Relevant Solutions. *J Biomed Mater Res Part B Appl Biomater*. 2014; 102:693-9.

82. Huber M, Reinisch G, Trettenhahn G, *et al.* Presence of Corrosion Products and Hypersensitivity-Associated Reactions in Periprosthetic Tissue after Aseptic Loosening of Total Hip Replacements with Metal Bearing Surfaces. *Acta Biomaterialia*. 2009; 5:172-80.

83. Jantzen C, Jorgensen H, Duus B*, et al.* Chromium and Cobalt Ion Concentrations in Blood and Serum Following Various Types of Metal-on-Metal Hip Arthroplasties - a Literature Overview. *Acta Orthop*. 2013; 84(3):229-36.

84. Langton D, Sidaginamale R, Joyce T*, et al.* The Clinical Implications of Elevated Blood Metal Ion Concentrations in Asymptomatic Patients with Mom Hip Resurfacings: A Cohort Study. *BMJ Open*. 2013; 3(3).

85. Tkaczyk C. Ions Released from Metal-on-Metal Hip Implants: In Vitro and in Vivo Investigations: McGill University; 2009.

86. Smith J, Lee D, Bali K*, et al.* Does Bearing Size Influence Metal Ion Levels in Large-Head Metal-on-Metal Total Hip Arthroplasty? A Comparison of Three Total Hip Systems. *J Orthop Surg Res*. 2014; 9(3).

87. Sampson B, Hart A. Clinical Usefulness of Blood Metal Measurements to Assess the Failure of Metal-on-Metal Hip Implants. *Ann Clin Biochem*. 2012; 49(2):118-31.

88. Shea K, Lundeen G, Bloebaum R*, et al.* Lymphoreticular Dissemination of Metal Particles after Primary Joint Replacements. *Clin Orthop Relat Res*. 1997; 338:219-26.

89. Campbell P, Urban R, Catelas I*, et al.* Autopsy Analysis Thirty Years after Metal-on-Metal Total Hip Replacement: A Case Report. *J Bone & Joint Surg*. 2003; 85A(11):2218-22.

90. Cobb A, Schmalzreid T. The Clinical Significance of Metal Ion Release from Cobalt–Chromium Metal-on-Metal Hip Joint Arthroplasty. *Proc Inst Mech Eng H*. 2006; 220(2):385-98.

91. Blumenthal N, Cosma V, Jaffe W*, et al.* A New Technique for Quantitation of Metal Particulates and Metal Reaction Products in Tissues near Implants *J Appl Biomater*. 1994; 5:191-3.

92. Goode A, Perkins J, Sandison A*, et al.* Chemical Speciation of Nanoparticles Surrounding Metal-on-Metal Hips. *Chem Commun*. 2012; 48(8335-8337).

93. Tkaczyk C, Huk O, Mwale F*, et al.* The Molecular Structure of Complexes Formed by Chromium or Cobalt Ions in Simulated Physiological Fluids. *Biomaterials*. 2009; 30:460-7.

94. Tkaczyk C, Huk O, Mwale F*, et al.* Investigation of the Binding of Cr(Iii) Complexes to Bovine and Human Serum Proteins: A Proteomic Approach. *J Biomed Mater Res A*. 2010; 94(1):214-22.

95. National Research Council. *Recommended Dietary Allowances: 10th Edition*: *National Academies Press*; 1989

96. Czarnek K, Terpiłowska S, Siwicki A. Selected Aspects of the Action of Cobalt Ions in the Human Body. *Central European Journal of Immunology*. 2015; 40(2).

97. ATSDR. *Public Health Statement - Cobalt*. 2004.

98. Steinhoff D, Mohr U. On the Question of a Carcinogenic Action of Cobalt-Containing Compounds. *Journal of Experimental Pathology*. 1991; 41(4):169-74.

99. Institute of Medicine Food and Nutrition Board. *Dietary Reference Intakes for Vitamin a, Vitamin K, Arsenic, Boron, Chromium, Copper, Iodine, Iron, Manganese, Molybdenum, Nickel, Silicon, Vanadium, and Zinc.* Washington DC: *National Academy Press*; 2001

100. IARC. *Chromium (Vi) Compounds*. World Health Organisation.

101. Hallab N, Jacobs J. Biologic Effects of Implant Debris. *Bull NYU Hosp Jt Dis*. 2009; 67:182-8.

102. Jacobs J, Roebuck K, Archibeck M*, et al.* Osteolysis: Basic Science. . *Clin Orthop Relat Res*. 2001; 393:71-7.

103. Ollivere B, Wimhurst J, Clark I*, et al.* Current Concepts in Osteolysis. *J Bone Joint Surg Br*. 2012; 94:10-5.

104. Bitar D, Parvizi J. Biological Response to Prosthetic Debris. *World J Orthop*. 2015; 6(2):172-89.

105. Hallab N, Jacobs J. Chemokines Associated with Pathologic Responses to Orthopedic Implant Debris. *Front Endocrinol*. 2017; 8(5).

106. Trindade M, Lind M, Sun D*, et al.* In Vitro Reaction to Orthopaedic Biomaterials by Macrophages and Lymphocytes Isolated from Patients Undergoing Revision Surgery. *Biomaterials*. 2001 22(3):252-9.

107. James G. A Clinicopathological Classification of Granulomatous Disorders. *Postgrad Med J*. 2000; 76:457-65.

108. Haynes D, Crotti T, Potter A*, et al.* The Osteoclastogenic Molecules Rankl and Rank Are Associated with Periprosthetic Osteolysis. *J Bone & Joint Surg(Br)*. 2000; 83B(6):902-11.

109. Masui T, Sakano S, Hasegawa Y*, et al.* Expression of Inflammatory Cytokines, Rankl and Opg Induced by Titanium, Cobalt-Chromium and Polyethylene Particles. *Biomaterials*. 2005; 26(14):1695-702.

110. Morais S, Carvalho G, Faria J*, et al.* In Vitro Biomineralization by Osteoblast-Like Cells Ii - Characterization of Cellular Culture Supernatants. *Biomaterials*. 1998; 19:23-9.

111. Morais S, Sousa J, Fernandes M*, et al.* In Vitro Biomineralization by Osteoblast-Like Cells I - Retardation of Tissue Mineralization by Metal Salts. *Biomaterials*. 1998; 19:13-21.

112. McKay G, Macnair R, MacDonald C, *et al.* Interactions of Orthopaedic Metals with an Immortalized Rat Osteoblast Cell Line. *Biomaterials*. 1996; 17:1339-44.

113. Anissian L, Stark A, Dahlstrand H, *et al.* Cobalt Ions Influence Proliferation and Function of Human Osteoblast-Like Cells. *Acta Orthopaedica Scandinavica*. 2009; 73(3):369-74.

114. Hallab N, Merritt K, Jacobs J. Metal Sensitivity in Patients with Orthopaedic Implants. *J Bone Joint Surg Am*. 2001; 83A:428-36.

115. Fratzl P. *Collagen: Structure and Mechanics*: *Springer Science & Business Media*; 2008

116. Shoulders M, Raines R. Collagen Structure and Stability. *Annual Review of Biochemistry*. 2009; 78:929-58.

117. Williams B, Gelman R, Poppke D, *et al.* Collagen Fibril Formation. *J Bio Chem*. 1978; 253(18):6578-85.

118. Viguet-Carrin S, Garnero P, Delmas P. The Role of Collagen in Bone Strength. *Osteoporosis International*. 2006; 17(3):319-36.

119. Bella J, Brodsky B, Berman H. Hydration Structure of a Collagen Peptide. *Structure*. 1995; 3(893-906).

120. Fullerton G, Amurao M. Evidence That Collagen and Tendon Have Monolayer Water Coverage in the Native State. *Cell Biology Int*. 2006; 30:56-65.

121. Allen M, Myer B, Millet P, *et al.* The Effects of Particulate Cobalt, Chromium and Cobalt-Chromium Alloy on Human Osteoblast-Like Cells in Vitro. *J Bone & Joint Surg*. 1997; 79B(3):475-82.

122. He L, Cai S, Wu B, *et al.* Trivalent Chromium and Aluminum Affect the Thermostability and Conformation of Collagen Very Differently. *J Inorg Biochem*. 2012; 117:124-30.

123. Wu B, Mu C, Zhang G, *et al.* Effects of Cr3+ on the Structure of Collagen Fiber. *Langmuir*. 2009; 25(19):11905-10.

124. Mabilleau G, Filmon R, Petrov P, *et al.* Cobalt, Chromium and Nickel Affect Hydroxyapatite Crystal Growth in Vitro. *Acta Biomaterialia*. 2009; 6:1555-60.

125. Jia M, Hong Y, Duan S, *et al.* The Influence of Transition Metal Ions on Collagen Mineralization. *Mater Sci Eng C*. 2013; 33(4):2399-406.

126. Bhatnagar R, Gough C. Circular Dichroism and the Conformational Analysis of Biomolecules. Springer; 1996.

127. Drzewiecki K, Grisham D, Parmar A*, et al.* Circular Dichroism Spectroscopy of Collagen Fibrillogenesis: A New Use for an Old Technique. *Biophys J*. 2016; 111(11):2377-86.

128. Tronci G, Russell S, Wood D. Photo-Active Collagen Systems with Controlled Triple Helix Architecture. *J Mater Chem*. 2013; 30B(1):3705-15.

129. Beck K, Chan V, Shenoy N*, et al.* Destabilization of Osteogenesis Imperfecta Collagen-Like Model Peptides Correlates with the Identity of the Residue Replacing Glycine. *Proc of National Academy of Sciences USA*. 2000; 97(8):4273-8.

130. Zhu J, Kauffman L. Collagen I Self-Assembly: Revealing the Developing Structures That Generate Turbidity. *Biophys J*. 2014; 106(8):1822-31.

131. Comper W, Veis A. The Mechanism of Nucleation for in Vitro Collagen Fibril Formation. . *Biopolymers*. 1977; 16:2113-31.

132. Sullivan M, Barker T, Funk S*, et al.* Matricellular Hevin Regulates Decorin Production and Collagen Assembly. *J Bio Chem*. 2006; 281:27621-32.

133. Li Y. The Mechanism of Collagen Self Assembly: Hydrophobic and Electrostatic Interactions: University of Florida; 2009.

134. Shen Z, Kahn H, Ballarini R*, et al.* Viscoelastic Properties of Isolated Collagen Fibrils. *Biophys J*. 2011; 100(12):3008-15.

135. Xu B, Li H, Zhang Y. Understanding the Viscoelastic Behavior of Collagen Matrices through Relaxation Time Distribution Spectrum. *Biomatter*. 2013; 3(3).

136. Zuidema J, Rivet C, Gilbert R*, et al.* A Protocol for Rheological Characterization of Hydrogels for Tissue Engineering Strategies. *J Biomed Mater Res B*. 2014; 102(5):1063-73.

137. Li H, Zhang Y. Modeling of the Viscoelastic Behavior of Collagen Gel from Dynamic Oscillatory Shear Measurements. *Biorheology*. 2014; 51(6):369-80.

138. Hartsuilker C, Welleman J. *Engineering Mechanics: Volume 2: Stresses, Strains, Displacements*: *Springer Science & Business Media*; 2007

139. Urban R, Jacobs J, Gilbert J*, et al.* Migration of Corrosion Products from Modular Hip Prostheses. *J Bone & Joint Surg*. 1994; 76a(9):1345-59.

140. Hart A, Quinn P, Sampson B*, et al.* The Chemical Form of Metallic Debris in Tissues Surrounding Metal-on-Metal Hips with Unexplained Failure. *Acta Biomaterialia*. 2010; 6(11):4439-46.

141. Iida A. Synchrotron Radiation X-Ray Fluorescence Spectrometry. *Encyclopedia of Analytical Chemistry*. 2013. p. 1-23.

142. Li Y, Chen C. Chapter 6: X-Ray Absorption Spectroscopy. In: Chen C, Chai Z, Gao Y, (ed.). *Nuclear Analytical Techniques for Metallomics and Metalloproteomics*. Royal Society of Chemistry; 2010. p. 163-211.

143. Gao Y. Chapter 3: X-Ray Fluorescence. In: Chen C, Chai Z, Gao Y, (ed.). *Nuclear Analytical Techniques for Metallomics and Metalloproteomics*. Royal Society of Chemistry; 2010. p. 2-94.

144. Calvin S. *Xafs for Everyone*: *CRC Press*; 2013

145. Yano J, Yachandra V. X-Ray Absorption Spectroscopy. *Photosynth Res*. 2009; 102(2-3):241-54.

146. Vespa M, Wieland E, Dähn R*, et al.* Determination of Elemental Distribution and Chemical Speciation in Highly Heterogeneous Cementitious Materials Using Synchrotron-Based Micro-Spectroscopic Techniques. *Cement and Concrete Research*. 2007; 37:1473-82.

147. Shah K, Quinn P, Gartland A*, et al.* Understanding the Tissue Effects of Tribo-Corrosion: Uptake, Distribution, and Speciation of Cobalt and Chromium in Human Bone Cells. . *J Orthop Res*. 2015; 33:114-21.

148. Ordonez Y, Montes-Bayon M, Blanco-Gonzalez E*, et al.* Metal Release in Patients with Total Hip Arthroplasty by Df-Icp-Ms and Their Association to Serum Proteins. *J Anal At Spectrom*. 2009; (24):1037-43.

149. Pearson M, Williams R, Floyd H*, et al.* The Effects of Cobalt–Chromium–Molybdenum Wear Debris in Vitro on Serum Cytokine Profiles and T Cell Repertoire. *Biomaterials*. 2015; 67:232-9.

150. Hart A, Matthies A, Henckel J*, et al.* Understanding Why Metal-on-Metal Hip Arthroplasties Fail: A Comparison between Patients with Well-Functioning and Revised Birmingham Hip Resurfacing Arthroplasties. *J Bone Joint Surg Am*. 2010; 94(4).

151. Sinnett-Jones P, Wharton J, Wood R. Micro-Abrasion-Corrosion of a Cocrmo Alloy in Simulated Artificial Hip Joint Environments. *Wear*. 2005; 259(7-12):898-909.

152. Ortega R, Bresson C, Fraysse A*, et al.* Cobalt Distribution in Keratinocyte Cells Indicates Nuclear and Perinuclear Accumulation and Interaction with Magnesium and Zinc Homeostasis. *Toxicology Letters*. 2009; 188(1):26-32.

153. Catelas I, Petit A, Vali H*, et al.* Quantitative Analysis of Macrophage Apoptosis Vs. Necrosis Induced by Cobalt and Chromium Ions in Vitro. *Biomaterials*. 2005; 26(15):2441-53.

154. Posada O, Tate R, Grant M. Toxicity of Cobalt-Chromium Nanoparticles Released from a Resurfacing Hip Implant and Cobalt Ions on Primary Human Lymphocytes in Vitro. . *J Appl Toxicology*. 2015; 35(6).

155. Posada O, Tate R, Meek R*, et al.* In Vitro Analyses of the Toxicity, Immunological, and Gene Expression Effects of Cobalt-Chromium Alloy Wear Debris and Co Ions Derived from Metal-on-Metal Hip Implants. . *Lubricants*. 2015; 3(3):539-68.

156. Shah K, Wilkinson J, Gartland A. Cobalt and Chromium Exposure Affects Osteoblast Function and Impairs the Mineralization of Prosthesis Surfaces in Vitro. *J Orthop Res*. 2015; 33(11):1663-70.

157. Charras G, Sahai E. Physical Influences of the Extracellular Environment on Cell Migration. *Nature Rev Molec Cell Bio*. 2014; 15(12):813-24.

158. Shannon R. Revised Effective Ionic Radii *Acta Cyrst*. 1976; A32:751-67.

159. Wells A. *Structural Inorganic Chemistry 5th Ed.* Oxford: *Clarendon Press*; 1984

160. Vernon R, Gooden M. An Improved Method for the Collagen Gel Contraction Assay. *In Vitro Cell Dev Biol Anim*. 2002; 38(2):97-101.

161. Krause M, Oliver J. Natural Widths of Atomic K and L Levels, Ka X-Ray Lines and Several Kll Auger Lines. *J Phys Chem Ref Data*. 1979; 8(329).

162. Wold S, Esbensen K, Geladi P. Principal Component Analysis. . *Chemometrics and Intelligent Laboratory Systems*. 1987; 2:37-52.

163. Socrates G. *Infrared and Raman Characteristic Group Frequencies Tables and Charts Third Edition*. UK: *Wiley* 2001

164. Jokinen J, Dadu E, Nykvist P*, et al.* Integrin-Mediated Cell Adhesion to Type I Collagen Fibrils. *J Bio Chem*. 2004; 279(30):31956-63.

165. Barczyk M, Gullberg D, Carracido S. Integrins. *Cell Tissue Res*. 2010; 339(1):269-80.

166. Meyer M, Wiesmann H. Cell/Surface Interactions. *Bone and Cartilage Engineering*. Springer Science & Business Media; 2006.

167. Puelo D, Bizios R. Extracellular Matrix Derived Ligands. *Biological Interactions on Material Surfaces*. Springer Science & Business Media; 2009.

168. Davidenko N, Schuster C, Bax D*, et al.* Evaluation of Cell Binding to Collagen and Gelatin - a Study of the Effect of 2d and 3d Architecture and Surface Chemistry. *J Mater Sci Mater Med*. 2016; 27(10).

169. Dittmore A, Silver J, Sarkar S*, et al.* Internal Strain Drives Spontaneous Periodic Buckling in Collagn & Regulates Remodelling. *PNAS*. 2016; 113(30):8436-41.

170. Moteiro G, Fernandes A, Sundararaghaven H*, et al.* Positively & Negatively Modulating Cell Adhesion to Type I Collagen Via Peptide Grafting. *Tissue Eng Part A*. 2011; 17(13-14):1663-73.

171. Wertz D, Kruh R. X-Ray Diffraction Study of Some Concentrated Cobalt (Ii) Chloride Solutions. *J Chem Phys*. 1969; 50:4313-7.

172. Birdi-Chouhan G, Shelton R, Bowen J, *et al.* Soluble Silicon Patterns and Templates: Calcium Phosphate Nanocrystal Deposition in Collagen Type 1. *RSC Advances*. 2016; 6:99809-15.

173. Larkin P. Infrared and Raman Spectroscopy: Principles and Spectral Interpretation. Elsevier; 2011.

174. Frushour B, Koenig J. Raman Scattering of Collagen, Gelatin, and Elastin. *Biopolymers*. 1975; 14:379-91.

175. Haynes D, Potter A, Atkins G, *et al.*, editors. Metal Particles Stimulate Expression of Regulators of Osteoclast Development Including Osteoclast Differentiation Factor (Rankl/Trance), Osteoprotogenin and Macrophage Colony Stimulating Factor. . 45th Annual Meeting of the Orthopaedic Research Society; 1999.

176. Scharf B, Clement C, Zolla V, *et al.* Molecular Analysis of Chromium and Cobalt-Related Toxicity. *Scientific Reports*. 2014; 4.

177. Levine D, Staehle R. Crevice Corrsion in Orthopedic Implant Metals. *J Biomed Mater Res*. 1977; 11(4):553-61.

178. Willert H, Broback L, Buchhorn G, *et al.* Crevice Corrosion of Cemented Titanium Alloy Stems in Total Hip Replacements. *Clin Orthop Relat Res*. 1996; 333:51-75.

179. Kokubo T, Kushitani H, Sakka S, *et al.* Solutions Able to Reproduce in Vivo Surface-Structure Changes in Bioactive Glass-Ceramic a-W. *J Biomed Mater Res*. 1990; 24:721-34.

180. Schindelin J, Arganda-Carreras I, Frise E. Fiji: An Open-Source Platform for Biological-Image Analysis. *Nature Methods*. 2012; 9(7):676-82.

181. Frommer J. The Chromium X-Ray Absorption near Edge Structure: New Ways to Determine the Local Molecular Environment of Trivalent Chromium in Geochemical. Zurich2009.

182. Salvati E, Betts F, Doty S. Particulate Metallic Debris in Cemented Total Hip Arthroplasty. *Clin Orthop Relat Res*. 1993; 293:160-73.

183. Willert H, Semlitsch M. Reactions of the Articular Capsule to Wear Products of Artificial Joint Prostheses. *J Biomed Mater Res A*. 1977; 11(2):157-64.

184. Xia X, Monteiro-Riviere N, Mathur S, *et al.* Mapping the Surface Adsorption Forces of Nanomaterials in Biological Systems. *ACS Nano*. 2011; 5(11):9074-81.

185. Sabokbar A, Pandley R, Athanasou N. The Effect of Particle Size and Electrical Charge on Macrophage-Osteoclast Differentiation and Bone Resorption. *J Mater Sci Mater Med*. 2003; 14(3):731-8.

186. Yang H, Lul C, Yang D*, et al.* Comparative Study of Cytotoxicity, Oxidative Stress and Genotoxicity Induced by Four Typical Nanomaterials: The Role of Particle Size, Shape and Composition. *J Appl Toxicology*. 2005; 29(1):69-78.

187. Lerotic M, Mak R, Wiric S*, et al.* Mantis: A Program for the Analysis of X-Ray Spectromicroscopy Data. *J Synchrotron Rad*. 2014; 21(5):1206-12.

188. Gether G, Hall S. *Straightforward Statistics: Understanding the Tools of Research*: *Oxford University Press*; 2014

189. Frantz C, Stewart K, Weaver V. The Extracellular Matrix at a Glance. *J Cell Sci*. 2010; 123(24):4195-200.

190. Bhatt H, Goswami T. Implant Wear Mechanisms - Basic Approach. *Biomedical Materials*. 2008; 3(4).

191. Granchi D, Cenni E, Ciapetti G*, et al.* Cell Death Induced by Metal Ions: Necrosis or Apoptosis? *J Mater Sci Mater Med*. 1998; 9:31-7.

192. Cooper H, Urban R, Wixson R*, et al.* Adverse Local Tissue Reaction Arising from Corrosion at the Femoral Neck-Body Junction in a Dual-Taper Stem with a Cobalt-Chromium Modular Neck. *J Bone & Joint Surg*. 2013; 95 - A(10):865-72.

193. Ingham E, Green T, Stone M*, et al.* Production of Tnf-Alpha and Bone Resorbing Activity by Macrophages in Response to Different Types of Bone Cement Particles. *Biomaterials* 2000; 21:1005-13.

194. Li Y. Application and Development of Nmr Spectroscopy to Study the Conformation and Dynamics of Collagen-Like Triple Helical Peptides: University of Medicine and Dentistry of New Jersey; 2007.